

THE UNIVERSITY OF CALGARY

**MULTICONVERTED REFLECTIONS IN MARINE ENVIRONMENTS
WITH THIN PERMAFROST LAYERS**

by

Taiwen Chen

A THESIS

SUBMITTED TO THE FACULTY OF GRADUATE STUDIES
IN PARTIAL FULFILLMENT OF THE REQUIREMENTS FOR THE
DEGREE OF MASTER OF SCIENCE

DEPARTMENT OF GEOLOGY AND GEOPHYSICS

CALGARY, ALBERTA

APRIL, 1994

© Taiwen Chen 1994

THE UNIVERSITY OF CALGARY

FACULTY OF GRADUATE STUDIES

The undersigned certify that they have read, and recommend to the Faculty of Graduate Studies for acceptance, a thesis entitled "Multiconverted Reflections in Marine Environments with Thin Permafrost Layers" submitted by Taiwen Chen in partial fulfillment of the requirements for the degree of Master of Science.



Supervisor, Dr. D.C. Lawton,
Department of Geology and Geophysics



Dr. R.J. Brown,
Department of Geology and Geophysics



Dr. K. Duckworth,
Department of Geology and Geophysics



Dr. H. Laue,
Department of Physics and Astronomy

April 18, 1994

ABSTRACT

In the Canadian Beaufort Sea, high-quality conventional P-wave reflection seismic data are difficult to obtain because of a severe screening effect of a shallow layer of ice-bearing permafrost. Multiconverted reflections (PSPPSP) were studied in this thesis project in order to evaluate images of reflections underlying a high-velocity layer. Acoustic seismic physical modeling and numerical modeling experiments were undertaken for multiconverted reflection (PSPPSP) recognition and analysis. Both the physical and numerical modeling results indicate that values of the S-wave velocity in the high-velocity layer and of the P-wave velocity in deeper layers are the most important quantities affecting the multiconverted PSPPSP reflection amplitude. Based on these investigations, two lines of field data (datasets A and B) from the Canadian Beaufort Sea were processed. From this field data study, it was concluded that analysis of the multiconverted reflections is very critical for the data interpretation in this environment, especially for the shallow section.

Acknowledgments

Completion of this thesis would not have been possible without various contributions of many people. I'd first like to express my special thanks to Dr. Don Lawton, my thesis supervisor, for his many positive contributions to this research. He has provided me with excellent supervision throughout my M.Sc. program, and encouraged me in many ways to complete this research. His excellent example of a geophysical scientist is very much appreciated. Most synthetic data in chapters 2 and 3 were created by using Don's software based upon the solutions to Zoeppritz equations.

I owe a great deal of gratitude to many people in CREWES. Especially, Mr. Mark Lane has provided me with processing support using Landmark/ITA software on Sun workstations. Mr. Darren Foltinek and Mr. Henry Bland are also thanked for their computer assistance. Mr. Eric Gallant has provided me with technical assistance for physical modeling set-up. Dr. James Brown is thanked for his fine example in mastering the balance between science and bridge.

The seismic data was donated by Gulf Canada Resource Ltd. (dataset A in chapter 5) and Halliburton Geophysical (dataset B in chapter 5). Zoeppritz plot in Figure 2.8 was created by using the code of Dr. P.P.C. Wu (The University of Calgary) based on the solutions to the Zoeppritz equations. The financial support was provided by the CREWES Project as a research assistantship, the Department of Geology and Geophysics as a teaching assistantship, China National Petroleum Cooperation (CNPC) as a research scholarship.

Finally, I'd like to thank my wife Yan Liu for her patience and understanding during the completion of this thesis, especially for her standing behind me through all long hours spent at the university.

TABLE OF CONTENTS

APPROVAL PAGE.....	ii
ABSTRACT.....	iii
ACKNOWLEDGMENTS.....	iv
TABLE OF CONTENTS.....	v
LIST OF TABLES.....	viii
LIST OF FIGURES.....	ix
LIST OF SYMBOLS.....	xii
Chapter 1: Introduction	1
1.1 Introduction	1
1.2 Imaging methods over high-velocity surface layer	2
1.3 Concept of multiconverted reflections	2
1.4 Thesis objectives and structure	4
1.5 Review of AVO analysis.....	5
1.5.1 AVO theory.....	5
1.5.2 Conventional P-wave AVO case studies.....	8
1.5.3 AVO inversion	9
1.5.4 Converted-wave AVO and inversion	9
1.5.5 Poisson's ratio	10
1.6 Hardware and software used	11
Chapter 2: Physical seismic modeling	13
2.1 Introduction	13
2.2 Model construction.....	15
2.3 Data acquisition.....	18
2.4 Numerical modeling.....	19
2.5 Results	20

2.5.1 Group 1.....	20
2.5.2 Group 2.....	28
2.6 Conclusions	34
Chapter 3: Numerical seismic modeling	35
3.1 Introduction	35
3.2 Dependence on the S-wave velocity in layer 2	35
3.3 Dependence on the P-wave velocity in layer 2	38
3.4 Dependence on the P-wave velocity in layer 4	41
3.5 Dependence on the thickness of layer 2	43
3.6 Dependence on the depth of layer 2	45
3.7 Discussion	46
Chapter 4: Multifold physical modeling data.....	48
4.1 Introduction	48
4.2 Data acquisition.....	50
4.3 Data processing	50
4.3.1 Preprocessing.....	55
4.3.2 Mute, deconvolution and bandpass	55
4.3.3 CMP sorting, velocity analysis, NMO correction and mute	57
4.3.4 Stack.....	63
4.3.5 Migration.....	64
4.4 Discussion	68
Chapter 5: Multiconverted reflection analysis for the Canadian Beaufort Sea data	71
5.1 Introduction	71
5.2 Dataset A.....	71
5.2.1 Introduction.....	71
5.2.2 Preprocessing	75

5.2.3	CMP sorting, velocity analysis, NMO correction and mute	75
5.2.4	Stack and AGC.....	77
5.2.5	Discussion	77
5.3	Postcritical seismic data processing for the dataset A.....	77
5.3.1	Introduction	77
5.3.2	'Block-shift' NMO correction method.....	79
5.3.3	Results	82
5.3.4	Discussion	84
5.4	Dataset B	86
5.4.1	Introduction	86
5.4.2	Preprocessing	86
5.4.3	Gain	90
5.4.4	$f-k$ filtering and mute.....	90
5.4.5	CMP sorting and deconvolution.....	92
5.4.6	Velocity analysis and NMO correction.....	92
5.4.7	Mute and $f-k$ filtering.....	92
5.4.8	Trim statics.....	94
5.4.9	Stack and bandpass.....	96
5.4.10	Post-stack $f-k$ filtering.....	96
5.4.11	Discussion	96
5.5	Conclusions	99
Chapter 6	Conclusions	100
6.1	Thesis summary.....	100
6.2	Future work	101
REFERENCES	103

LIST OF TABLES

1.1.	Physical parameters for Figure 1.3.....	7
2.1.	Scaling factors used for physical modeling.....	14
2.2.	Physical properties and parameters of layer 2.....	17
2.3.	Physical properties and parameters of layer 4.....	17
2.4.	R_0 for all layer 2.....	17
2.5.	Geometry used for the seismic physical modeling experiments.....	19
3.1.	Physical parameters for layer 2, Model 3-1.....	36
3.2.	Physical parameters for layer 2, Model 3-2.....	39
3.3.	Physical parameters for layer 4, Model 3-3.....	41
4.1.	Materials and their physical parameters, Model 4-1.....	48
4.2.	Geometry for data acquisition over Model 4-1.....	50
4.3.	Seismic processing flow for the physical modeling data.....	55
4.4.	RMS velocities for CMP 101.....	63
5.1.	Acquisition geometry for the dataset A.....	75
5.2.	Acquisition geometry for the dataset B.....	89
5.3.	RMS velocities obtained from the velocity analysis.....	94

LIST OF FIGURES

1.1.	Schematic diagram showing nonconverted and multiconverted reflections in marine environments.....	3
1.2.	Schematic diagram showing reflection and transmission of a plane wave incident at the interface between two horizontal layers.....	6
1.3.	Zoeppritz amplitude plots.....	7
2.1.	Schematic diagram of the physical model.....	15
2.2.	A shot gather and its synthetic seismogram for model 1-1.....	21
2.3.	A shot gather and its synthetic seismogram for model 1-2.....	23
2.4.	A shot gather and its synthetic seismogram for model 1-3.....	24
2.5.	A shot gather and its synthetic seismogram for model 1-4.....	26
2.6.	A shot gather and its synthetic seismogram for model 1-5.....	27
2.7.	A shot gather and its synthetic seismogram for model 2-1.....	29
2.8.	Reflection amplitude versus incident angle plots.....	30
2.9.	A shot gather and its synthetic seismogram for model 2-2.....	32
2.10.	A shot gather and its synthetic seismogram for model 2-3.....	33
3.1.	Amplitude versus offset for model 3-1.....	37
3.2.	Amplitude versus offset for model 3-2.....	40
3.3.	Amplitude versus offset for model 3-3.....	42
3.4.	Schematic diagram of model 3-4.....	43
3.5.	Reflection amplitude versus source-to-receiver offset.....	44
3.6.	Schematic diagram of model 3-5.....	45
3.7.	Amplitude versus offset for model 3-5.....	47
4.1.	Schematic diagram of the model with lateral velocity change.....	49
4.2.	Shot gather on location A.....	51

4.3.	Shot gather on location <i>B</i>	52
4.4.	Shot gather on location <i>C</i>	53
4.5.	Shot gather on location <i>D</i>	54
4.6.	NMO-corrected gather for CMP 101.....	58
4.7.	NMO-corrected gather for CMP 194.....	59
4.8.	NMO-corrected gather for CMP 287.....	60
4.9.	NMO-corrected gather for CMP 380.....	61
4.10.	NMO-corrected gather for CMP 504.....	62
4.11.	Final stacked section for the physical modeling data.....	65
4.12.	The near offset (0 to 800 m) stacked section for the physical modeling data.....	66
4.13.	The far offset (800 to 1984 m) stacked section for the physical modeling data....	67
4.14.	Final migrated section for the physical modeling data.....	69
5.1.	A shot-gather example of dataset A, Canadian Beaufort Sea.....	73
5.2.	Schematic diagram showing the model.....	74
5.3.	The conventional seismic data processing flow chart for dataset A.....	74
5.4.	NMO-corrected CMP gather.....	76
5.5.	Stacked section using conventional processing procedures, dataset A.....	78
5.6.	Calculation procedure for ‘block shift’ NMO correction.....	81
5.7.	‘Block shift’ NMO-corrected gathers.....	83
5.8.	Processing flow with ‘block shift’ normal-moveout application, dataset A.....	84
5.9.	Stacked section using ‘block shift’ NMO correction, dataset A.....	85
5.10.	Seismic data processing flow for the dataset B.....	87
5.11.	A shot gather for the dataset B.....	88
5.12.	The same shot gather as shown in Figure 5.11 but with prestack <i>f-k</i> filtering and mute applied.....	91
5.13.	NMO-corrected CMP gather for the dataset B.....	93

5.14. Same CMP gather as shown in Figure 5.13 but with prestack $f-k$ filtering applied.....	95
5.15. Final stacked section for the dataset B.....	97
5.16. Final stacked section for the dataset B with a poststack $f-k$ filter applied.....	98

LIST OF SYMBOLS

P	P-mode wave
S	S-mode wave
V_p	P-wave velocity
V_s	S-wave velocity
V_{rms}	root-mean-square velocity
ρ	Density
σ	Poisson's ratio
R_0	Reflection coefficient at normal incidence
t_0	Two-way vertical travel time
AVO	Amplitude versus offset
NMO	Normal moveout
CMP	Common midpoint

Chapter 1: Introduction

1.1 Introduction

In some sedimentary basins of the world, a high-velocity layer (e.g., carbonate, salt, volcanics, anhydrite or permafrost) occurs at or near the surface. Seismic data quality is usually degraded by this high-velocity layer due to many factors, such as energy scattering and reverberation in the high-velocity layer, seismic wave reverberation in a low-velocity layer which may overlie the high-velocity layer, and weak energy transmission through the high-velocity layer.

During Pleistocene glacial cycles, sea level in the Canadian Beaufort Sea was up to 100 m below present sea level (Poley et al., 1989). Delta plain deposits were thus exposed to Arctic climatic conditions. As a result, sediments on the Canadian Beaufort Sea shelf became ice-bonded to a depth varying from 10 m to 600 m (Poley et al., 1989). The P-wave velocity in the ice-bearing permafrost can be twice as much as that in the surrounding sediments. Seismic data recorded in areas affected by ice-bearing permafrost are generally of poor quality. Poor penetration (between the high-velocity ice-bearing permafrost and the low-velocity surrounding sediments) and reverberation (between the top and the bottom of the ice-bearing permafrost layers) are two factors causing poor data quality (Poley et al., 1989).

In some areas of the Canadian Beaufort Sea, several ice-bearing permafrost layers overlie one another (Poley and Lawton, 1991). Due to the high impedance contrast at the top of the shallowest layer of ice-bearing permafrost, it is not easy to image the bottom of this layer, nor to image the top and bottom of the second (and deeper) layers of ice-bearing permafrost. It is desirable to obtain improved reflections from the permafrost sequence because the distribution of permafrost has a strong influence on gravel mining and drilling in this area (Poley, 1987; Poley et al., 1989).

1.2 Imaging methods over high-velocity surface layer

Young and Lucas (1988) suggested that integrated geophysical techniques can be used to determine the basement horizon and the major structural trends in some areas with a high-velocity surface layer. These integrated techniques mainly include gravity, magnetotelluric, aeromagnetic, and seismic methods. Fuller et al. (1988) showed that it is possible to reject linear reverberations by the application of a velocity filter. However, processing cannot solve the fundamental problem of the field data quality by itself. Meaningful data must be recorded if a meaningful result is to be obtained (Sheriff, 1991).

Since 1983, much attention has been paid to seismic data acquisition in areas with a high-velocity near-surface layer. The suggested solutions to the problem can be summarized as: the seismic array approach (Embree and Roche, 1983; Meister et al., 1989; Pritchett, 1991); receiver patches (Pritchett, 1991); wide-aperture seismic (Jarchow et al., 1991); stack array (Anstey, 1986a; Anstey, 1986b; Pritchett, 1991), and converted-wave and shear-wave programs (Purnell, 1992; Pritchett, 1991). These last workers suggested that better energy transmission with the S-waves in the high-velocity layer and P-waves elsewhere could be observed. Fix et al. (1983) showed some successful examples of using S-waves to get interpretable reflection data in areas with a high-velocity near-surface layer.

1.3 Concept of multiconverted reflections

This thesis discusses the acquisition, processing and interpretation of seismic data in a marine environment with a high-velocity permafrost layer within the top 60 m to 300 m below the sea floor. A simplified model of this environment is shown in Figure 1.1, in which layers 1 and 3 are water layers representing low-velocity unconsolidated sediments, and layers 2 and 4 are composed of high-velocity material representing permafrost layers. Rays 1, 2 and 3 are single-mode reflections, i.e., no mode conversion occurs at any part along the raypaths. Ray 1 (PP) is the P-P reflection from the top of

layer 2 (the first ice-bearing permafrost layer); ray 2 (PPPP) is the P-P reflection from the top of layer 3; and ray 3 (PPPPPP) is the P-P reflection from the top of layer 4 (the second ice-bearing permafrost layer). Due to the fact that the P-wave velocities of the ice-bonded layers (layers 2 and 4) are about twice as much as those of layers 1 and 3, the absolute acoustic impedance difference between layer 1 and layer 2 is large. Therefore, a large amount of incident energy is reflected back at the top of the first ice-bearing permafrost layer (layer 2). This is one reason why reflections from the bottom of the first ice-bearing permafrost layer (top of layer 3), as well as from deeper reflectors, are not as strong as those from the top of layer 2.

At large offsets, efficient conversion to and transmission of S-wave energy through layer 2 occurs at the top of layer 2. This results in converted-mode energy in layer 2. The converted energy is reflected from the bottom of the first ice-bearing permafrost layer. This reflected S-mode energy is converted back to P-mode wave at the

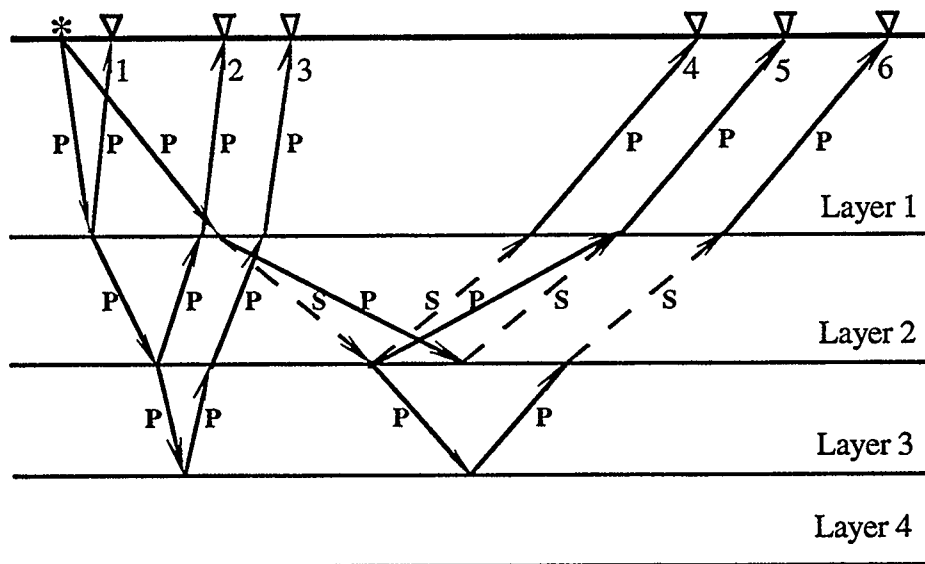


FIG. 1.1. Schematic diagram showing nonconverted and multiconverted reflections in marine environments. Layers 1 and 3 are water layers; layers 2 and 4 are high-velocity layers, such as the ice-bearing permafrost in Canadian Beaufort Sea. * = source; ∇ = receiver; P = P-wave mode; S = S-wave mode.

interface between layer 1 and layer 2, resulting in a PSSP multiconverted reflection (ray 4 in Figure 1.1).

Ray 6 is another multiconverted reflection in this environment. The S-wave in layer 2 can be converted back to a P-wave upon transmission into layer 3. The P-mode energy is reflected from the top of the underlying substrate (layer 4). Double conversion can also occur for the upgoing wave, resulting in the PSPPSP arrival (ray 6) in Figure 1.1.

Other two kinds of multiconverted reflections (PSPP and PPSP, ray 5) are also shown in Figure 1.1 but are not discussed in details in this thesis.

1.4 Thesis objectives and structure

Purnell et al. (1990) demonstrated the potential of salt imaging in the Gulf Coast area offshore Louisiana by using the multiconverted PSSP wave. They found the S-wave velocity in salt to be a fairly close match to the P-wave velocity of the surrounding sediments and good energy coupling between the S-wave in salt and P-wave elsewhere was observed. Based on this work (Purnell et al., 1990), it was proposed that better penetration may be observed between S-waves in the ice-bearing permafrost and P-waves elsewhere in the Canadian Beaufort Sea. The P-wave velocity of the ice-bearing permafrost layer is about as twice as much as that in the surrounding sediments. Therefore, good energy coupling between the S-wave in permafrost and the P-wave elsewhere could be expected (Chen and Lawton, 1992a and 1992b).

This thesis reports on multiconverted reflection modeling and processing of field data from the Canadian Beaufort Sea. The first purpose of this study has been to evaluate images of reflections underlying a high-velocity layer using multiconverted reflections (PSSP and PSPPSP). The second goal has been to undertake AVO (amplitude-versus-offset) analysis for multiconverted reflections (PSPPSP) in marine environments with the ice-bearing permafrost layers. In order to fulfill this study objective, seismic modeling (both physical and numerical) and processing of seismic field data were undertaken.

Physical and numerical modeling results are described in chapters 2 and 3, respectively. The numerical modeling results were used to evaluate and confirm the results from physical modeling in terms of event traveltimes and amplitudes. An advantage of the numerical modeling is that the physical parameters can be changed easily. Chapter 4 discusses the processing procedure and results for multifold physical modeling data. Chapter 5 includes mostly data processing of the field data, with a focus on both the shallow reflections (dataset A: high-resolution site survey data) and the deep reflections (dataset B: conventional exploration data). Conclusions and recommendations from this study are summarized in chapter 6.

1.5 Review of AVO analysis

1.5.1 AVO theory

Consider the general case of a seismic plane wave which impinges non-normally upon a flat interface separating two half-spaces (Figure 1.2). In Figure 1.2, P_I, P_R, S_R, P_T, S_T refer to incident P-wave, reflected P-wave, reflected S-wave, transmitted P-wave and transmitted S-wave, respectively. θ_1 and θ_2 are angles of incidence of the reflected and transmitted P-waves. ϕ_1 and ϕ_2 refer to angles of the reflected and transmitted S-waves. V_{pi}, V_{si}, ρ_i are P-wave velocity, S-wave velocity and density of layer i ($i = 1, 2$), respectively. V_{pi}, V_{si} are related by Snell's law:

$$\frac{V_{pi}}{\sin\theta_i} = \frac{V_{si}}{\sin\phi_i}, \quad (1.1)$$

Snell's law for Figure 1.2 can be expressed as:

$$\frac{V_{p1}}{\sin\theta_1} = \frac{V_{s1}}{\sin\phi_1} = \frac{V_{p2}}{\sin\theta_2} = \frac{V_{s2}}{\sin\phi_2}, \quad (1.2)$$

since the incident and the reflected P-wave velocities are the same, and therefore, the angles of the incidence and the reflection P-waves are the same (θ_1 in Figure 1.2).

Assuming conservation of energy, modified by Snell's law and the boundary conditions, the standard Zoeppritz equations can be obtained (Aki and Richards, 1980). Figure 1.3 shows an example of Zoeppritz plots of a reflected P-wave, reflected S-wave, transmitted P-wave and transmitted S-wave for a model with two half-spaces. Table 1.1 lists the physical parameters for the model.

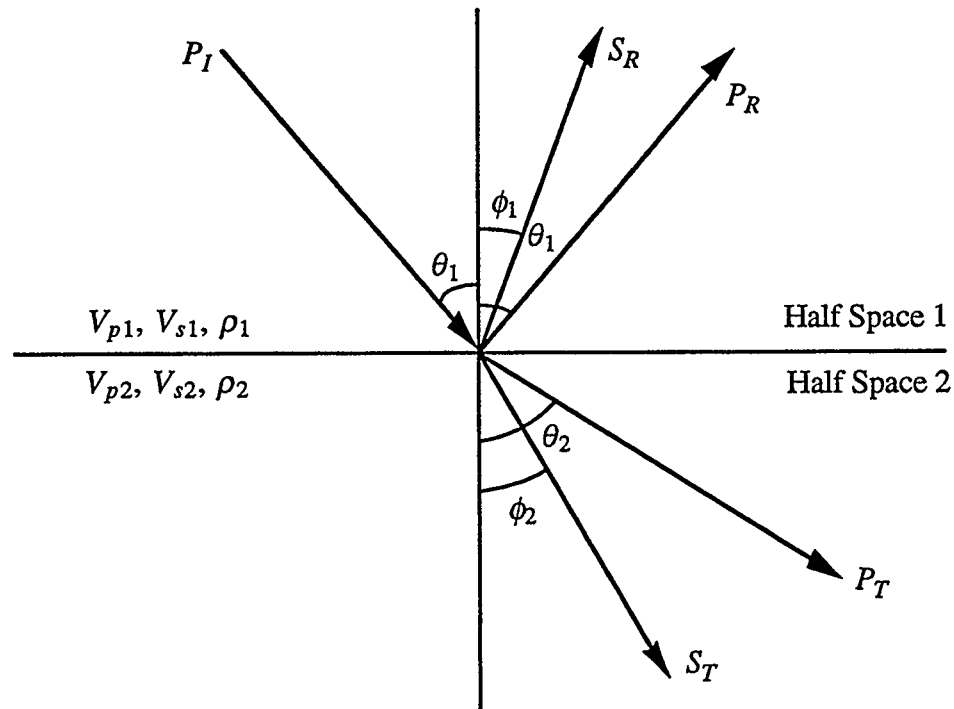


FIG 1.2. Schematic diagram showing reflection and transmission of a plane wave incident at the interface between two horizontal layers. P_I , P_R , S_R , P_T , S_T = incident P-wave, reflected P-wave, reflected S-wave, transmitted P-wave and transmitted S-wave, respectively; θ_1 , θ_2 = Angles of the incident (reflected) and transmitted P-waves; ϕ_1 , ϕ_2 = Angles of the reflected and transmitted S-waves; V_{pi} , V_{si} , ρ_i = P-wave velocity, S-wave velocity and density of layer i ($i = 1, 2$).

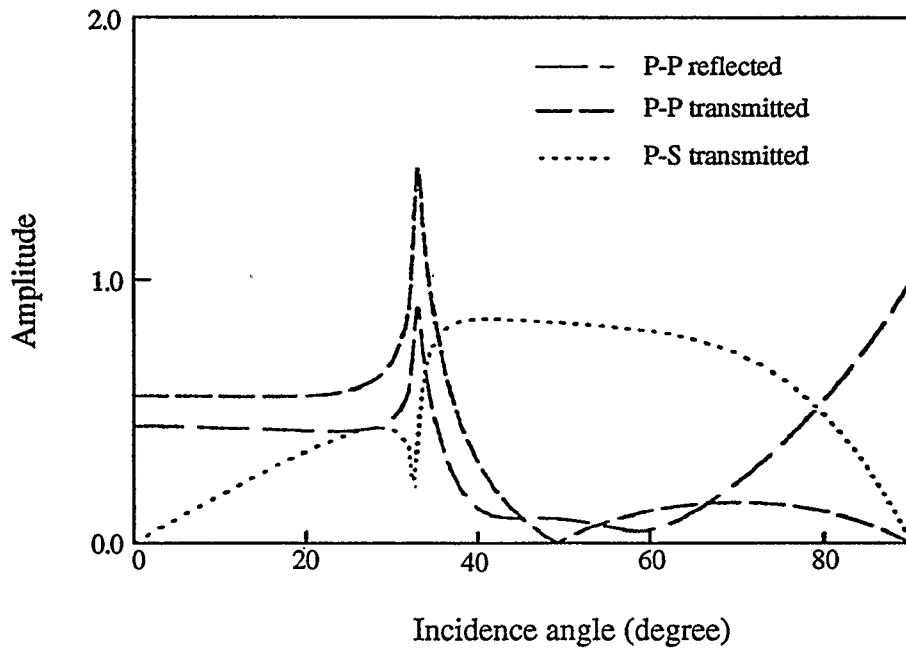


FIG 1.3. Zoeppritz amplitude plots for reflected P-wave, transmitted P-wave and transmitted S-wave. Amplitude refers to the absolute value of the displacement reflection coefficient. Incidence angle refers to the angle of P-wave incidence upon the interface between two half-spaces.

Table 1.1 Physical parameters for Figure 1.3

	V_p (m/s)	V_s (m/s)	ρ (kg/m ³)
Half-space 1	1486	0	1000
Half-space 2	2740	1385	1200

In Figure 1.3, incidence angle refers to the angle of P-wave incidence upon the interface between two half-spaces and amplitude refers to the absolute value of the displacement reflection coefficient. The physical parameters of half-spaces 1 and 2 are the same as those of water and Plexiglas, respectively. That is, Figure 1.3 shows the Zoeppritz plots for a model with water overlying Plexiglas. This kind of model will be discussed further in chapters 2 and 3.

In Figure 1.3, the critical angle for P-waves is 31.5° . There is not much amplitude variation with change of incidence angle for either the reflected or the transmitted P-waves before the critical angle. However, the amplitude of the transmitted S-wave increases with increasing incidence angle. This is because there are no transmitted S-waves at normal incidence. Beyond the critical angle, most incident P-wave energy is converted to transmitted S-wave. The transmitted S-wave energy was recorded as multiconverted reflections (PSSP and PSPPSP) in physical and numerical modeling experiments (chapters 2 and 3).

1.5.2 Conventional P-wave AVO case studies

As early as 1955, Koefoed (1955) calculated a reflection coefficient as a function of incidence angle, and noted the importance of Poisson's ratio (or, equivalently, V_p/V_s) on AVO anomalies. Koefoed concluded that a positive reflection coefficient at normal incidence and a positive Poisson's ratio change causes reflection amplitude to increase with increasing offset. Conversely, a positive reflection coefficient at normal incidence and a negative Poisson's ratio change cause reflection amplitude to decrease with increasing offset.

Ostrander (1984) used a three-layer gas-sand model to illustrate AVO effects. The gas sands that produce the amplitude anomalies have lower impedance than the encasing shales and have reflections that increase in magnitude with offset. Ostrander concluded that the change in Poisson's ratio has a strong influence on changes in reflection coefficient as a function of angle of incidence, and suggested that the analysis of seismic reflection amplitude versus shot-to-group offset can in many cases distinguish between gas-related amplitude anomalies and other types of amplitude anomalies. Rutherford and Williams (1989) further discussed three classes of gas-sand reflectors in terms of reflection coefficients at normal incidence at the top of the gas sand: class 1 gas sands have higher impedance than the encasing sediments, class 2 have the same

impedance as the encasing sediments and class 3 have lower impedance than the encasing sediments. The Poisson's ratio change is negative for all three cases. For the first case, the reflection amplitude decreases with increasing offset and for the other two cases it increases with increasing offset. The third case is the same one as discussed by Ostrander (1984).

1.5.3 AVO inversion

Recent work suggests that P-P AVO analysis and inversion might be an effective way to extract rock properties (Smith and Gidlow, 1987; Castagna and Smith, 1993). Smith and Gidlow (1987) proposed a method for P-P AVO inversion. The Zoeppritz equations can be simplified to describe the variation of the P-wave reflection coefficient with the P-wave angle of incidence as a function of the P-wave velocities, the S-wave velocities and the densities. For each CMP gather, the P- and S-wave reflectivity weights can be obtained by comparing the simplified Zoeppritz equations and the real data using a least squares method. Then P- and S-wave weighted stacks can be obtained from the P- and S-wave reflectivity gathers. It is then possible to create a display which highlights the Poisson's ratio anomaly (or the presence of gas) by using the so called 'fluid factor stack' sections. Castagna and Smith (1993) showed that the difference between the P- and S-wave weighted stacks is robust enough to determine the presence of a Poisson's ratio anomaly (or gas-saturated zone).

1.5.4 Converted-wave AVO and inversion

It seems that most AVO analyses in the last decade were undertaken for single-mode reflections. Few authors have paid much attention to converted-wave AVO analysis. However, in recent years, some authors in the CREWES Project at The University of Calgary have been using converted-waves for AVO analysis. Abdalla (1989) carried out P-SV synthetic modeling for the Carrot Creek area of central Alberta.

Nazar and Lawton (1993) did further P-SV AVO analysis for the Carrot Creek field. They found that only subtle amplitude variation exhibits itself on the P-P component whereas, at the location of conglomerate bodies, strong amplitude anomalies can be observed on the P-SV component (Nazar, 1991; Nazar and Lawton, 1993). This is due to a phase change for the P-P data. They also showed the usefulness of amplitude variations in partially stacked sections to the final stacked sections for both the P-P and P-SV cases. Coulombe et al. (1992a and 1992b) undertook AVO analysis using borehole seismic data. They pointed out certain advantages of using VSP data for AVO analysis, i.e., the wavelet is known and the incident and reflected amplitudes can be measured immediately above the interface, which results in the true-amplitude seismic response (Coulombe, 1993; Coulombe et al., 1992a and 1992b). Le et al. (1992) suggested that converted-waves might resolve thin beds better than single-mode waves through full-wave AVO synthetic study.

Stewart (1990) proposed a method to jointly process P-P and P-SV data to extract compressional and shear properties. He suggested that better estimated velocities might be obtained by using two independent observations: P-P reflectivity (R^{PP}) and P-SV reflectivity (R^{PS}). Zhang and Stewart (1991) did some tests on the joint inversion by using synthetic seismic data, and they concluded that a great improvement of the S-wave velocity estimation can be obtained for synthetic data by using the joint inversion method.

1.5.5 Poisson's ratio

From the above, it seems that a change in Poisson's ratio (or the change in the ratio between the P- and S-wave velocities) between the layers of interests is one of the critical factors for AVO analysis. By definition, Poisson's ratio is the ratio of the fractional transverse contraction to the fractional longitudinal extension when a rod is

stretched (Sheriff, 1991). Theoretically, Poisson's ratio can be obtained by the following equation:

$$\sigma = \frac{\left(\frac{V_p}{V_s}\right)^2 - 2}{2\left[\left(\frac{V_p}{V_s}\right)^2 - 1\right]}, \quad (1.3)$$

where V_p , V_s , σ are P-wave velocity, S-wave velocity, and Poisson's ratio of a rock.

Poisson's ratio can be obtained directly if both P- and S-wave velocities are known. Previous work has shown that both P- and S-wave velocities can be directly obtained by using multicomponent seismic data (Tatham and McCormack, 1991). However, the S-wave velocity is unknown for most cases, so that it is necessary to predict the Poisson's ratio for a target zone when its S-wave velocity is unknown. It is well known that Poisson's ratio is affected by many factors, such as lithology, porosity, pore shape, pore fluid, clay content, and anisotropy etc. (Toksöz et al., 1976; Ostrander, 1984; Brown et al., 1989; Miller and Stewart, 1990; Tatham and McCormack, 1991). Gassmann theory is a technique through which Poisson's ratio versus porosity or water saturation can be obtained (Gregory, 1976 and 1977; Hampson and Russell, 1990; Hampson-Russell Software Service Ltd., 1991). Petrel Robertson Ltd. (1991) undertook a study of pore shape effect on Poisson's ratio for gas-saturated carbonate using Toksöz theory.

1.6 Hardware and software used

All seismic data processing undertaken in this thesis was performed using Landmark/ITA Insight software (Landmark/ITA, 1992) on Sun Workstations at the Department of Geology and Geophysics, The University of Calgary.

Most synthetic data were created by using the software of Dr. D.C. Lawton (The University of Calgary) based upon the Zoeppritz equations. Zoeppritz plot in Figure 2.8 was created by using the code of Dr. P.P.C. Wu (The University of Calgary) based on the plane solutions to the Zoeppritz equations. The amplitude picking program was developed using the Matlab software. The 'block-shift' NMO correction program was developed in FORTRAN, and compiled on the Sun Workstations.

The text, tables and figures were created on an Apple Macintosh IIsx computer using Microsoft Word, Expressionist, Cricket Graph, Adobe Photoshop and Canvas software packages.

Chapter 2: Physical seismic modeling

2.1 Introduction

Chapter 1 outlines the Canadian Beaufort Sea as a marine environment with high-velocity, ice-bearing permafrost near the sea floor. The presence of the permafrost layers makes it difficult to image all other deeper reflectors. In this chapter, a study of multiconverted reflections is presented using both physical and numerical modeling approaches. The purpose of this modeling study is to determine whether multiconverted reflections could provide better images of deeper reflectors, particularly from the top of the second layer of the ice-bearing permafrost. Also in this study, AVO (amplitude-versus-offset) analysis was undertaken for both the physical and numerical data.

Physical modeling is an effective way for assisting seismic studies in environments containing permafrost. Cheadle (1988) developed a modeling tank system that was used to generate acoustic data over models of ice-bearing permafrost. His modeling results suggested that reflections from the base of the ice-bearing permafrost layers are particularly difficult to image using single-mode (P) reflections. However, one of the difficulties in physical modeling is a limitation in the range of physical properties of available materials. It is often impossible to find a material whose velocity matches the velocity in the field exactly, and there is a limit to how much detail we can put in models. For example, as discussed by Poley and Lawton (1991), the velocity of the ice-bearing permafrost may be transitional rather than abrupt. Therefore, the limitation for the modeling is the difficulty in finding materials in the laboratory with a transitional velocity change instead of an abrupt one.

As discussed by Poley and Lawton (1991), there are several layers of permafrost in the Canadian Beaufort Sea. The first two ice-bearing permafrost layers are called *D6* and *D5*, respectively. Poley and Lawton (1991) showed the strong effect of *D6* on *D5* in terms of reflection amplitude and phase. Cheadle (1988) built a physical model with

layers of permafrost represented by two or three layers of Plexiglas suspended in water. The water between the Plexiglas layers was used to represent the low-velocity, unfrozen layers. In the research carried out for the present thesis, a similar model was built, but the data were recorded with a different acquisition geometry than that used by Cheadle (1988).

The physical models were scaled to field units by using the scaling factors shown in Table 2.1. Distance- and time-scale factors used were both 1:5,000, and the velocity scale factor was 1:1. Layer 2 of the model was 0.62 cm thick for all models, resulting in a layer 31 m thick after scaling, which is an average thickness of the *D6* layer in the Beaufort Sea (Poley and Lawton, 1991). The distance from the source to the top of the second layer was 8.2 cm, which is 410 m after scaling. This depth was chosen to minimize noise from the reverberating tail of the direct arrival between the source and receiver transducers. It is a reasonable depth as permafrost is known to occur from 10 to 600 m depth in the Beaufort Sea (Poley et al., 1989).

Table 2.1 Scaling factors used for physical modeling

Parameter	Scale factor	Model	Field
Distance	5000	1 cm	50 m
Time	5000	100 nsec	0.5 ms
Velocity	1	2740 m/s	2740 m/s
Frequency	1/5000	250 kHz	50 Hz

2.2 Model construction

Eight models were constructed using several different materials available in the physical seismic modeling laboratory at The University of Calgary. All these models have four layers, as shown in Figure 2.1. Both layer 1 and layer 3 are water layers, representing the low-velocity, unconsolidated sediments above and below the high-velocity ice-bearing permafrost horizons in the Canadian Beaufort Sea (layer 2 and layer 4). Layer 2 is the high-velocity shallow layer (*D6* in Poley and Lawton, 1991), and layer 4 is the layer to be imaged (*D5* in Poley and Lawton, 1991). Five different materials (aluminum, Trabond, Plexiglas, polystyrene, and PVC Foam) were chosen for layer 2, whereas layer 4 was made of four different materials (aluminum, Plexiglas, polystyrene, and orthodic foam). These materials possess a range of physical properties, as listed in Table 2.2 and Table 2.3.

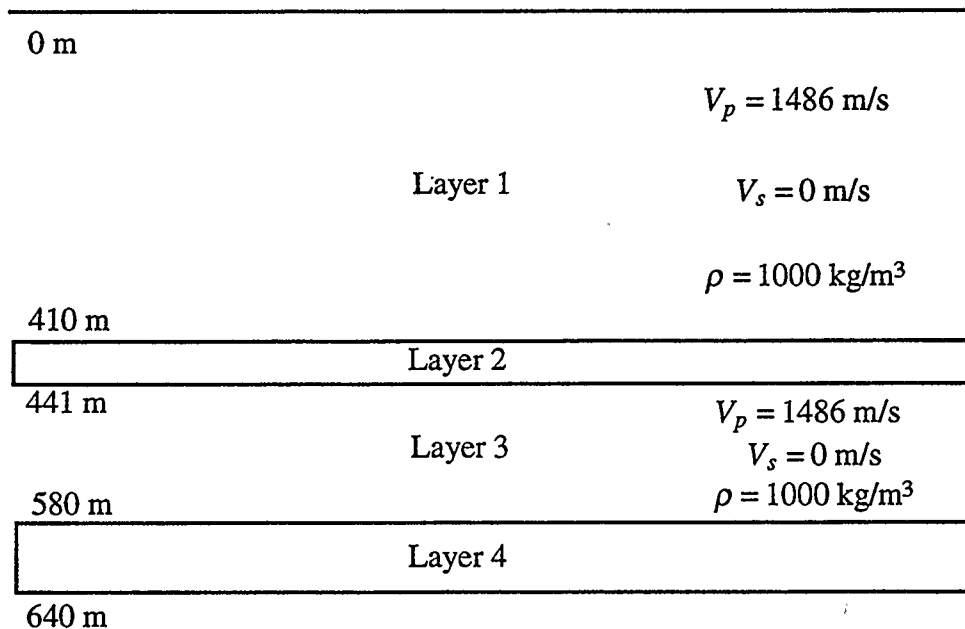


FIG. 2.1. Schematic diagram of the physical model. Both layer 1 and layer 3 are water layers. Layer 2 and layer 4 are solid layers; V_p = P-wave velocity; V_s = S-wave velocity; ρ = density. Dimensions are given in field units.

The P-wave and S-wave velocities of all materials listed in Tables 2.2 and 2.3 were measured in the laboratory by using cylindrical transducers, and Poisson's ratio was calculated by using equation (1.3). Density was obtained from measured weight and volume for each sample of different materials. The P-wave velocity of aluminum (6004 m/s) is very high compared with the P-wave velocity in water (1486 m/s), hence a large acoustic-impedance difference occurs between water and aluminum. In comparison, the P-wave velocities of Trabond (3010 m/s) and Plexiglas (2740 m/s) are about the same as that of ice-bearing permafrost (around 3000 m/s) in the Canadian Beaufort Sea. Polystyrene has a P-wave velocity of 2063 m/s, which is lower than that of frozen sediments, whereas PVC Foam and orthodic foam have P-wave velocities of only 1069 m/s to 1100 m/s, which are lower than that of water. In marine environments, it is not common for any layer to have a lower P-wave velocity than that of water. However, by studying this particular model, the results may be compared with other models, and may be used for studying multiconverted reflections in non-marine environments, such as the Canadian Rocky Mountain Foothills area.

Table 2.4 lists normal reflection coefficients (R_0) for all layer-2 materials (layer 1 is a water layer). The P-wave velocity of permafrost is expected to be around 3000 m/s, and with a density about 2000 kg/m³ (Poley, 1987). Hence R_0 is around 0.60. In Table 2.4, P-wave velocities and normal reflection coefficients (R_0) for Trabond and Plexiglas are close to those of permafrost. Hence a model with Trabond or Plexiglas as layer 2 is a good representative for the geology of the Canadian Beaufort Sea, whereas models with other materials can be used to investigate other geological situations where velocity inversions occur.

Table 2.2 Physical properties and parameters of layer 2

Compound	Thickness (actual, cm)	Thickness (scaled, m)	V_p (m/s)	V_s (m/s)	σ	ρ (kg/m ³)
Aluminum	0.62	31	6004	3029	0.33	2640
Trabond	0.62	31	3010	1733	0.25	1210
Plexiglas	0.62	31	2740	1385	0.33	1200
Polystyrene	0.62	31	2063	846	0.40	1030
PVC Foam	0.62	31	1100	740	0.10	670

Table 2.3 Physical properties and parameters of layer 4

Compound	Thickness (actual, cm)	Thickness (scaled, m)	V_p (m/s)	V_s (m/s)	σ	ρ (kg/m ³)
Aluminum	1.2	60	6004	3029	0.33	2640
Plexiglas	1.2	60	2740	1385	0.33	1200
Polystyrene	1.2	60	2063	846	0.40	1030
Orthodic foam	1.2	60	1069	591	0.28	160

Table 2.4 R_0 for all layer 2 (layer 1 is water layer)

Material	V_p (m/s)	ρ (kg/m ³)	R_0
Aluminum	6004	2640	0.83
Trabond	3010	1210	0.42
Plexiglas	2740	1200	0.38
Polystyrene	2063	1030	0.18
PVC Foam	1100	670	-0.34

2.3 Data acquisition

For the acoustic experiments, all the models were put in the water-filled seismic modeling tank, 2 meters deep by 3 meters wide by 4 meters long. The data were collected using small, spherical transducers as source and receiver. Both source and receiver transducers were mounted on long carriages which move on separate beams. Carriages and beams are moved in both x and y directions using stepping motors. The data acquisition system includes a pulse generator, the digital storage oscilloscope (Nicolet 2090), a digital delay unit and a receiver preamplifier (Cheadle, 1988). The motors, as well as the data acquisition components, are controlled by a computer terminal (Cheadle, 1988). The collected data were transferred to Landmark/ITA seismic processing system on Sun Workstations for subsequent processing.

One difficulty during data acquisition is the maintenance of the wavelet shape. In acoustic physical modeling, both the source and receiver transducers are put in the water. Because of the omnidirectional response of these transducers, the direct arrival has a very high amplitude, and the wavelet tail of the direct arrival is very long. In order to eliminate this long tail of the direct arrival, a baffle was used on the source. It was found that this is an effective way to suppress the long tail of the wavelet. However, the wavelet shape is sensitive to the baffle position, and the baffle also introduces a small change in the directivity response of the transducer, which may cause some problems in detailed amplitude analysis of the data.

Eight models were constructed, and were divided into two groups. In group 1, models have the same layer 4 (aluminum) whereas in group 2, models have the same layer 2 (Plexiglas). Results for both groups are described in section 2.5. The recording geometry used in the experiments is shown in Table 2.5. A total of eight gathers were collected over these physical models. All shot gathers were collected using an end-on geometry, with a total of 150 traces in each gather.

Table 2.5 Geometry used for the seismic physical modeling experiments

Parameter	Field	Model
Number of shots	8	8
Traces/shot	150	150
Near offset	60 m	1.2 cm
Far offset	1550 m	31 cm
Group interval	10 m	0.2 cm
Central Frequency	50 Hz.	250 kHz.
Samples	4096	4096
Sample rate	0.5 msec	100 nsec

2.4 Numerical modeling

Interpretation of the physical modeling results was assisted and verified by computing synthetic seismograms for equivalent models. These seismograms are also shown and discussed in section 2.5. The purpose of computing synthetic seismograms was to verify the physical modeling results in terms of traveltime and amplitude of events. Additional synthetic data which are shown in chapter 3 were used to study the amplitudes of multiconverted reflections for numerical models that did not have a physical equivalent.

The numerical modeling program was based on plane wave solutions to the Zoeppritz equations. Reflection coefficients calculated from the Zoeppritz equations were convolved with a Ricker wavelet with a central frequency of 50 Hz. Transmission losses and geometrical spreading were calculated for the synthetic data, but attenuation was not. The direct arrival was not calculated for the synthetic seismograms either.

2.5 Results

In this section, all physical and numerical modeling results are plotted with true amplitudes with no time-variant scaling or trace balancing applied. All physical modeling data were recorded with the baffle on the source transducer. Therefore, the first arrivals on all shot gathers have a relatively small amplitude, and the tail of the wavelet is much shorter than if the baffle was not used.

2.5.1 Group 1

Group 1 contains five models, all of which have aluminum as layer 4. Five different shallow layers (layer 2) are comprised of Plexiglas, PVC Foam, polystyrene, Trabond and aluminum. This group of models examines the reflectivity of a very high-impedance basal layer below a shallow velocity inversion. Figure 2.2 shows the shot gather for Plexiglas used as layer 2. Identification of events in Figure 2.2a was assisted by computing a numerical synthetic seismogram of the same model. This seismogram is shown in Figure 2.2b. Events labeled PP and PPPP in Figure 2.2 refer to the P-wave reflections from the top and the base of layer 2, respectively. Event PPPPPP refers to the P-wave reflection from the top of layer 4, and PSSP is the multiconverted reflection from the base of layer 2.

In both the physical and numerical modeled seismograms (Figure 2.2), the P-wave reflection from the top of layer 2 (PP) diminishes almost to zero at the middle offset. This is due to the fact that the incident P-wave reaches critical angle between water and Plexiglas before the middle offset (about 500 m). At larger offsets, efficient conversion and transmission of S-wave energy into the thin Plexiglas layer occurs. This converted energy is reflected from the bottom of layer 2, and it is converted back to a P-mode at the top of layer 2, resulting in the PSSP multiconverted reflection which is identified in both Figures 2.2a and 2.2b. The S-wave energy in layer 2 is also reconverted to a P-wave upon transmission through the base of layer 2. Double mode-conversion also occurs for

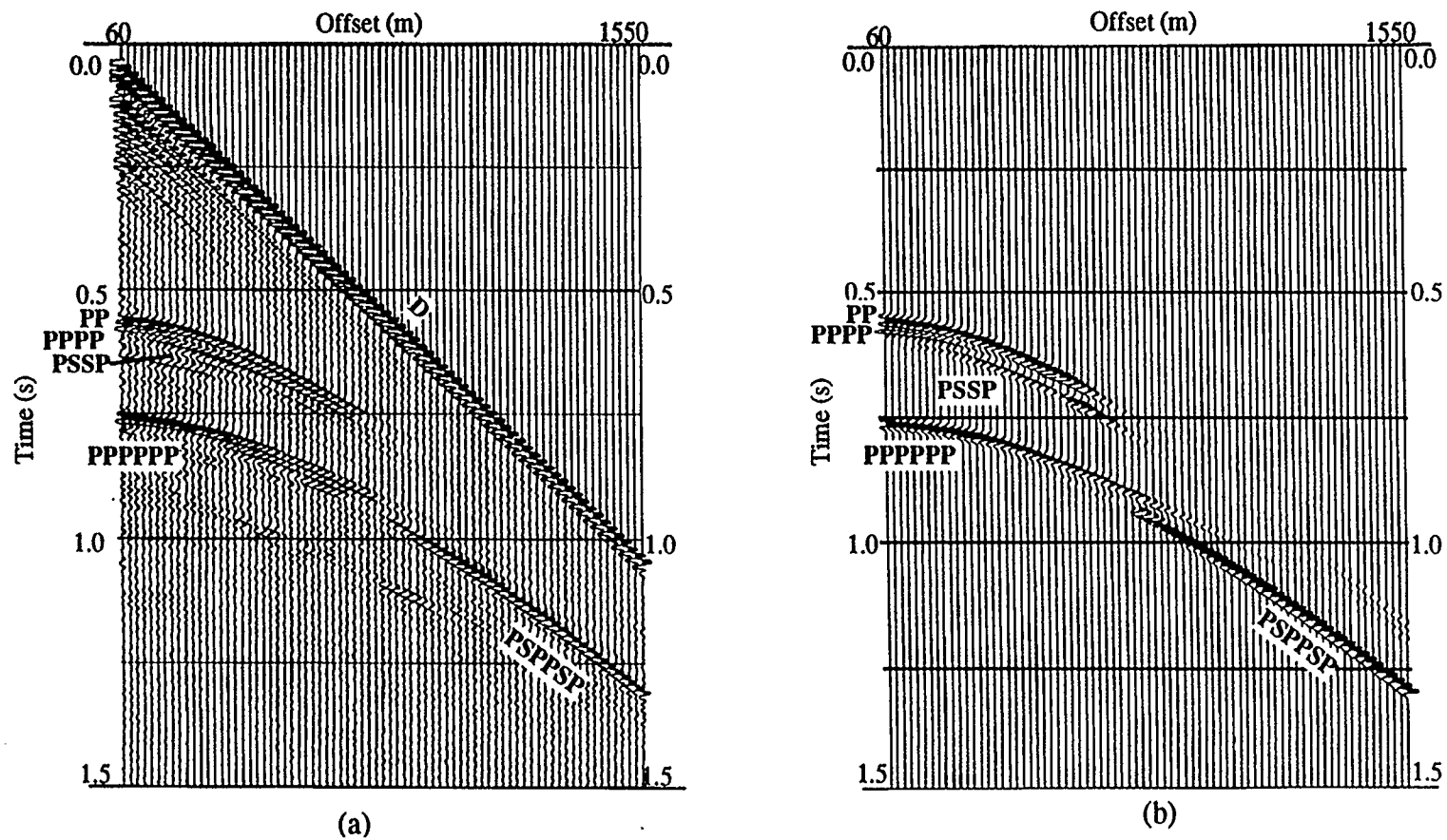


FIG. 2.2. A shot gather (a) and its synthetic seismogram (b) for model 1-1. D = direct arrival; PP = P-wave reflection from the top of layer 2 (Plexiglas); PPPP = P-wave reflection from the bottom of layer 2; PSSP = multiconverted reflection from the bottom of layer 2; PPSPP = P-wave reflection from the top of layer 4 (aluminum); PPSPP = multiconverted reflection from the top of layer 4.

the P-wave energy reflected off the top of the underlying layer 4, resulting in the high-amplitude PSPPSP arrival identified on far offset traces in Figures 2.2a and 2.2b.

In contrast, when the shallow velocity inversion is removed and layer 2 is replaced by low-velocity PVC Foam, a uniformly decreasing PP event amplitude from the top of layer 2 is obtained. Results for this model are shown in Figure 2.3a. The multiconverted PSPPSP event is not present because of the fact that the P-wave velocity in PVC Foam is lower than that in water. Therefore, there is no critical angle for the incident P-wave, resulting in very little converted S-wave energy being transmitted into PVC Foam layer. This conclusion is confirmed by numerical modeling (Figure 2.3b). The difference between the physical modeling (Figure 2.3a) and the numerical modeling (Figure 2.3b) is that attenuation was not included in the numerical modeling. Therefore, a higher-amplitude event was obtained for the PPPP reflection for the numerically modeled seismogram (Figure 2.3b), compared with the physical modeling case (Figure 2.3a).

Figure 2.4a shows the physical modeling results when polystyrene is used as layer 2. As for the Plexiglas case (Figure 2.2a), all major events (PP, PPPP, PSSP, PPPPPP, and PSPPSP) are identified on the gather and verified with numerical modeling (Figure 2.4b). Furthermore, a PSPP (or PPSP) event is identified on these gathers. The physical modeling data (Figure 2.4a) and the numerical modeling data (Figure 2.4b) match very well in terms of the traveltime and amplitude for all of the events identified. Also from both gathers, it is clear that the P-wave reflection from the top of layer 2 (PP) reaches the maximum amplitude just beyond the middle offset position, which is the critical distance for a P-wave incident on the top of layer 2. After passing the critical distance, the PP event amplitude decreases but not as rapidly as for the Plexiglas model (Figure 2.2). The reflection from the top of layer 4 (PPPPPP) shows a uniform decrease in amplitude with offset, as predicted by numerical modeling results (Figure 2.4b). Comparing Figures 2.2

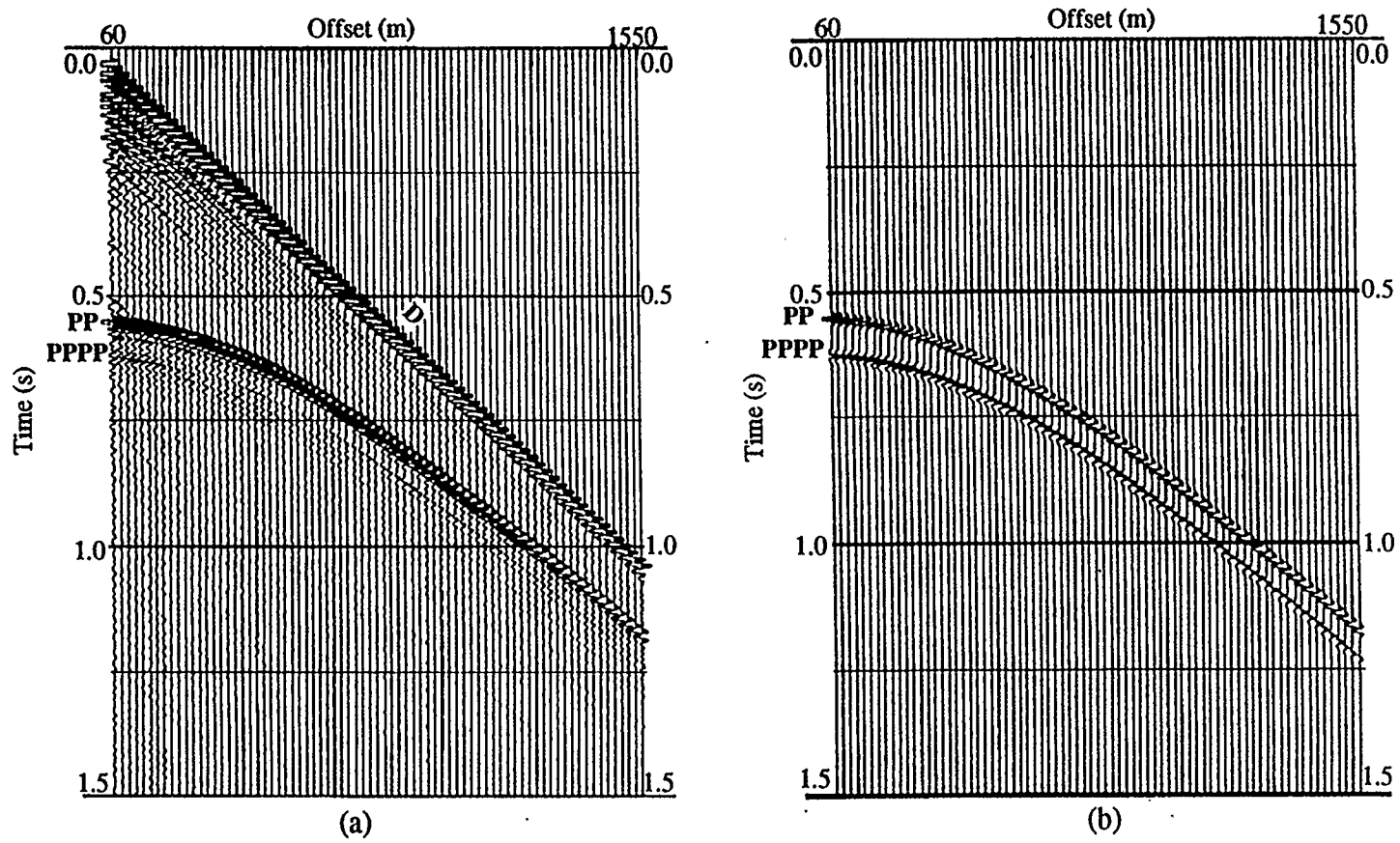


FIG. 2.3. A shot gather (a) and its synthetic seismogram (b) for model 1-2. D = direct arrival; PP = P-wave reflection from the top of layer 2 (PVC Foam); PPPP = P-wave reflection from the bottom of layer 2.

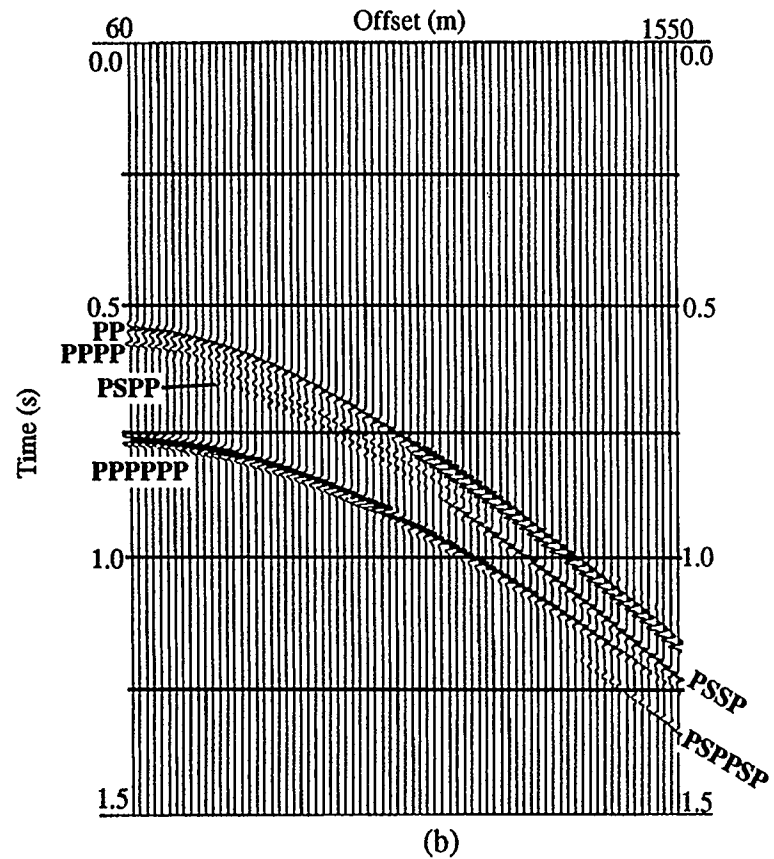
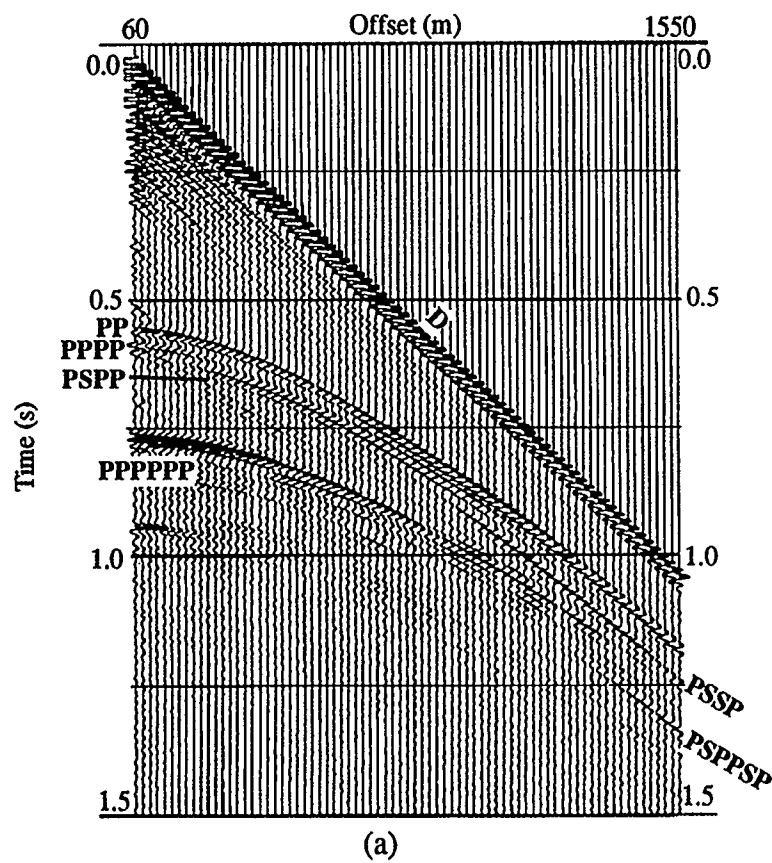


FIG. 2.4. A shot gather (a) and its synthetic seismogram (b) for model 1-3. D = direct arrival; PP = P-wave reflection from the top of layer 2 (polystyrene); PPPP = P-wave reflection from the bottom of layer 2; PSPP = multiconverted reflection from the bottom of layer 2; PPSPP = multiconverted reflection from the bottom of layer 2; PPSPP = P-wave reflection from the top of layer 4 (aluminum); PSSP = multiconverted reflection from the top of layer 4.

and 2.4, it is clear that the amplitude of PSPPSP reflection in Figure 2.4 is lower than that shown in Figure 2.2 for the same range of offset. This is because the S-wave velocity of polystyrene (846 m/s) is much lower than the P-wave velocity in water (1486 m/s), whereas the S-wave velocity of Plexiglas (1385 m/s) is closer to the P-wave velocity in water. Therefore, not as much PSPPSP energy propagates through layer 2 when it is composed of polystyrene rather than Plexiglas.

The model with Trabond used for layer 2 yields results shown in Figure 2.5, which are rather similar to the Plexiglas case (Figure 2.2). In Figure 2.5a, single-mode reflections (PP, PPPP, PPPPPP) and multiconverted modes (PSPP, PSPPSP) are identified by comparison with a synthetic seismogram (Figure 2.5b). However, the P-wave and S-wave velocities of Trabond are higher than for Plexiglas. The absolute difference between the S-wave velocity in layer 2 and the P-wave velocity in water for Plexiglas is much smaller than that for Trabond. Therefore, for the same offset, the PSPPSP energy is higher for model 1-1 (in Figure 2.2) than for model 1-4 (in Figure 2.5).

We also notice that the synthetic seismogram in Figure 2.5b is not as good a match to the physical modeling data (Figure 2.5a), comparing with the Plexiglas case (Figure 2.2). In the laboratory, Trabond was made of Trabond powder, glass beads and water, which were mixed in a prescribed ratio. Then it was cured in the laboratory for a few days under the normal temperature and pressure. The physical properties could be different between a fresh Trabond sample and a cured one. This may be one factor causing the difference between the physical modeling results (Figure 5.4a) and numerical modeling results (Figure 2.5b).

Figure 2.6 shows the physical modeling (Figure 2.6a) and numerical modeling (Figure 2.6b) results for the extreme case when aluminum was used as layer 2. From the data in Table 2.2, it is clear that both the P-wave and S-wave velocities of aluminum are much higher than the P-wave velocity in water. Therefore, a strong screening effect

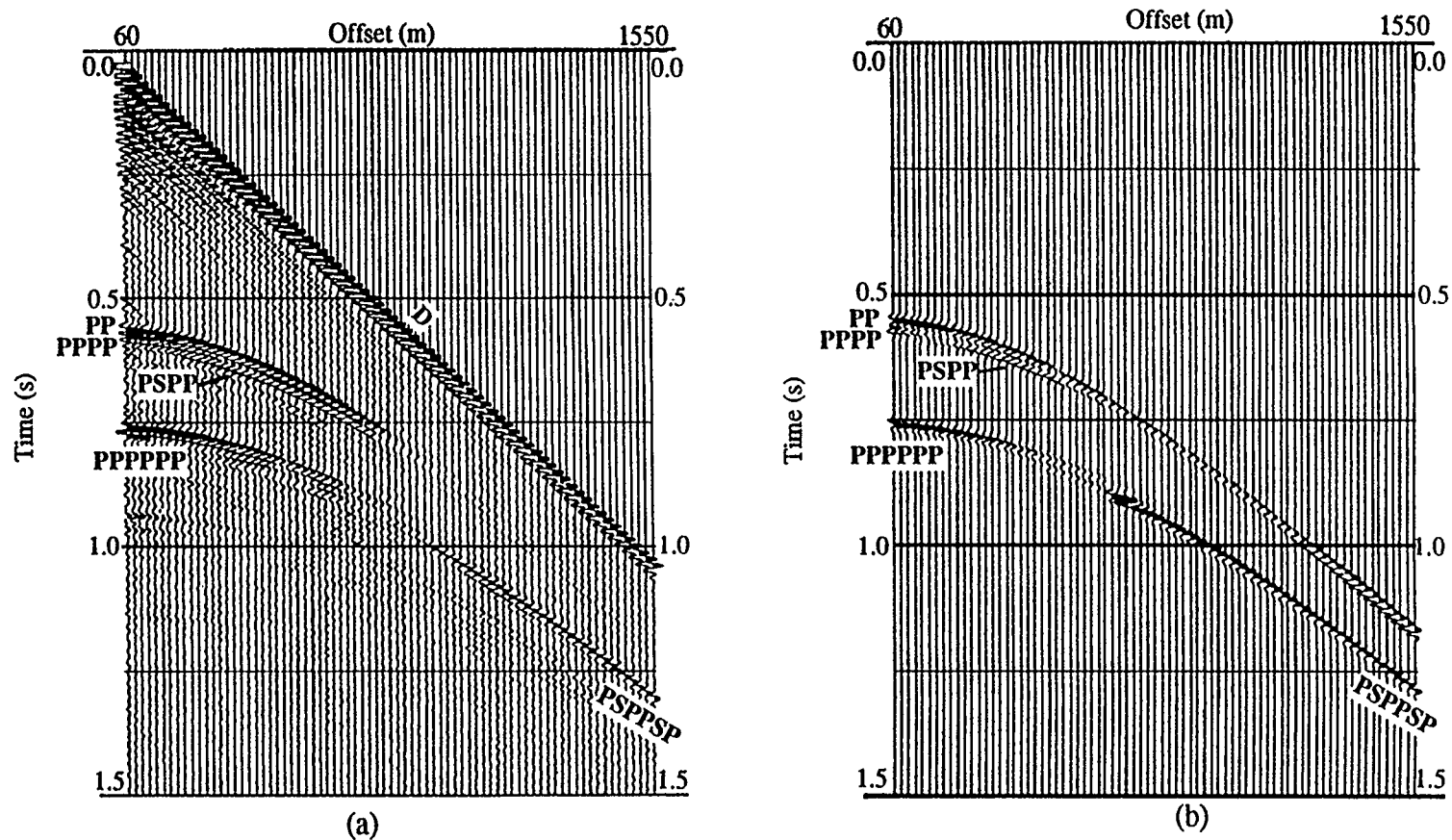


FIG. 2.5. A shot gather (a) and its synthetic seismogram (b) for model 1-4. D = direct arrival; PP = P-wave reflection from the top of layer 2 (Trabond); PPPP = P-wave reflection from the bottom of layer 2; PSPP = multiconverted reflection from the bottom of layer 2; PPSPP = P-wave reflection from the top of layer 4 (aluminum); PSPPSP = multiconverted reflection from the top of layer 4.

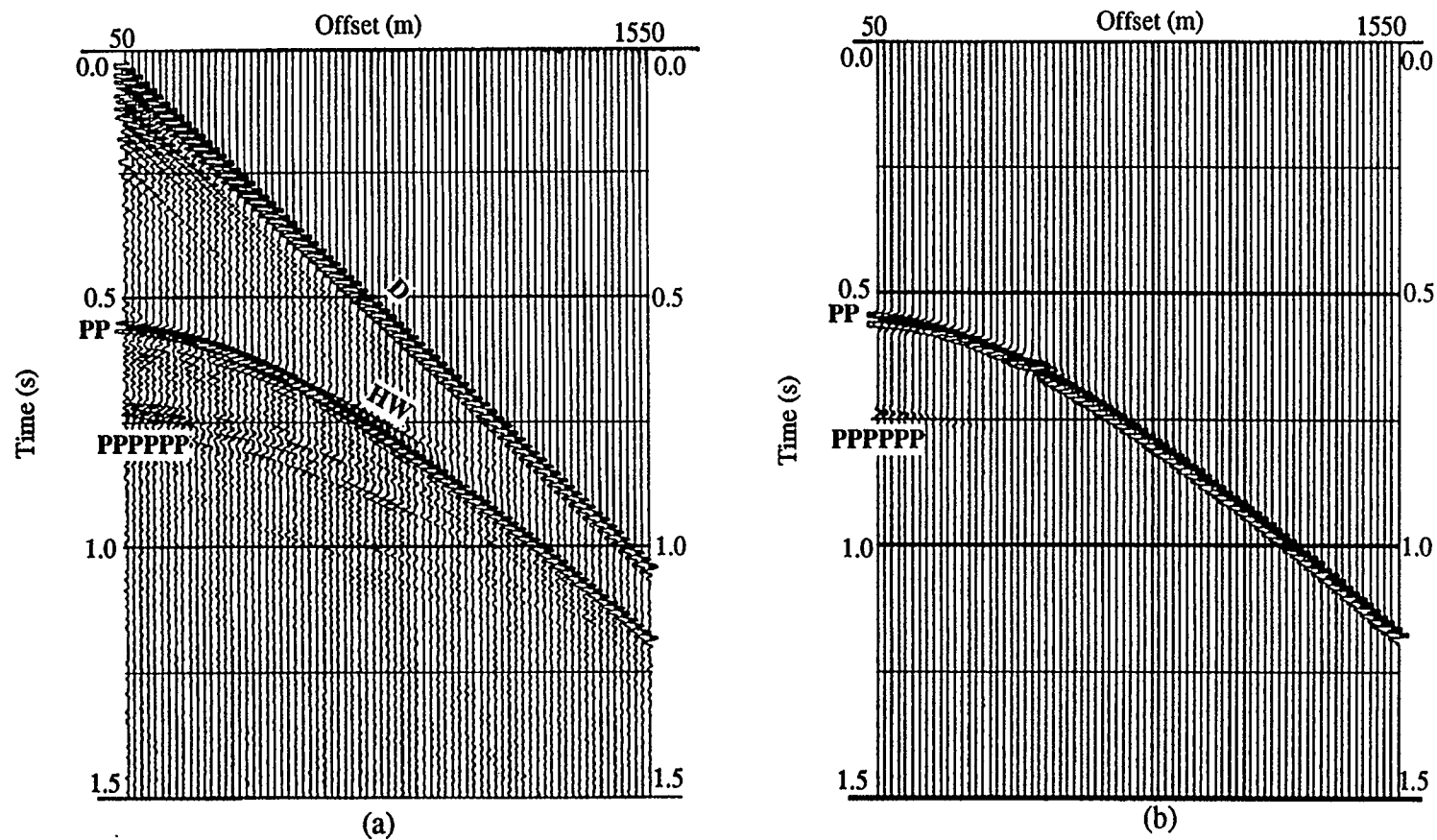


FIG. 2.6. A shot gather (a) and its synthetic seismogram (b) for model 1-5. D = direct arrival; PP = P-wave reflection from the top of layer 2 (aluminum); PPPPPP = P-wave reflection from the top of layer 4; HW: = shear head-wave.

occurs. Because of a large reflection coefficient, most energy is reflected from the top of layer 2 (PP mode), and thus P-wave reflections from deeper interfaces (e.g., PPPPPP) almost cannot be identified. In Figure 2.6a, a head wave is also identified at about the middle offset position. Energy with linear moveout showing the head wave separating from the reflection trajectory can be identified. The slope of the reflection arrival is approximately 0.323 ms/m, corresponding to an apparent velocity of approximately 3096 m/s, which is about the same as that of the S-wave velocity in aluminum (3029 m/s). Therefore, this head wave is a converted head wave (PSP). The incident P-wave reaches the critical angle at 29° at the top of aluminum, it is then converted to S-wave. The converted S-wave travels along the surface of aluminum, then is converted back to P-wave to create a PSP head wave raypath.

2.5.2 Group 2

In section 2.5.1, all models with the same material (aluminum) for layer 4 were discussed. In this section, results for models with the same layer 2 material (Plexiglas) are discussed. Four different materials were used as layer 4 in this group: aluminum (model 1-1, Figure 2.2), Plexiglas (Model 2-1, Figure 2.7), polystyrene (Model 2-2, Figure 2.9), and orthodic foam (Model 2-3, Figure 2.10).

Figure 2.7 shows the physical modeling (Figure 2.7a) and numerical modeling (Figure 2.7b) results when Plexiglas is used as layer 4. Single-mode reflections (PP, PPPP, and PPPPPP) can be identified, but the multiconverted reflection (PSPPSP) is not clear in Figure 2.7 as it is in Figure 2.2. In order to understand why the PSPPSP in Figure 2.7a is not as clear as in Figure 2.2a, numerical modeling was undertaken by using solutions to the Zoeppritz equations. Figure 2.8 is the plot of amplitude versus incidence angle. Amplitude refers to the absolute value of the displacement reflection coefficient, and the angle refers to the incidence angle for the first Plexiglas layer. Four different layers with varying P-wave velocity (4000 m/s, 2740 m/s, 2500 m/s, 2000 m/s), but with

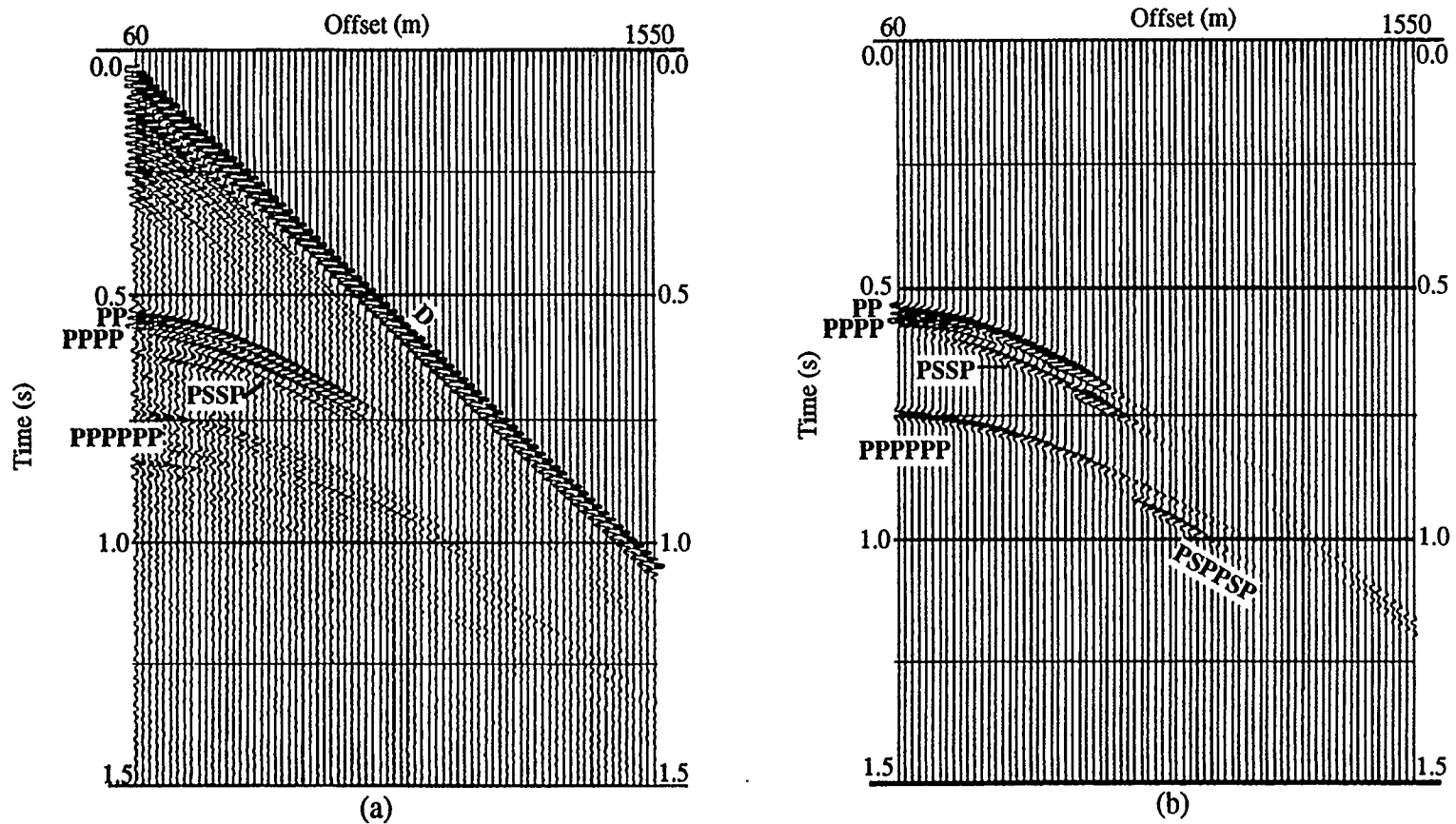


FIG. 2.7. A shot gather (a) and its synthetic seismogram (b) for model 2-1. D = direct arrival; PP = P-wave reflection from the top of layer 2 (Plexiglas); PPPP = P-wave reflection from the bottom of layer 2; PSSP = multiconverted reflection from the bottom of layer 2; PPPPPP = P-wave reflection from the top of layer 4 (Plexiglas); PSPPSP = multiconverted reflection from the top of layer 4.

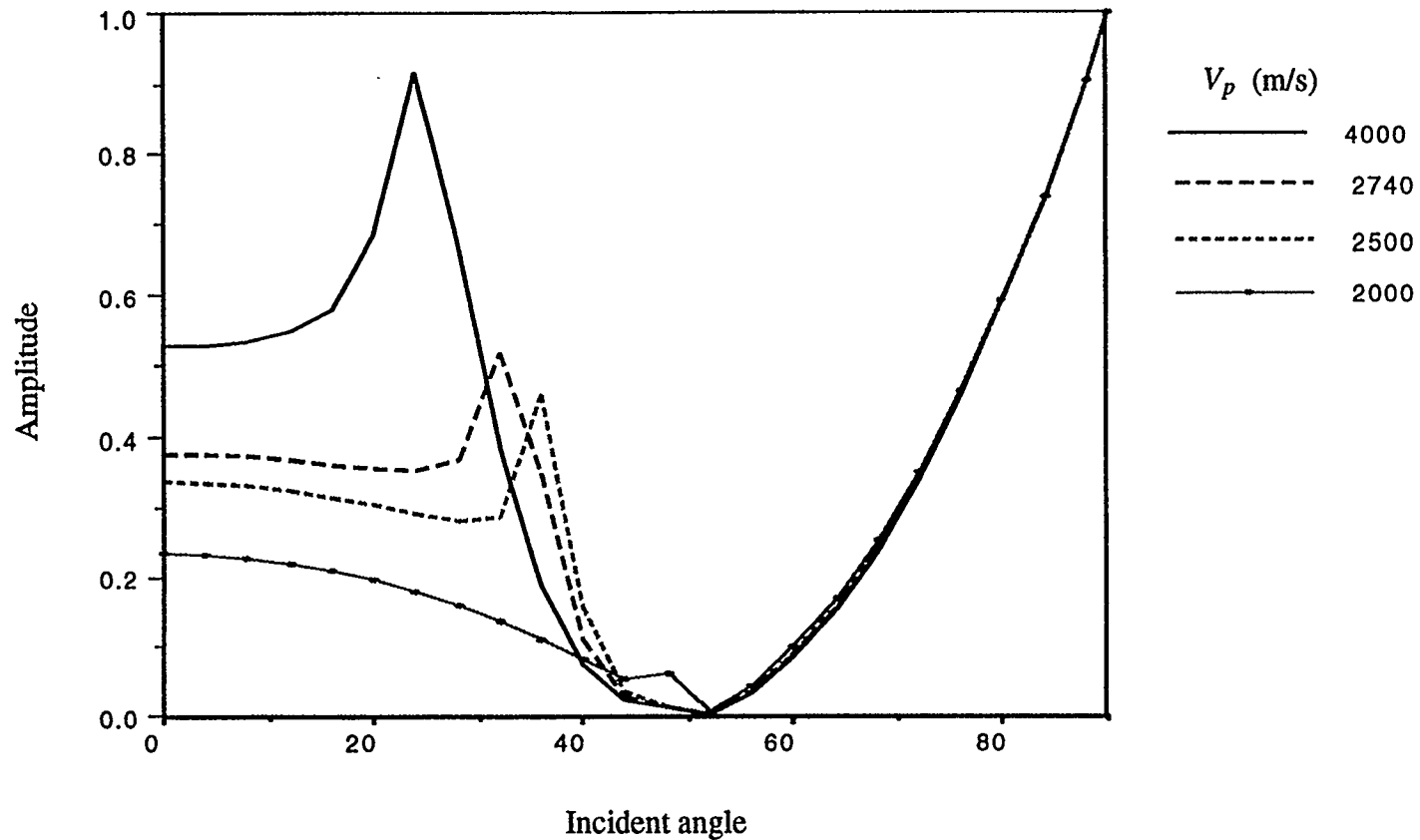


FIG. 2.8. Reflection amplitude versus incident angle plots for layer 2 with the same S-wave velocity (1380 m/s), and with P-wave velocity varying from 2000 m/s to 4000 m/s. Amplitude refers to the absolute value of the displacement reflection coefficient, the incident angle refers to the P-wave incident angle upon layer 2.

the same S-wave velocity (1380 m/s) were chosen. The result shows that amplitudes for different P-wave velocity reaches almost zero for incidence angles between 40 degree and 60 degree. That is true if the S-wave velocity is 1380 m/s. For model 2-1, since two layers of Plexiglas were used, the incidence angle on the second layer of Plexiglas and that on the first layer are the same. Therefore, there is not much reflected PSPPSP reflection at the far offset in Figure 2.7a.

As mentioned earlier, model 2-2 (Plexiglas for layer 2, and polystyrene for layer 4) is the best representative for the shallow stratigraphy in the Canadian Beaufort Sea. The shot gather recorded over this model is shown in Figure 2.9a. Single-mode reflections (PP, PPPP, PPPPPP) and multiconverted reflection (PSSP, PSPPSP) are all identified in the shot gather, and are verified by the synthetic seismogram (Figure 2.9b). It is interesting to note that the PSPPSP reflection on the far-offset traces is similar in energy to the PPPPPP event on the near-offset traces. This suggests that a better image of the top of layer 4 could be obtained by using the multiconverted reflection (PSPPSP) than the single-mode reflection (PPPPPP).

Comparing Figure 2.2a and Figure 2.9a, it is obvious, as expected, that the best image of the top of layer 4 can be obtained when it has a high P-wave velocity. This is true because when the P-wave velocity of the imaged layer is higher, the absolute value of acoustic impedance difference between water (layer 3) and the imaged layer (layer 4) is greater. In Model 2-3, orthodic foam, with a very low P-wave velocity, was used for layer 4, and results are shown in Figure 2.10a. Single-mode reflections (PP, PPPP, PPPPPP) and multiconverted reflection (PSPPSP) were identified (Figure 2.10a), by comparison with a synthetic seismogram (Figure 2.10b). In Figure 2.10a, the *B* refers to the reflection from the base of the orthodic foam. Since the density of orthodic foam (160 kg/m^3) is lower than that of water, it will tend to float on water. To stabilize the model, another piece of aluminum was bonded at the bottom of model to keep it

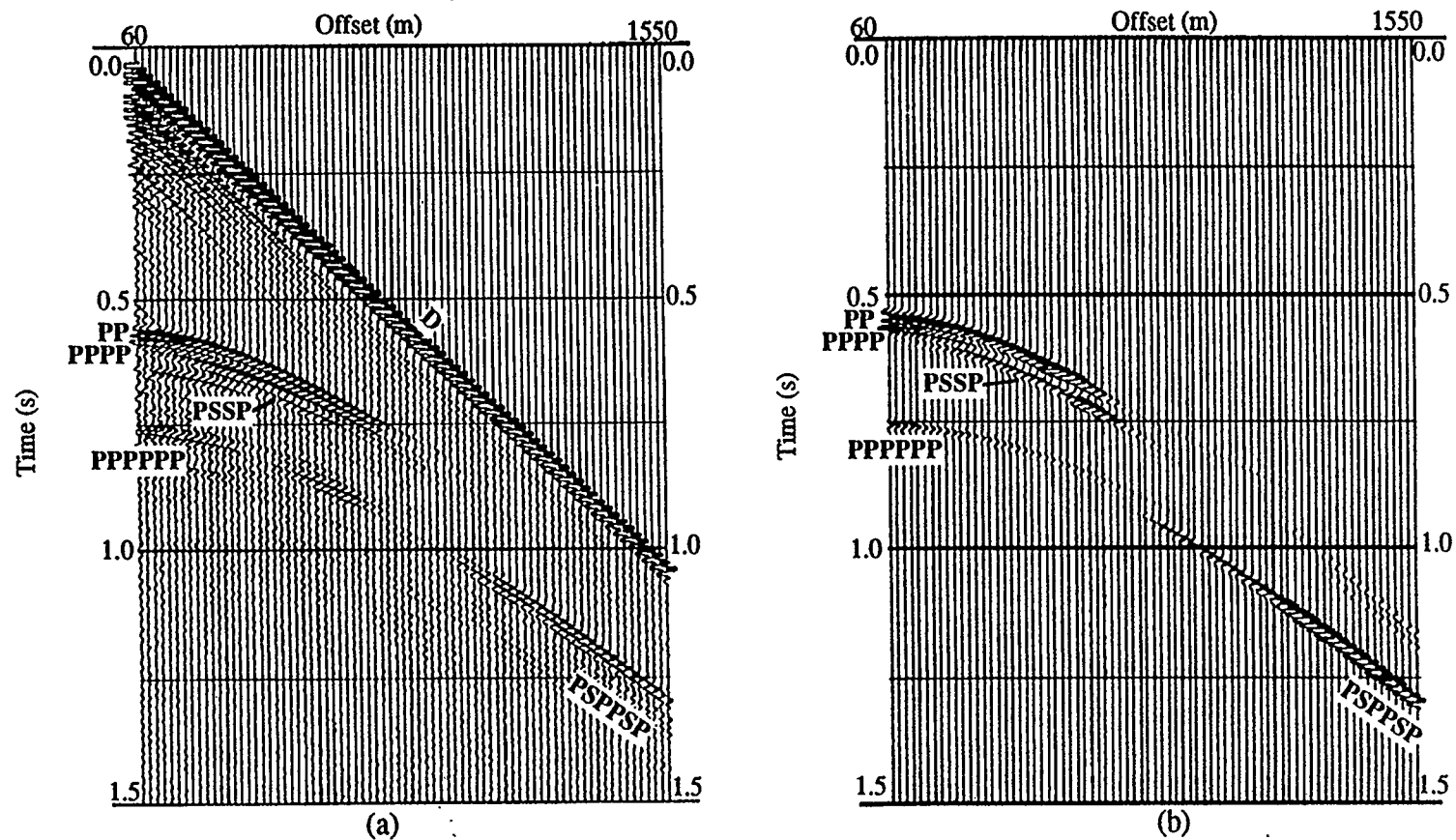


FIG. 2.9. A shot gather (a) and its synthetic seismogram (b) for model 2-2. D = direct arrival; PP = P-wave reflection from the top of layer 2 (Plexiglas); PPPP = P-wave reflection from the bottom of layer 2; PSSP = multiconverted reflection from the bottom of layer 2; PPSPPP = P-wave reflection from the top of layer 4 (polystyrene); PSPPSP = multiconverted reflection from the top of layer 4.

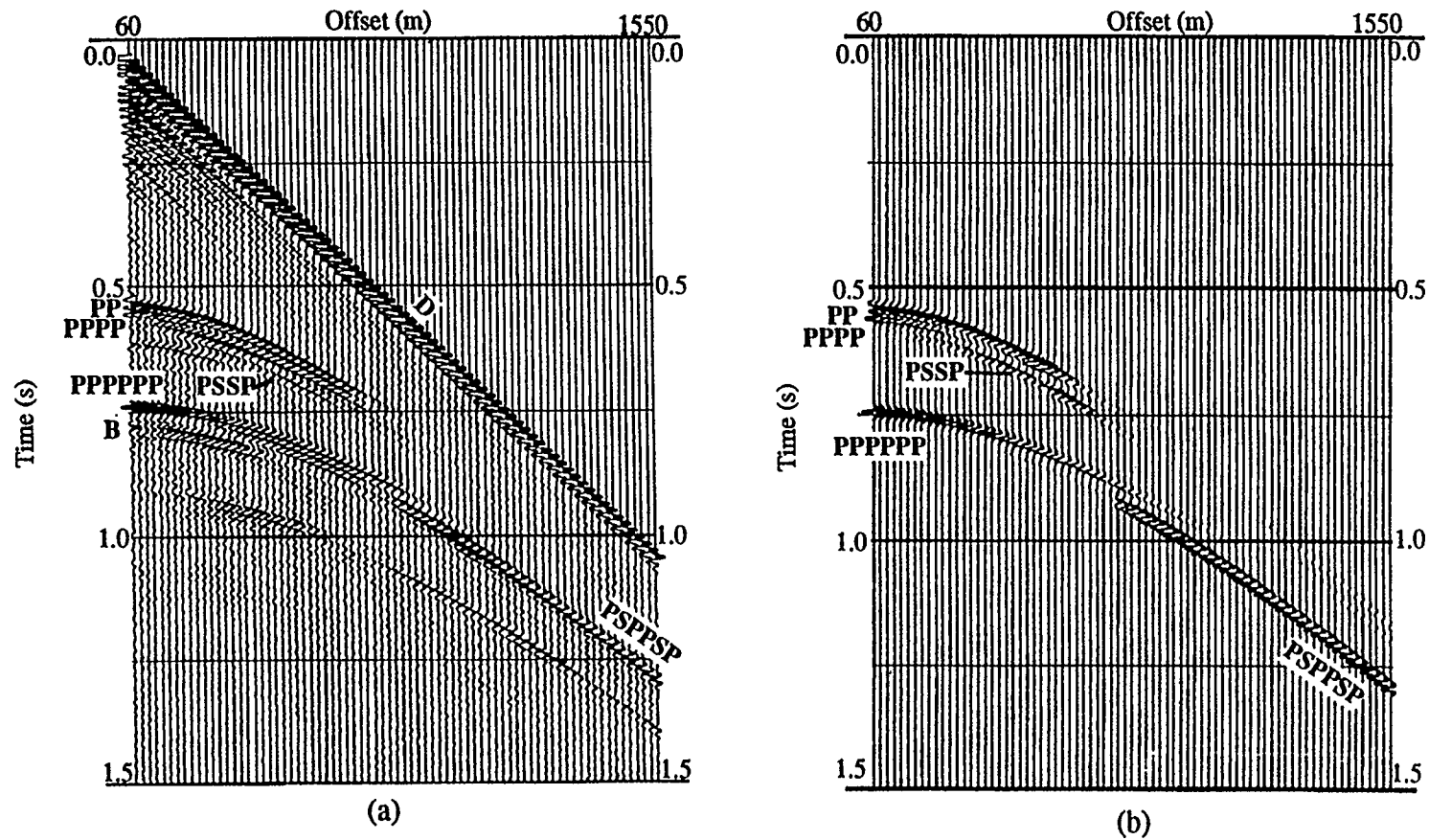


FIG. 2.10. A shot gather (a) and its synthetic seismogram (b) for model 2-3. D = direct arrival; PP = P-wave reflection from the top of layer 2 (Plexiglas); PPPP = P-wave reflection from the bottom of layer 2; PSSP = multiconverted reflection from the bottom of layer 2; PPSPPSP = P-wave reflection from the top of layer 4 (orthodic foam); B = P-wave reflection from the base of layer 4.

submerged. Since the P-wave velocity in aluminum is much greater than that in orthodic foam, the reflection at this interface (marked with *B* in Figure 2.10a) can be identified. This additional layer was not incorporated in the numerical model.

Also in Figure 2.10a, we can see a very strong PSPPSP event compared with the amplitude of this event in Figure 2.2a. This would imply that it should be easy to image the layer when its P-wave velocity is lower than that in water. This result may be applicable for low-velocity layers in nonmarine examples, especially when this imaged layer is a gas-saturated zone, since the P-wave velocity of a gas-saturated zone is usually lower than that of the surrounding rocks (Ostrander, 1984).

2.6 Conclusions

Both the physical and numerical modeling results suggest that the S-wave velocity in layer 2 and the P-wave velocity of layer 4 both contribute to the multiconverted PSPPSP reflection amplitude. Also, from the results of model 2-2 (Figure 2.9a), a higher-amplitude event for the top of layer 4 was obtained for the multiconverted reflection (PSPPSP), compared with the single-mode reflection (PPPPPP). Those results could be useful, since PPPPPP event on near traces could be dominated by noise, and the multiconverted reflection (PSPPSP) might be a more useful approach for imaging reflections below a shallow high-velocity layer.

Chapter 3: Numerical seismic modeling

3.1 Introduction

As discussed in chapter 2, one of the difficulties in physical modeling is a limitation in the range of physical properties of available materials. However, this is not the case for numerical modeling. One advantage of numerical modeling is that the physical parameters can be varied easily and it is therefore possible to study detailed models using numerical modeling techniques.

In chapter 2, some numerical modeling were undertaken to confirm the physical modeling results in terms of event identification as well as validating traveltime and amplitude. In this chapter, additional numerical modeling were undertaken to further study the effects which control multiconverted reflection (PSPPSP) amplitude. From the physical modeling results in chapter 2, it was concluded that the S-wave velocity of layer 2 and the P-wave velocity of layer 4 are two key parameters determining the amplitude of the multiconverted reflection (PSPPSP). It is necessary to study detailed effects by using synthetic data. For this study, five factors were considered, namely the S-wave and P-wave velocities of layer 2, the P-wave velocity of layer 4, and the thickness and the depth of layer 2.

3.2 Dependence on the S-wave velocity in layer 2

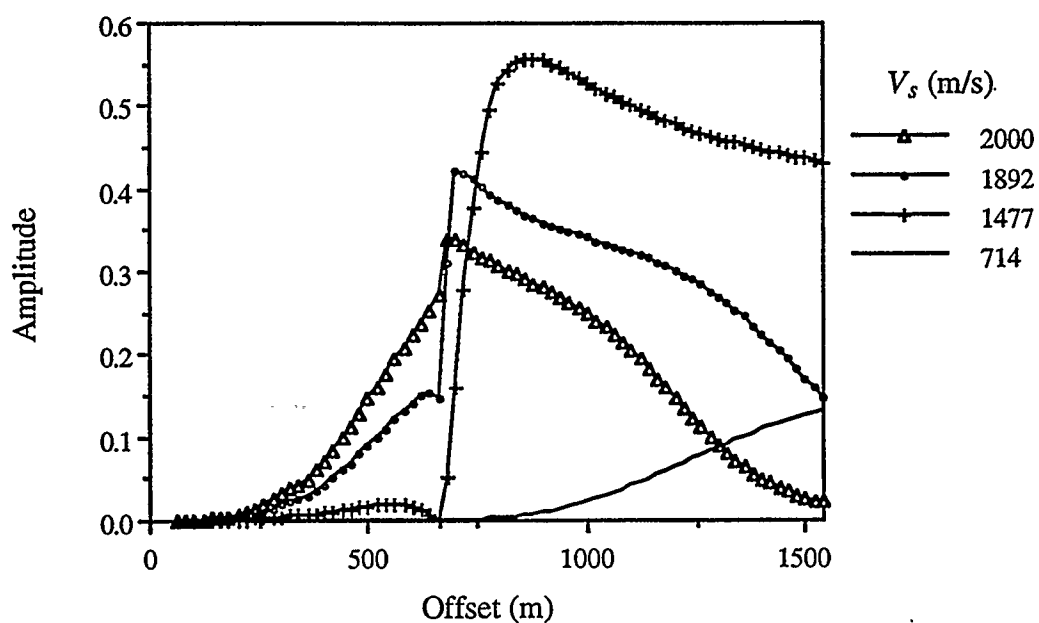
The cross-sectional profile of model 3-1 is shown in Figure 2.1. In this model, layer 1 and layer 3 are water layers, with P-wave and S-wave velocities of 1486 m/s and 0 m/s, respectively. P-wave and S-wave velocities of layer 4 are 6004 m/s and 3029 m/s, which are the same as those of aluminum. As discussed in chapter 2, when layer 2 was unchanged, the highest PSPPSP reflection amplitude was obtained with aluminum used as layer 4 when compared with other materials. For the additional numerical modeling,

the P-wave velocity in layer 2 was kept constant and S-wave velocity was varied as shown in Table 3.1.

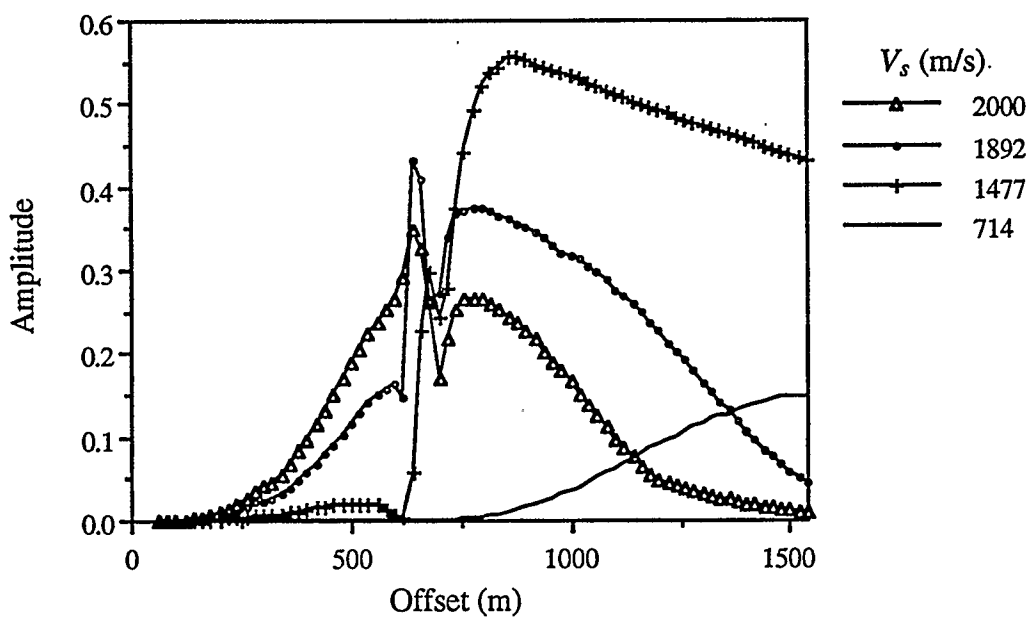
Table 3.1 Physical parameters for layer 2, model 3-1

Case	V_p (m/s)	V_s (m/s)	Poisson's ratio σ	ρ (kg/m ³)
1	3000	714	0.47	2000
2	3000	1477	0.34	2000
3	3000	1892	0.17	2000
4	3000	2000	0.10	2000

The P-wave velocity of layer 2 was kept constant at 3000 m/s, which is about the same as the P-wave velocity of ice-bearing permafrost in the Canadian Beaufort Sea. Shear-wave velocities for layer 2, ranging from 714 m/s to 2000 m/s, were chosen for studying the effect of the S-wave velocity of layer 2 on PSPPSP reflection energy from the top of layer 4. For each case in Table 3.1, PSPPSP reflection coefficients were obtained from the Zoeppritz equations, allowing for geometrical spreading and transmission losses. The amplitude-versus-offset plot is shown in Figure 3.1a, in which the vertical axis "amplitude" is the absolute value of the displacement reflection coefficient for a PSPPSP reflection, and the horizontal axis "offset" is the source-to-receiver distance. For each case in Table 3.1, synthetic seismograms were also generated by convolving the reflection coefficients with a Ricker wavelet with an appropriate phase shift applied. Then, the amplitudes of the PSPPSP event were picked to obtain an alternate amplitude-versus-offset diagram (Figure 3.1b). In Figure 3.1b, the vertical axis "amplitude" is the maximum positive value of a PSPPSP reflection event. Figures 3.1a and



(a)



(b)

FIG. 3.1. Amplitude-versus-offset for model 3-1. Layer 2 has a constant P-wave velocity (3000 m/s), and an S-wave velocity varying from 714 m/s to 2000 m/s. (a) Amplitude refers to the absolute value of the displacement reflection coefficient for P₁P₂P₁P₂P reflection calculated from Zoeppritz equations; (b) Amplitude is the maximum value picked from the synthetic seismogram.

3.1b were both generated in order to compare computed amplitudes with those which one would pick from a seismogram.

Theoretically, the incident P-wave upon layer 2 reaches the critical angle around 33° , which is equivalent to an offset of 530 m if the depth to layer 2 is 410 m. Before the critical distance, there is not much PSPPSP reflection energy in either of the graphs, Figure 3.1a or Figure 3.1b. Around the critical distance, all amplitude-versus-offset curves become complicated and no obvious relation can be observed between the PSPPSP reflection amplitude and the S-wave velocity of layer 2. Also, notice that there are differences in the curves between Figure 3.1a and Figure 3.1b around the critical distance. This is mainly due to phase changes in the events in the synthetic seismograms. In Figure 3.1a, the amplitudes are the absolute values from the solutions to the Zoeppritz equations, whereas in Figure 3.1b amplitude refers to the maximum positive amplitude picked from synthetic seismogram. Whenever there is a phase change, the maximum positive amplitude in Figure 3.1b and the absolute reflection coefficient value in Figure 3.1a may be different.

In both Figure 3.1a and Figure 3.1b, higher PSPPSP reflection amplitudes were obtained for offsets beyond the critical distance. The extreme case is that the best PSPPSP energy occurs when the S-wave velocity of layer 2 is 1477 m/s, which is close to the P-wave velocity in water. As the absolute difference between S-wave velocity in layer 2 and P-wave velocity in water becomes larger, PSPPSP reflection energy becomes smaller (Figure 3.1).

3.3 Dependence on the P-wave velocity in layer 2

Model 3-2 is very similar to model 3-1 except that the S-wave velocity in layer 2 was kept constant and P-wave velocity was varied as shown in Table 3.2.

Table 3.2 Physical parameters for layer 2, model 3-2

Case	V_p (m/s)	V_s (m/s)	Poisson's ratio σ	ρ (kg/m ³)
1	2220	1480	0.10	2000
2	2563	1480	0.25	2000
3	2877	1480	0.32	2000
4	4909	1480	0.45	2000

The S-wave velocity of layer 2 was set to be 1480 m/s, which is the same as the P-wave velocity in water. As shown previously, this provides maximum coupling between S-wave energy in layer 2 and P-wave energy in water. The objective of this model was to study the effect of the P-wave velocity in layer 2 on the PSPPSP reflection amplitude. P-wave velocities ranging from 2220 m/s to 4909 m/s were chosen. As for model 3-1, amplitudes of the PSPPSP event were calculated from the Zoeppritz equations and were also picked from synthetic seismograms generated for the models. These amplitudes are plotted versus offset in Figure 3.2a and Figure 3.2b, respectively. Critical angles for the four cases in Table 3.2 are 42°, 35°, 31°, 18°, corresponding to critical distances of 738 m, 574 m, 493 m and 266 m, respectively.

Before the critical distance, there is not much PSPPSP reflection energy. At about the critical distance, all amplitude-versus-offset curves become complicated. There are additional troughs in Figure 3.2b around the critical distance due to phase changes. As expected, an increase in the P-wave velocity of layer 2 results in a decrease in the critical distance. Beyond the critical distance, all amplitude curves overlay one another and it seems that, when the S-wave velocity of layer 2 is the same as the P-wave velocity in water, changing the P-wave velocity of layer 2 has little effect on the PSPPSP event amplitude.

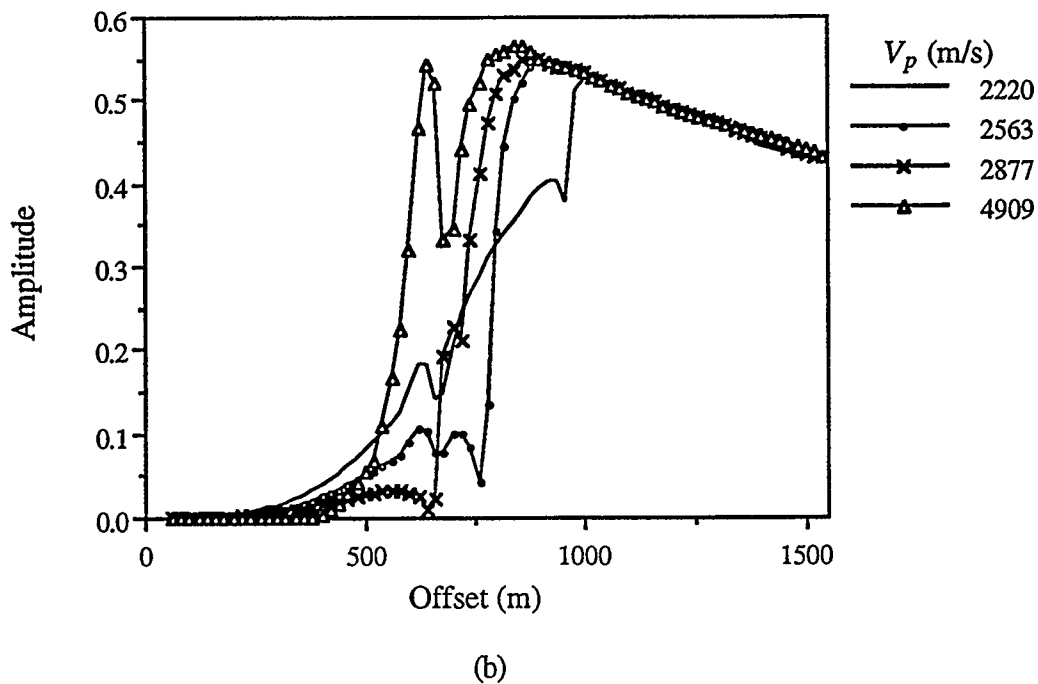
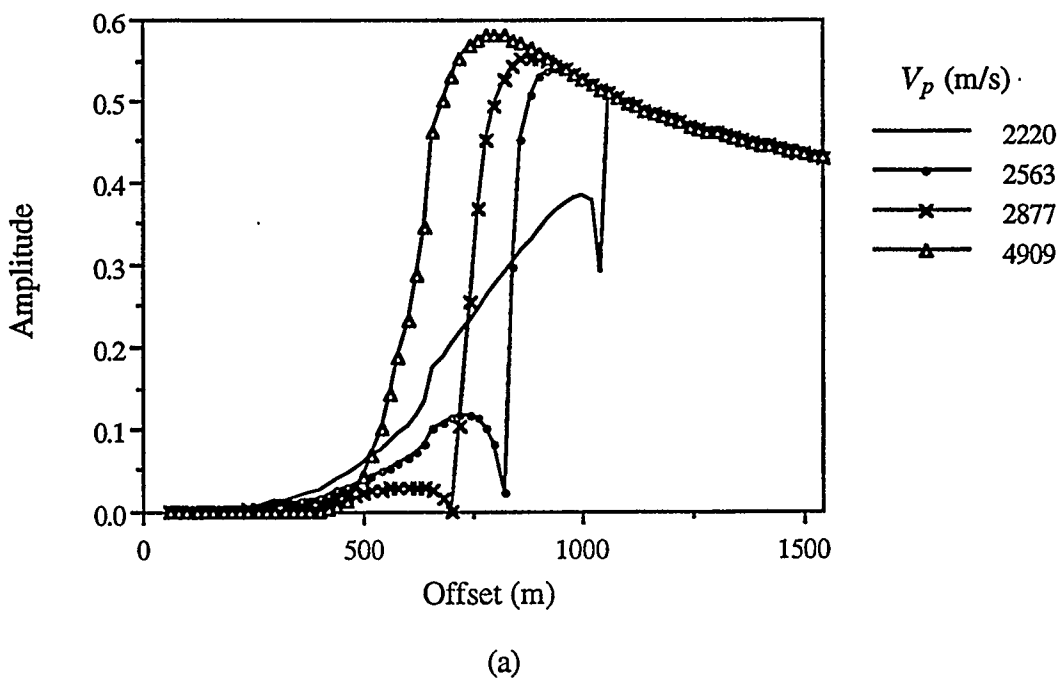


FIG. 3.2. Amplitude-versus-offset for model 3-2. Layer 2 has a constant S-wave velocity (1486 m/s), and a P-wave velocity varying from 2220 m/s to 4909 m/s. (a) Amplitude refers to the absolute value of the displacement reflection coefficient for PSPPPSP reflection calculated from Zoeppritz equations; (b) Amplitude is the maximum value picked from the synthetic seismogram.

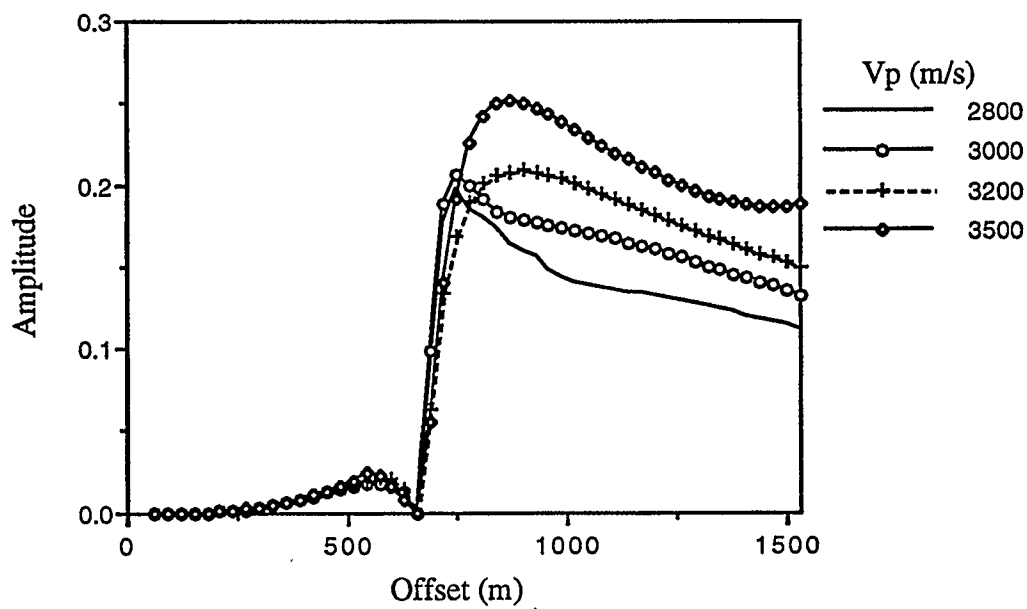
3.4 Dependence on the P-wave velocity in layer 4

The cross-sectional profile of model 3-3 is shown in Figure 2.1 as well. In model 3-3, layers 1 and 3 are water layers, and the P-wave and S-wave velocities of layer 2 are kept at 3000 m/s and 1500 m/s, respectively. As discussed above, the P-wave velocity of 3000 m/s is very similar to that of ice-bearing permafrost in the Canadian Beaufort Sea, and the V_P/V_S ratio of 2 ($\sigma = 0.33$) is a reasonable assumption for this lithology. Table 3.3 lists the physical parameters for layer 4.

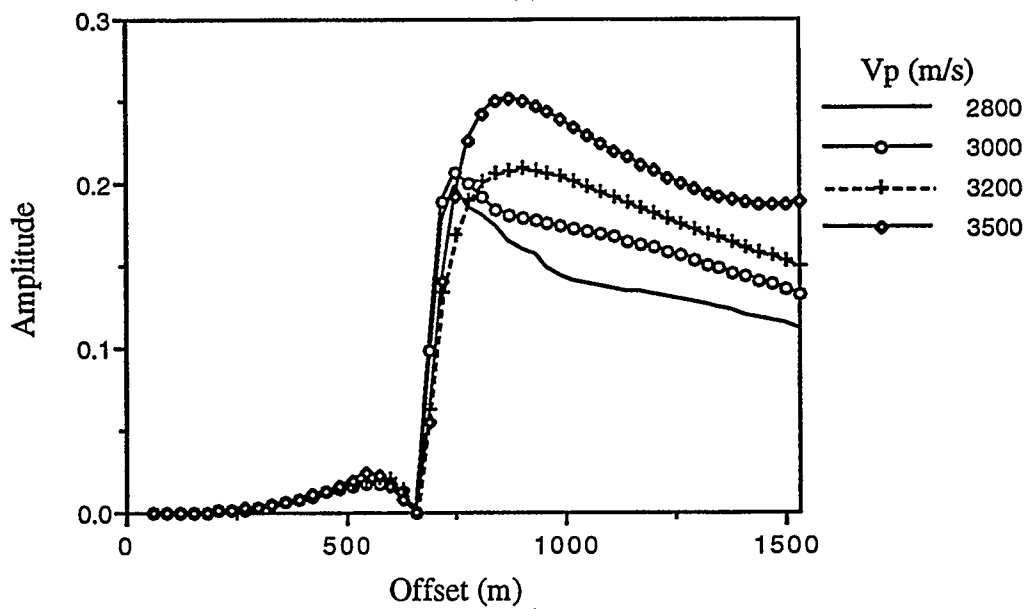
Table 3.3 Physical parameters for layer 4, model 3-3

Case	V_p (m/s)	V_s (m/s)	Poisson's ratio σ	ρ (kg/m ³)
1	2800	1400	0.33	2000
2	3000	1500	0.33	2000
3	3200	1600	0.33	2000
4	3500	1750	0.33	2000

A range of P-wave velocities ranging from 2800 m/s to 3500 m/s were chosen for layer 4. Amplitudes calculated from the Zoeppritz equations and picked from the appropriate synthetic seismograms are plotted versus offset in Figure 3.3a and Figure 3.3b, respectively. The incident P-wave reaches the critical angle at 30° at the top of layer 2, which is equivalent to the offset of about 600 m. Beyond the critical distance, increasing the P-wave velocity of layer 4 causes the PSPSP reflection amplitude to increase for the same offset.



(a)



(b)

FIG. 3.3. Amplitude-versus-offset for model 3-3. Layer 4 has a P-wave velocity varying from 2800 m/s to 3500 m/s, and a constant $V_P/V_S = 2$. The P-wave and S-wave velocities of layer 2 are 3000 m/s and 1500 m/s, respectively. (a) Amplitude refers to the absolute value of the displacement reflection coefficient for PSPPSP reflection calculated from Zoeppritz equations; (b) Amplitude is the maximum value picked from the synthetic seismogram.

3.5 Dependence on the thickness of layer 2

Model 3-4 was designed to investigate the effect of the thickness of layer 2 on the PSPPSP reflection. Previous studies (Poley and Lawton, 1991) showed that the thickness of the permafrost layers in the Canadian Beaufort Sea is not constant, and they suggested also that the thickness of *D6* (shallowest permafrost) should not have much effect on the reflection amplitude for the top of *D5* (second permafrost layer). This was tested in my study by setting different thicknesses for the *D6* permafrost layer (layer 2). Figure 3.4 shows the model and physical parameters of different model materials, in which the thickness of layer 2 changes from 5 m to 31 m (field units). When different thicknesses were chosen, the depth to the tops of layer 2 and layer 4 were kept constant (410 m and 580 m, respectively). The P-wave and S-wave velocities of layer 2 are 3000 m/s and 1700 m/s, respectively, which are close to those of Trabond, and similar to those of permafrost in the Canadian Beaufort Sea, as discussed previously. As in previous

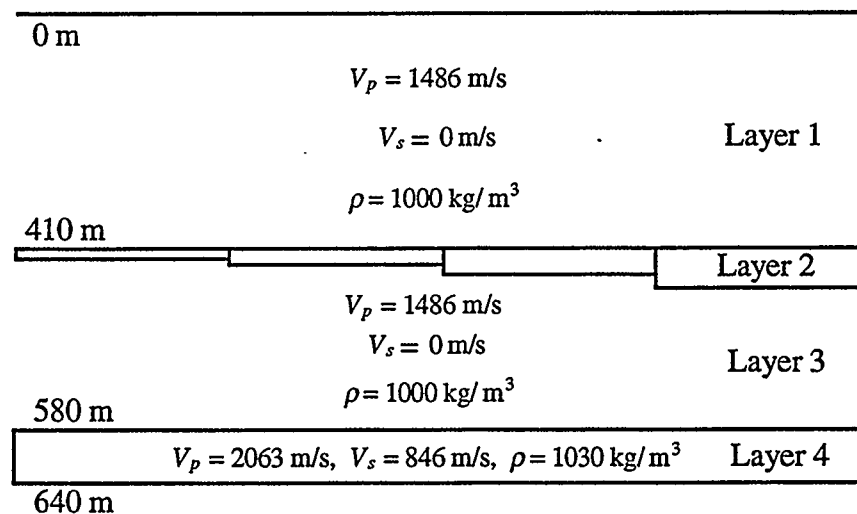
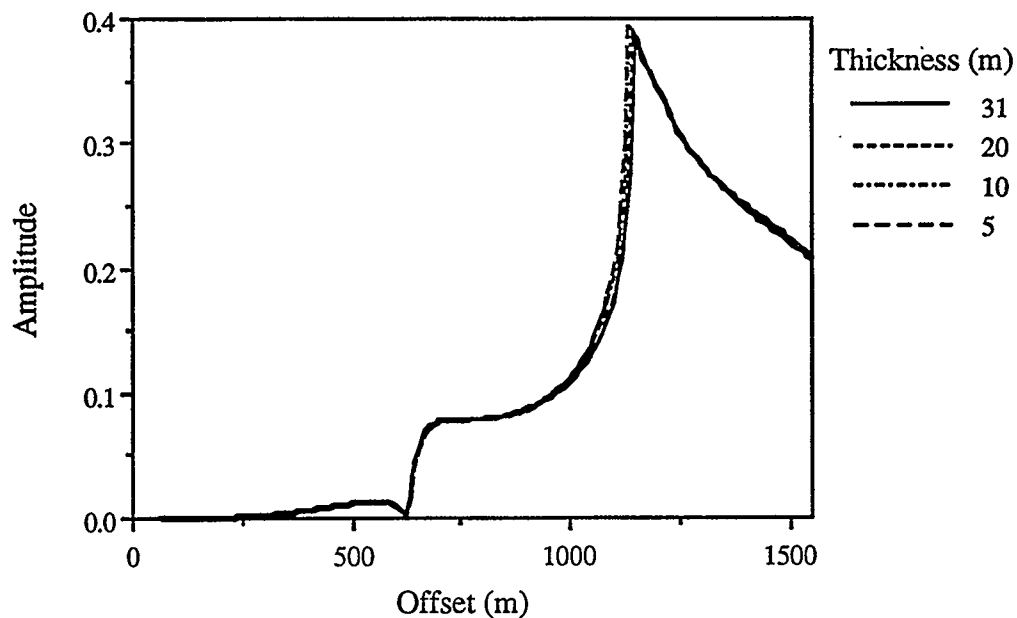
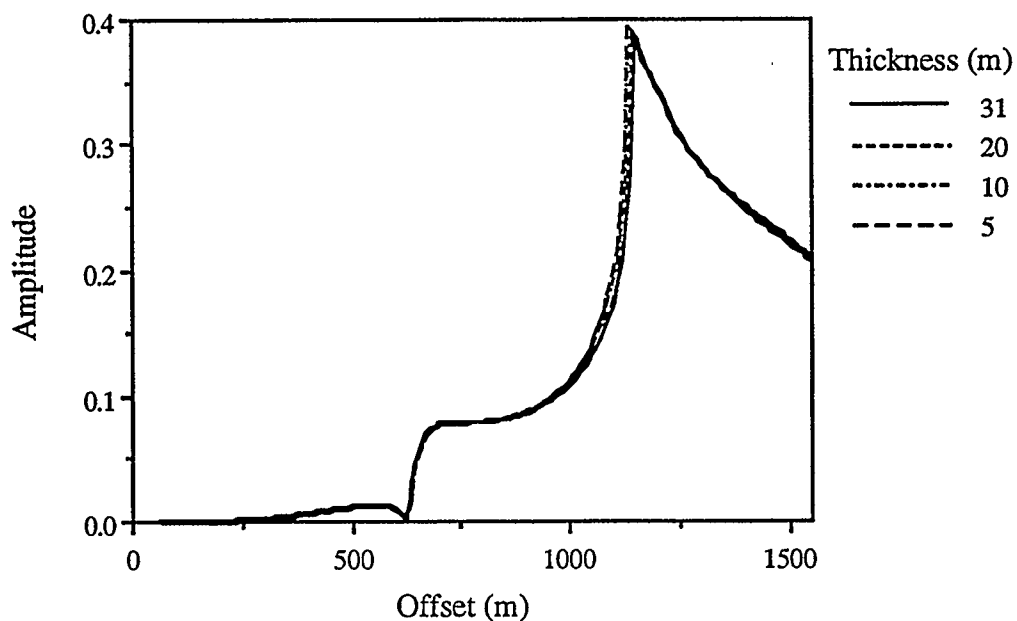


FIG. 3.4. Schematic diagram showing the model 3-4. The thicknesses of layer 2 are 5, 10, 20, and 31 m, respectively. Both layer 1 and layer 3 are water layers. P-wave velocity, S-wave velocity, and density for layer 2 are 3000 m/s, 1700 m/s, and 2100 kg/m³, respectively. V_p = P-wave velocity; V_s = S-wave velocity; ρ = density. Dimensions are given in field units.



(a)



(b)

FIG. 3.5 Reflection amplitude versus source-to-receiver offset for the P₁S₁P₁S₁P₁S₁P₁ event when with thickness of layer 2 varies from 5 m to 31 m. The P-wave and S-wave velocities of layer 2 are 3000 m/s and 1700 m/s, respectively. (a) Amplitude refers to the absolute value of the displacement reflection coefficient for P₁S₁P₁S₁P₁ reflection calculated from Zoeppritz equations; (b) Amplitude is the maximum value picked from the synthetic seismogram.

models, PSPPSP amplitudes calculated from the Zoeppritz equations and picked from synthetic seismograms were plotted versus offset in Figure 3.5a and Figure 3.5b, respectively. In both Figure 3.5a and Figure 3.5b, it is clear that PSPPSP reflection amplitudes become large beyond the critical distance, but the curves almost overlie one another, which suggests that the thickness of layer 2 does not affect the PSPPSP reflection energy significantly. This is partly due to the fact that attenuation was not included in the numerical modeling.

3.6 Dependence on the depth of layer 2

Model 3-5 was designed to study the effect of the depth of layer 2 on the PSPPSP event amplitude. Previous studies (Poley and Lawton, 1991) showed that the depth of permafrost in the Canadian Beaufort Sea varies from around 10 m to about 600 m. Figure 3.6 shows the physical parameters for different layers used in this model. The

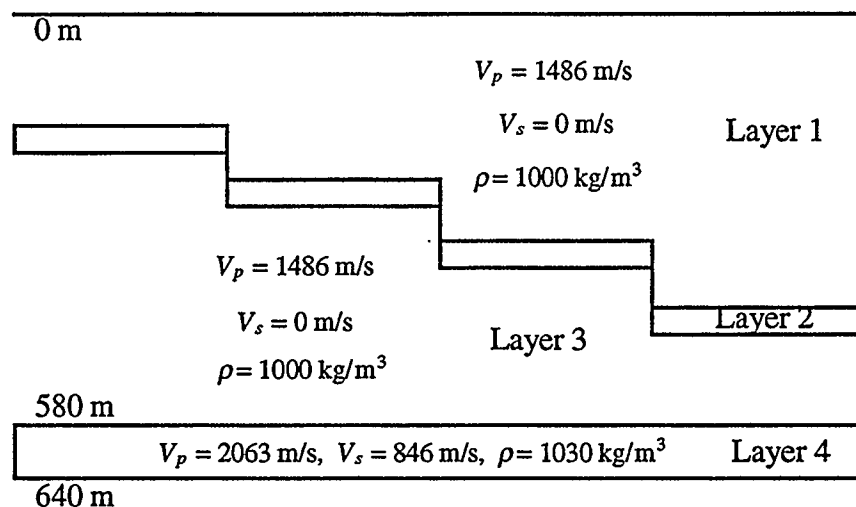
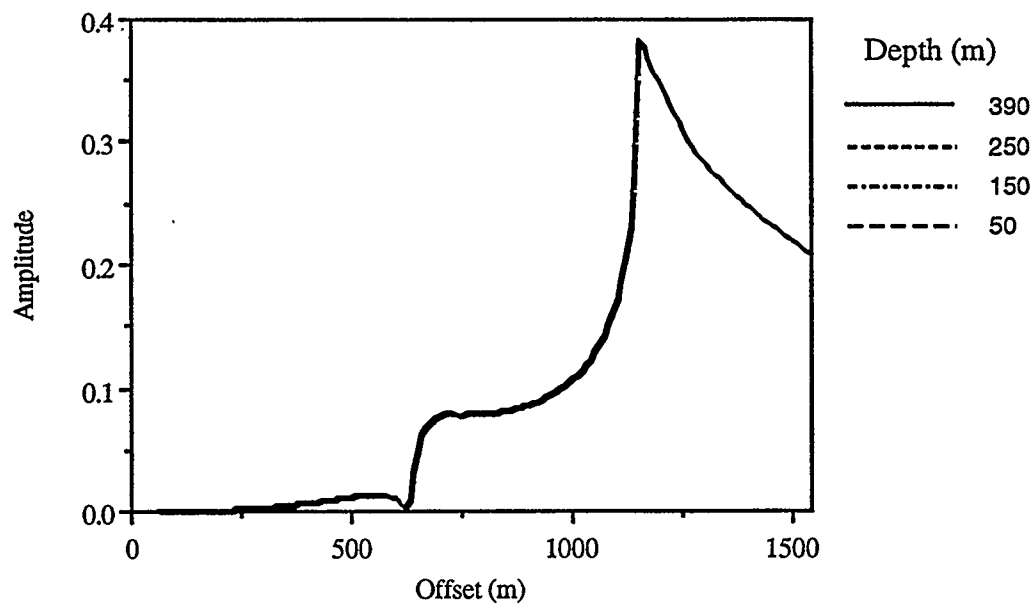


FIG. 3. 6. Schematic diagram of model 3-5. The depths to the top of layer 2 from left to right are 50, 150, 250, and 390 m, respectively. Both layer 1 and layer 3 are water layers. P-wave velocity, S-wave velocity, and density for layer 2 are 3000 m/s, 1700 m/s, and 2100 kg/m³, respectively. The thickness of layer 2 is 31 m. V_p = P-wave velocity; V_s = S-wave velocity; ρ = density. Dimensions are given in field units.

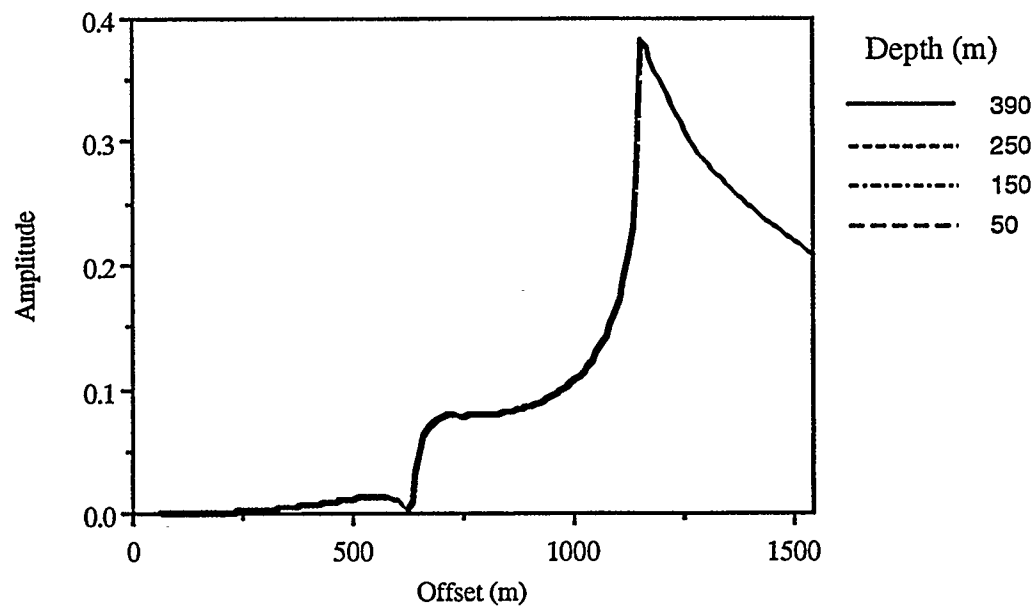
thickness of layer 2 was kept constant (31 m) for different depths. As for previous models, PSPPSP event amplitudes, calculated from the Zoeppritz equations and picked from synthetic seismograms are plotted versus offset in Figure 3.7a and Figure 3.7b, respectively. From Figure 3.7, as it is expected, it is clear that depth of layer 2 does not affect PSPPSP reflection energy.

3.7 Discussion

The numerical modeling results suggest that the S-wave velocity of layer 2 and the P-wave velocity of layer 4 contribute most significantly to the amplitude of multiconverted PSPPSP reflection of the models tested. This verifies the physical modeling results from chapter 2. Also, through numerical modeling, it has been shown that the P-wave velocity of layer 2 does not affect the PSPPSP event amplitude very much, but will affect the offset range over which this event is observed. Based on the assumption of zero attenuation for all layers, the thickness and the depth of layer 2 do not contribute significantly to the amplitude of the PSPPSP reflection.



(a)



(b)

FIG. 3.7. Amplitude-versus-offset for model 3-5. The P-wave and S-wave velocities of layer 2 are 3000 m/s and 1700 m/s, respectively. (a) Amplitude refers to the absolute value of the displacement reflection coefficient for PSPSP reflection calculated from Zoeppritz equations; (b) Amplitude is the maximum value picked from the synthetic seismogram.

Chapter 4: Multifold physical modeling data

4.1 Introduction

None of the models described in chapter 2 has any lateral velocity change in layer 2. In order to evaluate multiconverted reflections over a more complex velocity structure, a model with a lateral velocity change for layer 2 was constructed. Figure 4.1 shows a schematic diagram of this model. It is similar to models described in chapters 2 and 3, except layer 2 is made of 5 different materials as a function of distance along the model. Layers 1 and 3 are water layers, and layer 4 was composed of aluminum. In Figure 4.1, five different materials were chosen for layer 2, namely Plexiglas, polystyrene, Trabond, PVC Foam and aluminum. The physical properties of these materials are listed in Table 4.1. These five surface layers were suspended in water above the aluminum basal layer as shown schematically in Figure 4.1. The model was put on a Plexiglas table in the water-filled seismic modeling tank.

Table 4.1. Materials and their physical parameters , Model 4-1

Compound	Thickness (actual, cm)	Thickness (scaled, m)	V_p (m/s)	V_s (m/s)	σ	ρ (kg/m ³)
Aluminum	0.62	31	6004	3029	0.33	2640
Trabond	0.62	31	3010	1733	0.25	1210
Plexiglas	0.62	31	2740	1385	0.33	1200
Polystyrene	0.62	31	2063	846	0.40	1030
Water			1486	0	0.50	1000
PVC Foam	0.62	31	1100	740	0.10	670
Orthodic Foam	0.62	31	1069	591	0.28	160

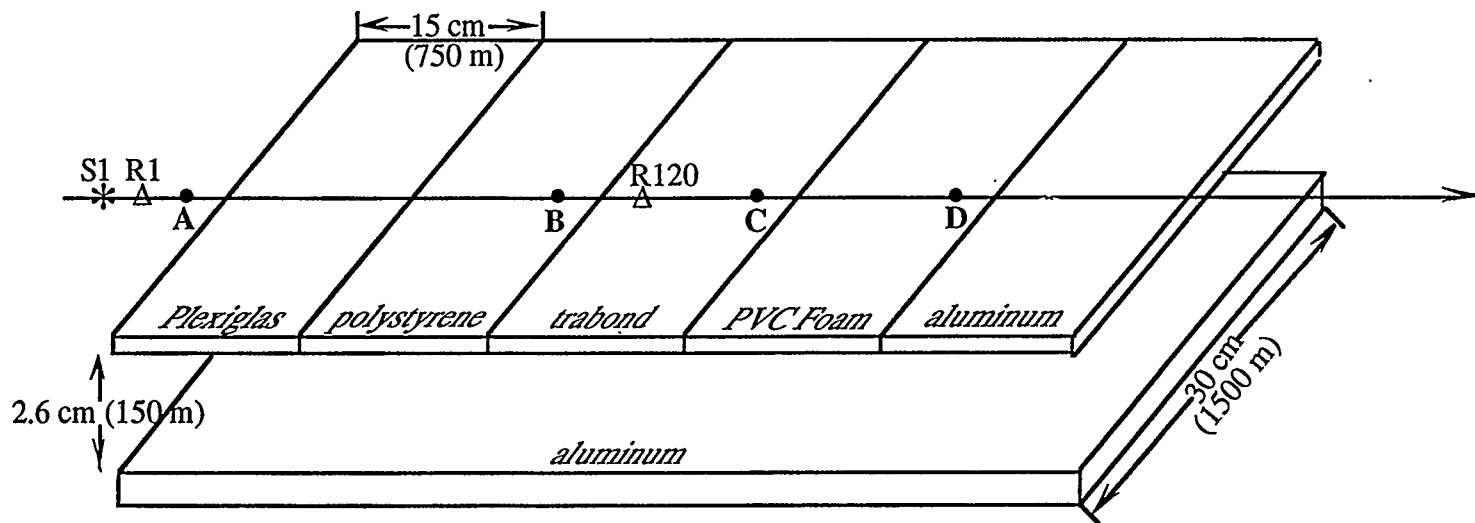


FIG. 4.1. Schematic diagram of the model with lateral velocity change; the model units are shown in centimeter and the world units are shown in meter in brackets. The model was suspended above the aluminum basal layer in water. *S1* = the first shot location; *S120* = the 120th shot location; *R1* = the first trace location for the first shot; *R120* = the 120th trace for the first shot. *A*, *B*, *C*, *D* = four shot gather locations shown in Figure 4.2 to Figure 4.5. The arrow shows the direction for the seismic survey.

4.2 Data acquisition

One seismic survey was run along the line over the model as shown in Figure 4.1, and the geometry used for the survey is given in Table 4.2. Figure 4.1 shows the locations for the first (S1) and the last (S120) shots, as well as the first (R1) and the last (R120) trace locations for the first shot (S1). Four shot locations in Figure 4.1, namely *A*, *B*, *C* and *D* were chosen to illustrate the raw data. The shot gathers for these four locations are shown in Figure 4.2a, Figure 4.3a, Figure 4.4a and Figure 4.5a, respectively. All of these displays are true amplitude plots without any scaling applied.

4.3 Data processing

The data were processed using Landmark/ITA software on the Sun Workstation cluster at the University of Calgary. Table 4.3 lists the data processing procedure.

Table 4.2. Geometry for data acquisition over Model 4-1 (field units)

	Model Unit	Field unit
Number of shots:	120	120
Traces/shot:	120	120
Near offset:	1.6 (cm)	80 (m)
Far offset:	39.68 (cm)	1984(m)
Group interval:	0.32 (cm)	16 (m)
Shot interval:	0.64 (m)	32 (m)
Maximum fold:	30	30
Central frequency (Hz.):	250 (kHz)	50 (Hz)
Samples:	4096	4096
Sample rate:	100 (ns)	0.5 (ms)

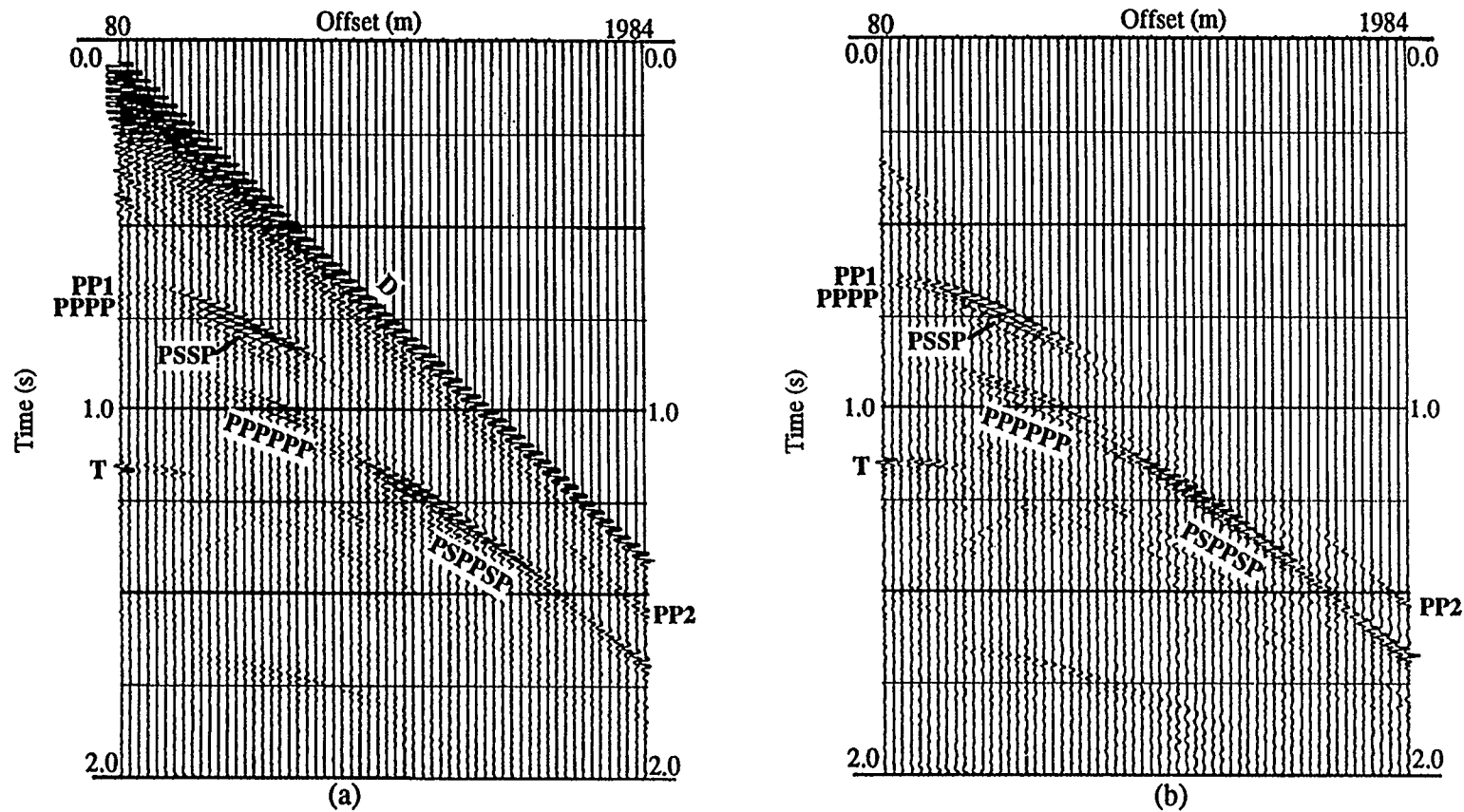


FIG. 4.2. (a) Shot gather on location "A" in Figure 4.1. (b) The same shot gather as in (a), but with mute, deconvolution and bandpass filter applied; D = direct arrival; PP1 = P-wave reflection from the top of Plexiglas; PP2 = P-wave reflection from the top of polystyrene; T = P-wave reflection from the top of Plexiglas table; PPSPP = P-wave reflection from the bottom of Plexiglas; PSSP = multiconverted reflection from the bottom of Plexiglas; PPSPPPP = P-wave reflection from the top of aluminum; PSPPSP = multiconverted reflection from the top of aluminum.

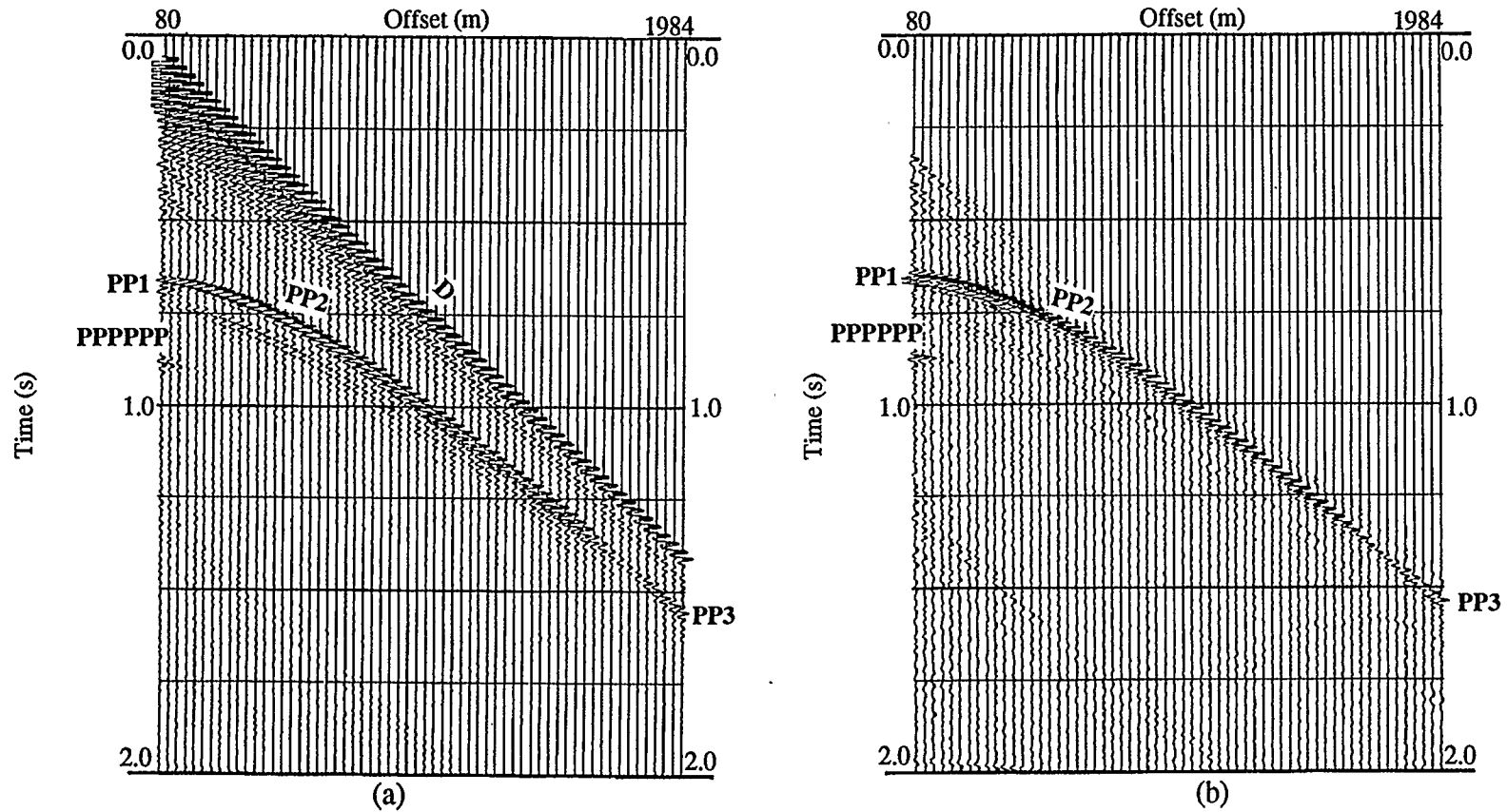


FIG. 4.4. (a) Shot gather on location *C* in Figure 4.1. (b) The same shot gather as in (a), but with mute, deconvolution and bandpass filter applied; D = direct arrival; PP1 = P-wave reflection from the top of Trabond; PP2 = P-wave reflection from the top of PVC Foam; PP3 = P-wave reflection from the top of aluminum; PPPPPP = P-wave reflection from the top of aluminum through Trabond.

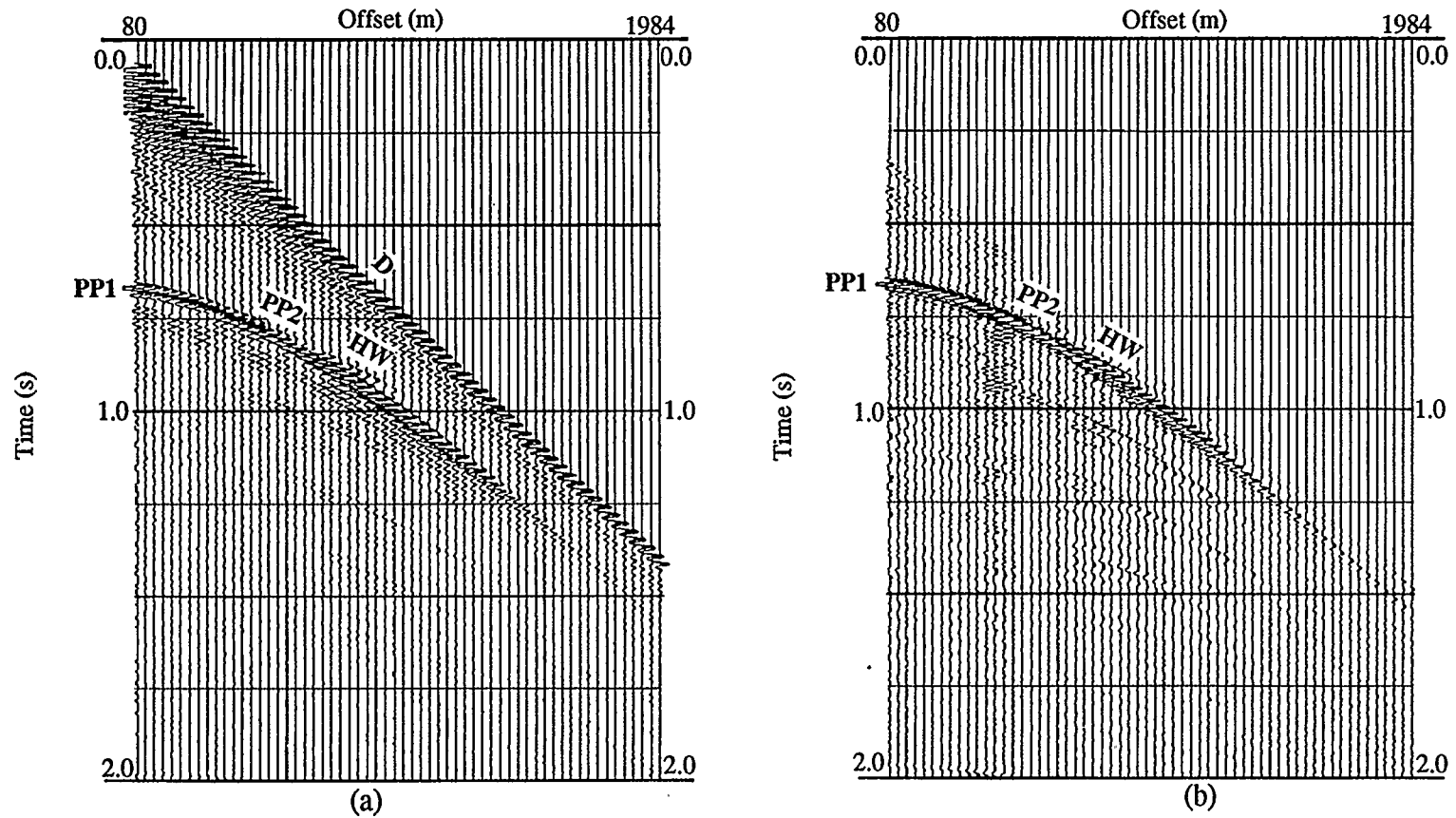
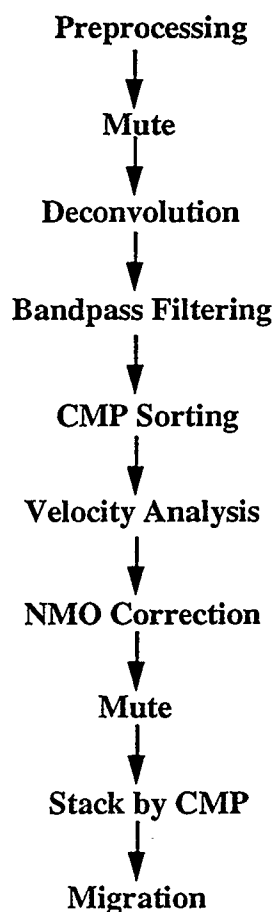


FIG. 4.5. (a) Shot gather on location *D* in Figure 4.1. (b) The same shot gather as in (a), but with mute, deconvolution and bandpass filter applied; D = direct arrival; PP1 = P-wave reflection from the top of PVC Foam; PP2 = P-wave reflection from the top of aluminum; HW = shear head-wave (PSP) from the top of aluminum.

4.3.1 Preprocessing

Since the data were recorded in trace-sequential format, preprocessing involved only inputting the field geometry (Table 4.3) and editing any bad traces.

Table 4.3 Seismic processing flow for the physical modeling data



4.3.2 Mute, deconvolution and bandpass

In Figure 4.2a, the strong direct arrival (marked *D*) is identified. PP1 refers to the P-P reflection from the top of Plexiglas (layer 2); PP2 refers to the P-P reflection from the top of adjacent polystyrene (layer 2); and *T* refers to the P-P reflection from the top of the underlying Plexiglas table. PPPP refers to the P-wave reflection from the base of the

Plexiglas, and PSSP is the multiconverted reflection from the base of the Plexiglas. PPPPPP is the P-wave reflection from the top of the aluminum basal layer (layer 4), through the Plexiglas layer (see Figure 1.1 for PPPPPP definition). PSPPSP refers to the multiconverted reflection from the top of the aluminum basal layer (layer 4), through the Plexiglas layer (also see Figure 1.1 for PSPPSP definition).

A mute was applied before deconvolution to eliminate the strong direct arrival. A seismic trace can be considered as the convolution of a spike sequence (seismic reflectivities) with a seismic wavelet. Ideally, the application of deconvolution results in a spike sequence (seismic reflectivities) from the seismic traces. In practice, deconvolution is used for data processing to improve the seismic resolution by compressing the seismic wavelet. A standard spiking deconvolution with a wavelet estimation time window of 80 ms was applied to the data. A bandpass filter with the frequency pass band from 10 to 70 Hz. was also applied to the data. Figures 4.2b is the same shot gather as shown in Figure 4.2a, but with mute, deconvolution and bandpass filtering applied to the data.

The shot gather for location *B* is shown in Figure 4.3a, and Figure 4.3b is the same shot gather after application of mute, deconvolution and bandpass filtering. In both figures, PP1 refers to the P-P reflection from the top of polystyrene (layer 2), PP2 refers to the P-P reflection from the top of the adjacent Trabond (layer 2), and PP3 refers to the P-P reflection from the top of PVC Foam (layer 2). PPPP is the P-wave reflection from the base of polystyrene. PPPPPP1 refers to the P-wave reflection from the top of the basal aluminum layer (layer 4), through the polystyrene layer, and PPPPPP2 is the P-wave reflection from the top of the basal aluminum layer (layer 4), through the Trabond layer. PSPPSP refers to the multiconverted reflection from the top of the aluminum basal layer (layer 4), through the Trabond layer. Comparing the PSPPSP amplitude in Figure 4.2a with that in Figure 4.3a, we can see higher PSPPSP amplitude in Figure 4.2a. As

discussed previously, this is due to the fact that the S-wave velocity of Plexiglas (Figure 4.2a) is closer to the P-wave velocity of water than that of Trabond.

The comparable shot gathers for location *C* are shown in Figure 4.4. In these records, PP1 refers to the P-P reflection from the top of Trabond (layer 2); PP2 refers to the P-P reflection from the top of PVC Foam (layer 2), and PP3 refers to the P-P reflection from the top of aluminum (layer 2). PPPPPP is the P-wave reflection from the top of the basal aluminum layer (layer 4), through the Trabond layer. The raw and partly processed shot gathers for location *D* are shown in Figure 4.5. PP1 refers to the P-P reflection from the top of PVC Foam (layer 2), PP2 refers to the P-P reflection from the top of aluminum (layer 2). *HW* in Figure 4.5 is interpreted to be a head wave. The calculated apparent velocity for this head wave is around 3080 m/s, which is about the same as the S-wave velocity of aluminum (3029 m/s). Therefore, this head wave is a converted head wave (PSP). As discussed in chapter 2, the incident P-wave reaches the critical angle at 29° at the top of aluminum, it is then converted to an S-wave. The converted S-wave travels along the surface of aluminum, then is converted back to P-wave to create a PSP head wave raypath.

4.3.3 CMP sorting, velocity analysis, NMO correction and mute

The traces in the collection of shot records were sorted into common midpoint (CMP) gathers, and velocity analysis was performed on these gathers based on semblance. If the correct velocity is used for correcting normal moveout (NMO) then reflections are horizontally corrected in the CMP domain. Figure 4.6 to Figure 4.10 are five NMO-corrected CMP gathers. These five CMP gathers are over Plexiglas (CMP 101), polystyrene (CMP 194), Trabond (CMP 287), PVC Foam (CMP 380) and over aluminum (CMP 504), respectively. Table 4.4 shows a comparison between rms velocities calculated for CMP 101 during processing and true rms velocities calculated from the known model velocities.

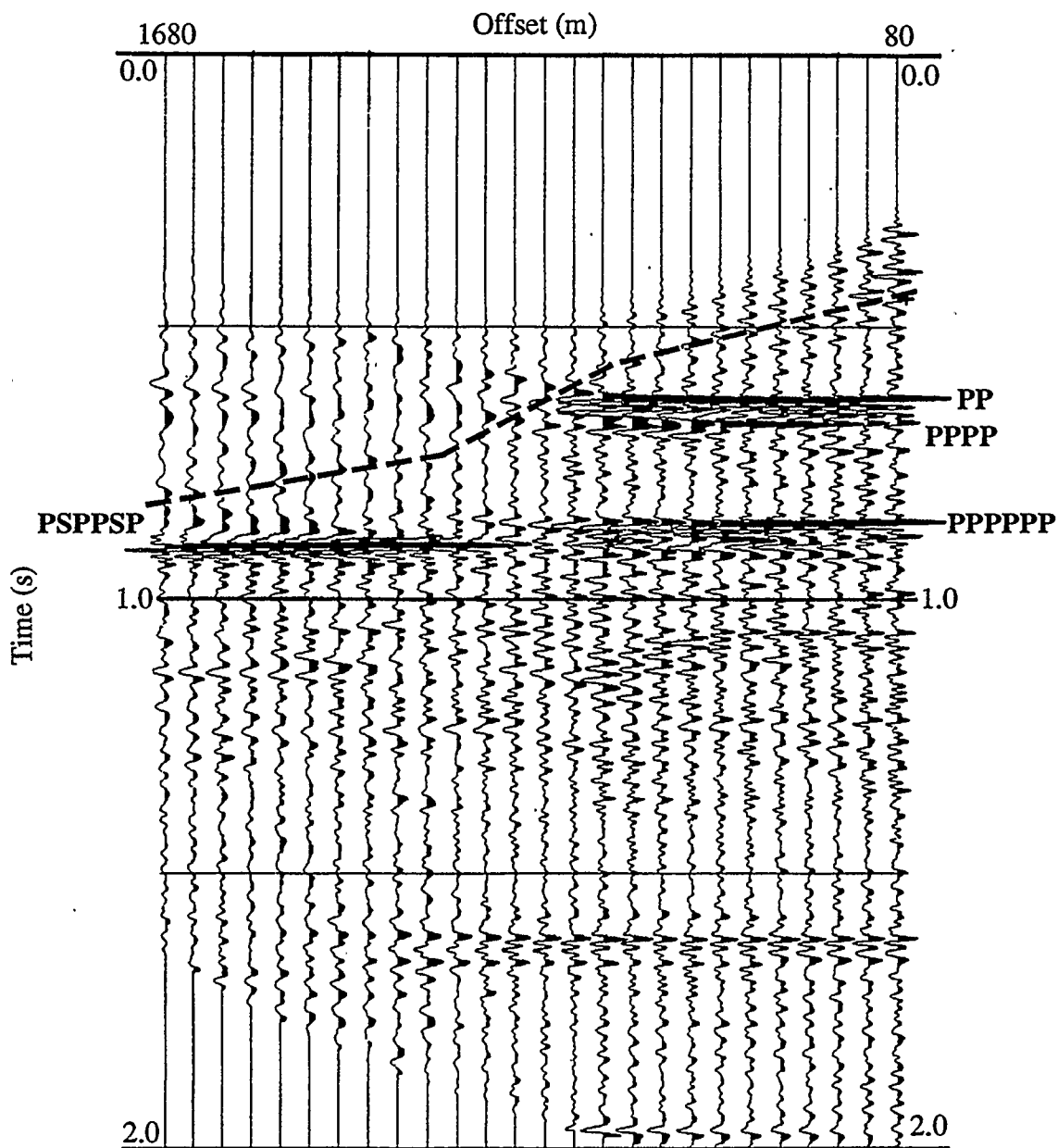


FIG. 4.6. NMO-corrected gather for CMP 101 (over Plexiglas). PP = P-wave reflection from the top of Plexiglas; PPPP = P-wave reflection from the bottom of Plexiglas; PPPPPP = P-wave reflection from the top of aluminum; PSPPSP = multiconverted reflection from the top of aluminum. The mute pattern is shown as a dashed line.

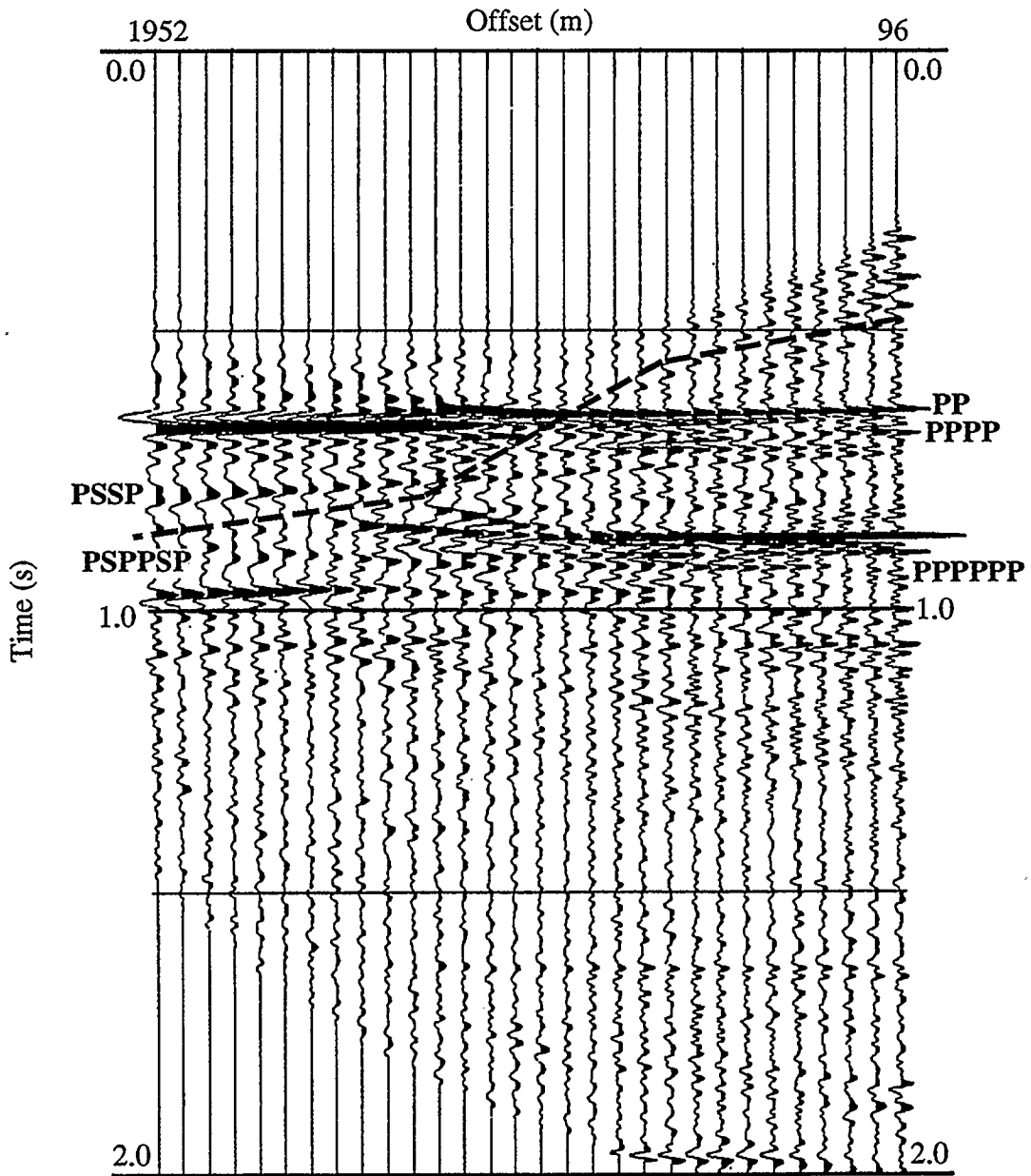


FIG. 4.7. NMO-corrected gather for CMP 194 (over polystyrene). PP = P-wave reflection from the top of polystyrene; PPPP = P-wave reflection from the bottom of polystyrene; PSSP = multiconverted reflection from the bottom of polystyrene; PPSPP = multiconverted reflection from the top of aluminum; PPSPP = P-wave reflection from the top of aluminum. The mute pattern is shown as a dashed line.

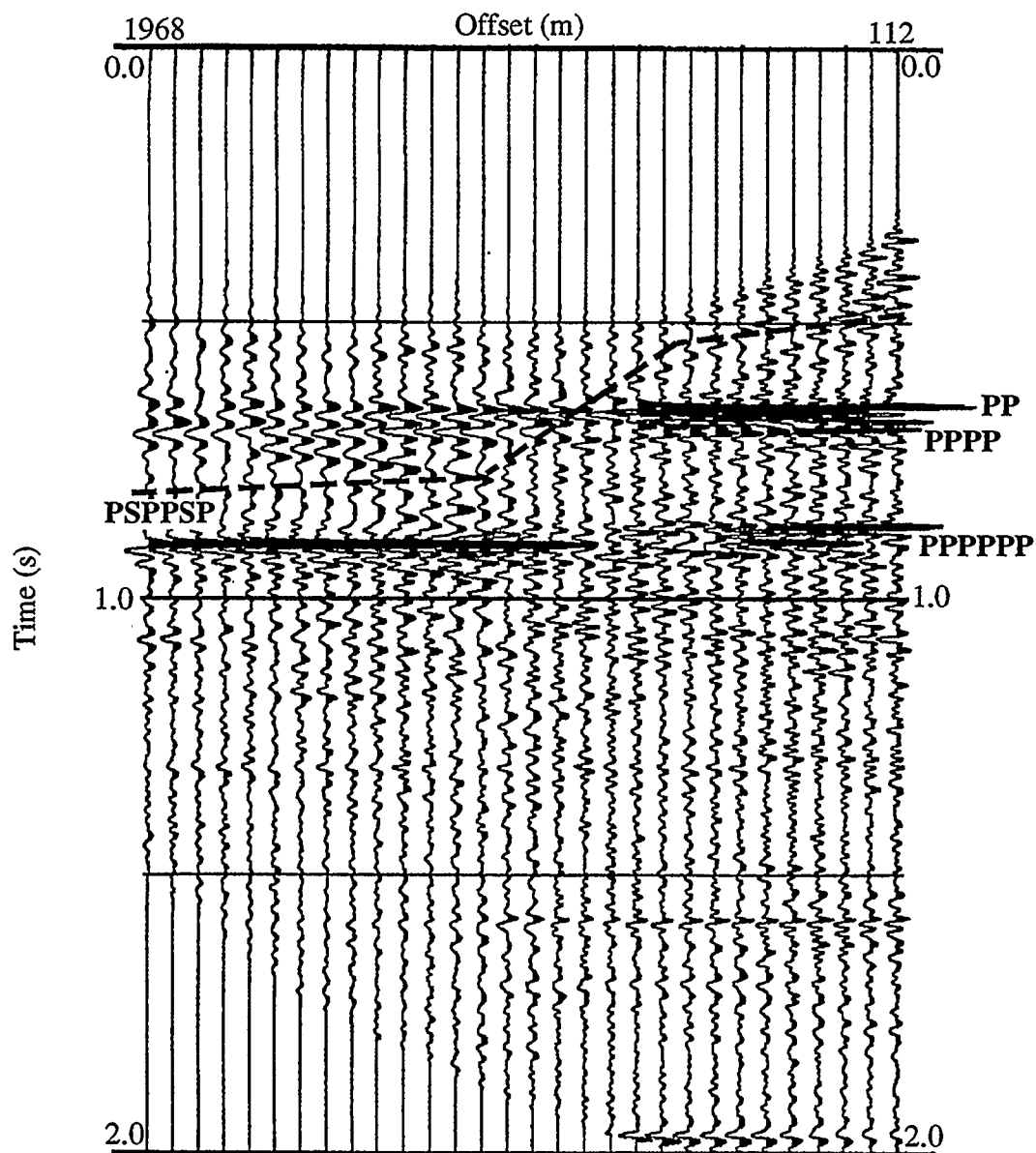


FIG. 4.8. NMO-corrected gather for CMP 287 (over Trabond). PP = P-wave reflection from the top of Trabond; PPPP = P-wave reflection from the bottom of Trabond; PPPPPP = P-wave reflection from the top of aluminum; PSPPSP = multiconverted reflection from the top of aluminum. The mute pattern is shown as a dashed line.

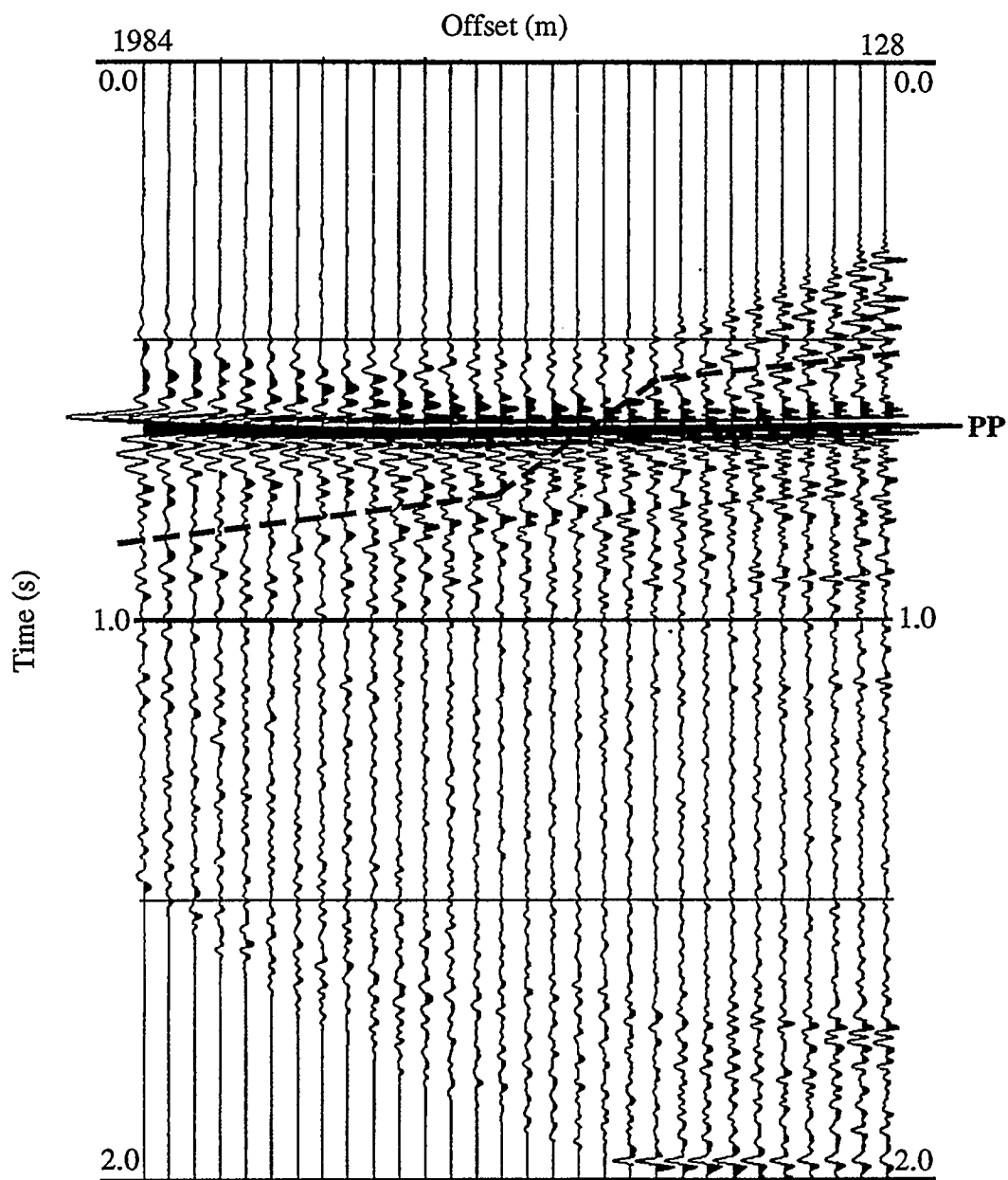


FIG. 4.9. NMO-corrected gather for CMP 380 (over PVC Foam). PP = P-wave reflection from the top of PVC Foam. The mute pattern is shown as a dashed line.

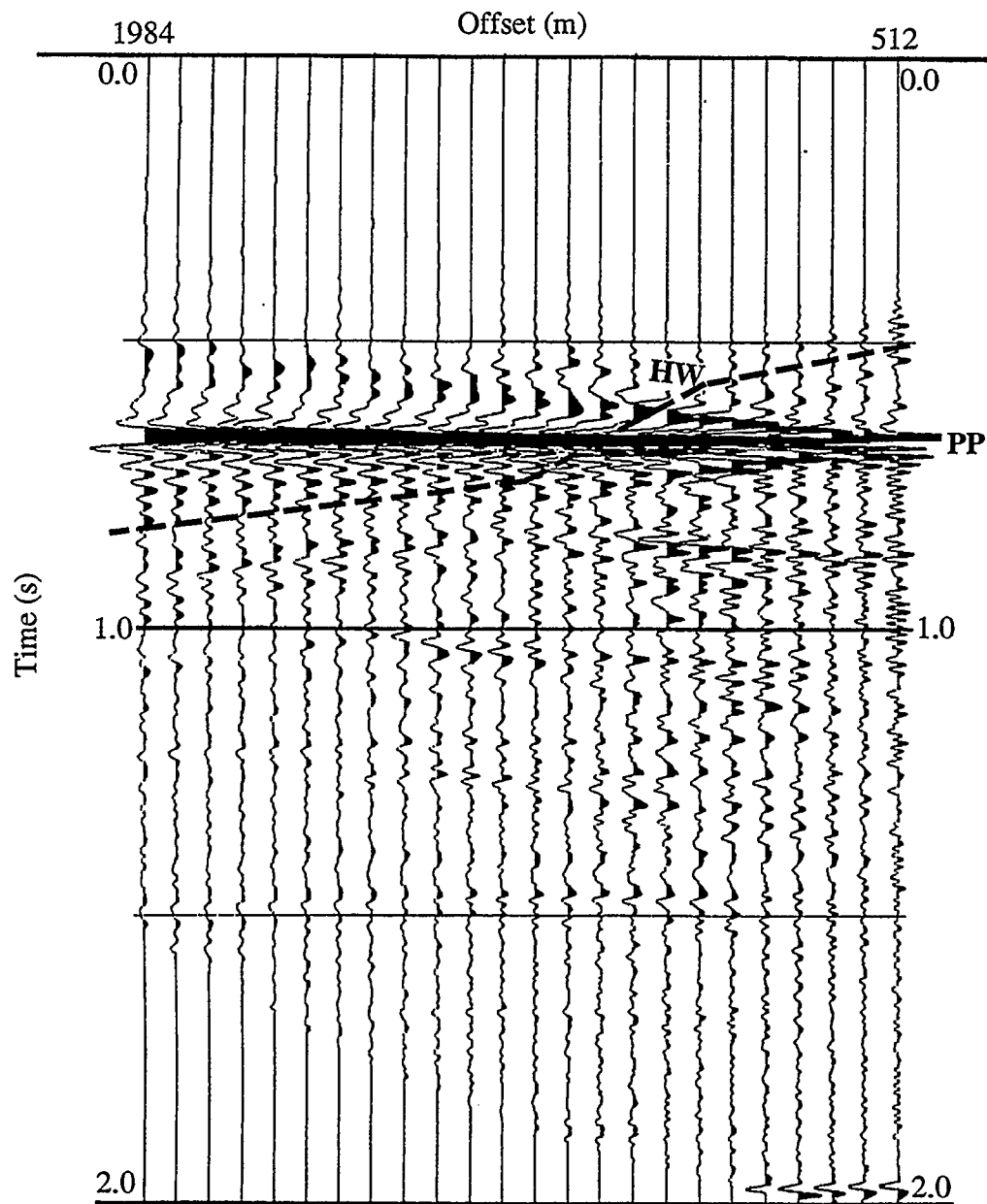


FIG. 4.10. NMO-corrected gather for CMP 504 (over aluminum). PP = P-wave reflection from the top of aluminum. HW = shear head-wave (PSP) from the top of aluminum. The mute pattern is shown as a dashed line.

Table 4.4 RMS velocities for CMP 101

Time (ms)	Stacking Velocity (m/s)	Known Velocity (m/s)
0	1450	1486
627	1450	1486
650	1515	1548
852	1502	1533
872	1750	1768
1100	1689	1713

For these CMP gathers, PP refers to the P-wave reflection from the top of layer 2 (Plexiglas, polystyrene, Trabond, PVC Foam and aluminum), PPPP is the P-wave reflection from the base of layer 2 and PSSP refers to the multiconverted reflection from the base of layer 2. PPPPPP refers to the P-wave reflection from the top of layer 4 (aluminum basal layer), and PSPPSP is the multiconverted reflection from the top of layer 4.

As discussed by Yilmaz (1987), after the NMO correction, a frequency distortion occurs, especially for the shallow events at the far offset. This is called the NMO stretch. Because of the NMO stretch, stacking the NMO-corrected CMP gathers will severely damage the shallow events (Yilmaz, 1987). Hence, a mute was again applied after the NMO correction and before stacking the data. The mute patterns are shown in dashed lines from Figure 4.6 to Figure 4.10.

4.3.4 Stack

Stacking (i.e. summing) in the CMP domain is done mainly to enhance the signal-to-noise ratio. In the CMP domain, all traces for one CMP are summed together to get one single output trace. Figure 4.11 shows the stacked section of the processed physical

modeling dataset for the model shown in Figure 4.1. Five CMP locations (shown in Figures 4.6 to 4.10) are marked on the stacked section. In Figure 4.11, PP refers to the P-wave reflection from the top of layer 2 (Plexiglas, polystyrene, Trabond, PVC Foam, and aluminum). Notice that the top of layer 2 for all cases was well imaged. PPPP is the P-wave reflection from the bottom of layer 2, and PSSP is the multiconverted reflection from the base of layer 2. PPPPPP refers to the P-wave reflection from the top of layer 4 (aluminum basal layer). The acoustic-impedance difference between both PVC Foam or aluminum and water is large, and hence most energy was reflected back from the top of PVC Foam and aluminum and later events have very low amplitudes.

In Figure 4.11, T is the P-P reflection from the top of the Plexiglas table, and PSPPSP is the multiconverted reflection from the top of layer 4. Notice that the PSPPSP reflection has much higher amplitude when Plexiglas and Trabond are used as layer 2 than for the other cases. As discussed in chapter 2, this is due to the fact that the S-wave velocities in Plexiglas and Trabond are closer to the P-wave velocity in water than those of other materials.

Offset-limited stacked sections (Figure 4.12 and Figure 4.13) were also created from the physical modeling dataset. Figure 4.12 is the near-offset (0 to 800 m) stacked section, with PP, PPPP, and PPPPPP events imaged well, since these reflections occur mostly at the near offsets. Figure 4.13 is the far offset (800 m to 1984 m) stacked section, with only PSPPSP reflections well imaged, since PSPPSP reflections dominate the far offset traces on CMP gathers (Figures 4.6 and 4.8).

4.3.5 Migration

Migration moves dipping reflectors into their true subsurface positions and collapses diffractions (Yilmaz, 1987). In Figure 4.11, the diffraction energy along the edges of layer 2 can be observed. A phase-shift migration was undertaken after stacking

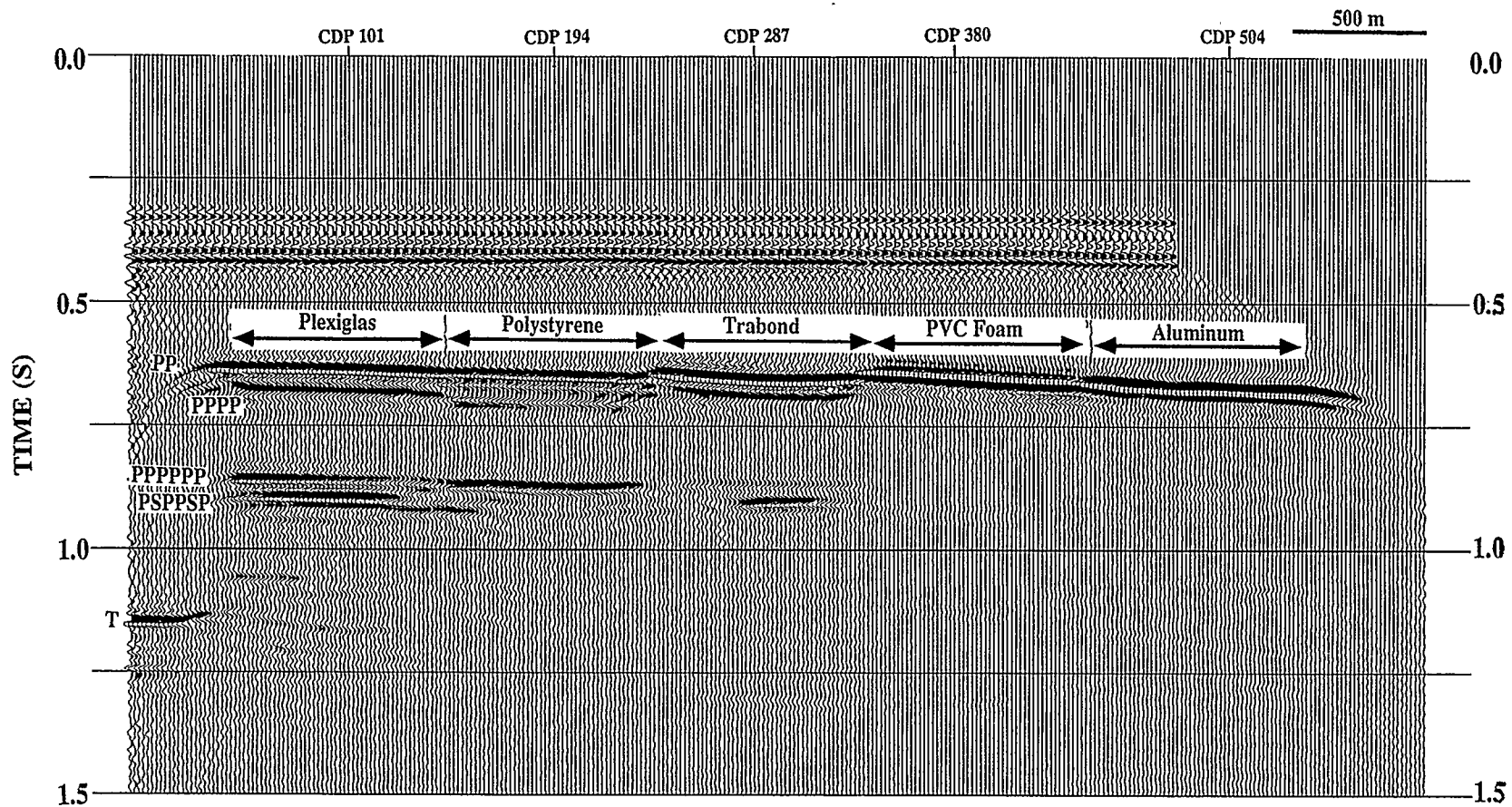


FIG. 4.11. Final stacked section for the physical modeling data. Five CMP locations (shown from Figure 4.6 to Figure 4.10) are marked. PP = P-wave reflection from the top of layer 2 (Plexiglas, polystyrene, Trabond, PVC Foam and aluminum); PPPP = P-wave reflection from the base of layer 2; PPPPPP = P-wave reflection from the top of layer 4 (aluminum); PSPPSP = multiconverted reflections from the top of layer 4; T = P-wave reflection from the top of the Plexiglas table.

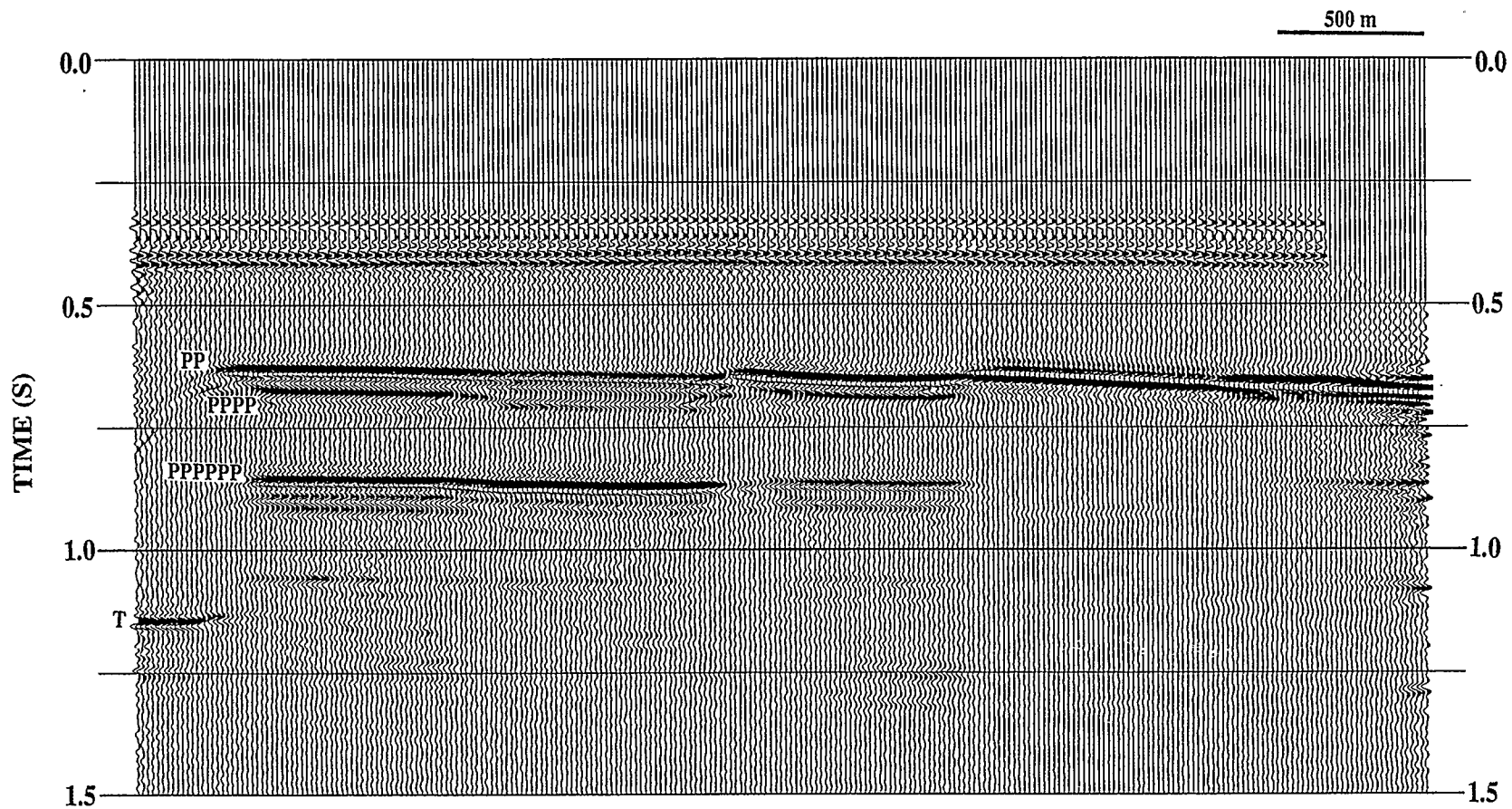


FIG. 4.12. The near-offset (0 to 800 m) stacked section for the physical modeling data. PP = P-wave reflection from the top of layer 2 (Plexiglas, polystyrene, Trabond, PVC Foam and aluminum); PPPP = P-wave reflection from the base of layer 2; PPPPPP = P-wave reflection from the top of layer 4 (aluminum); T = P-wave reflection from the top of the Plexiglas table.

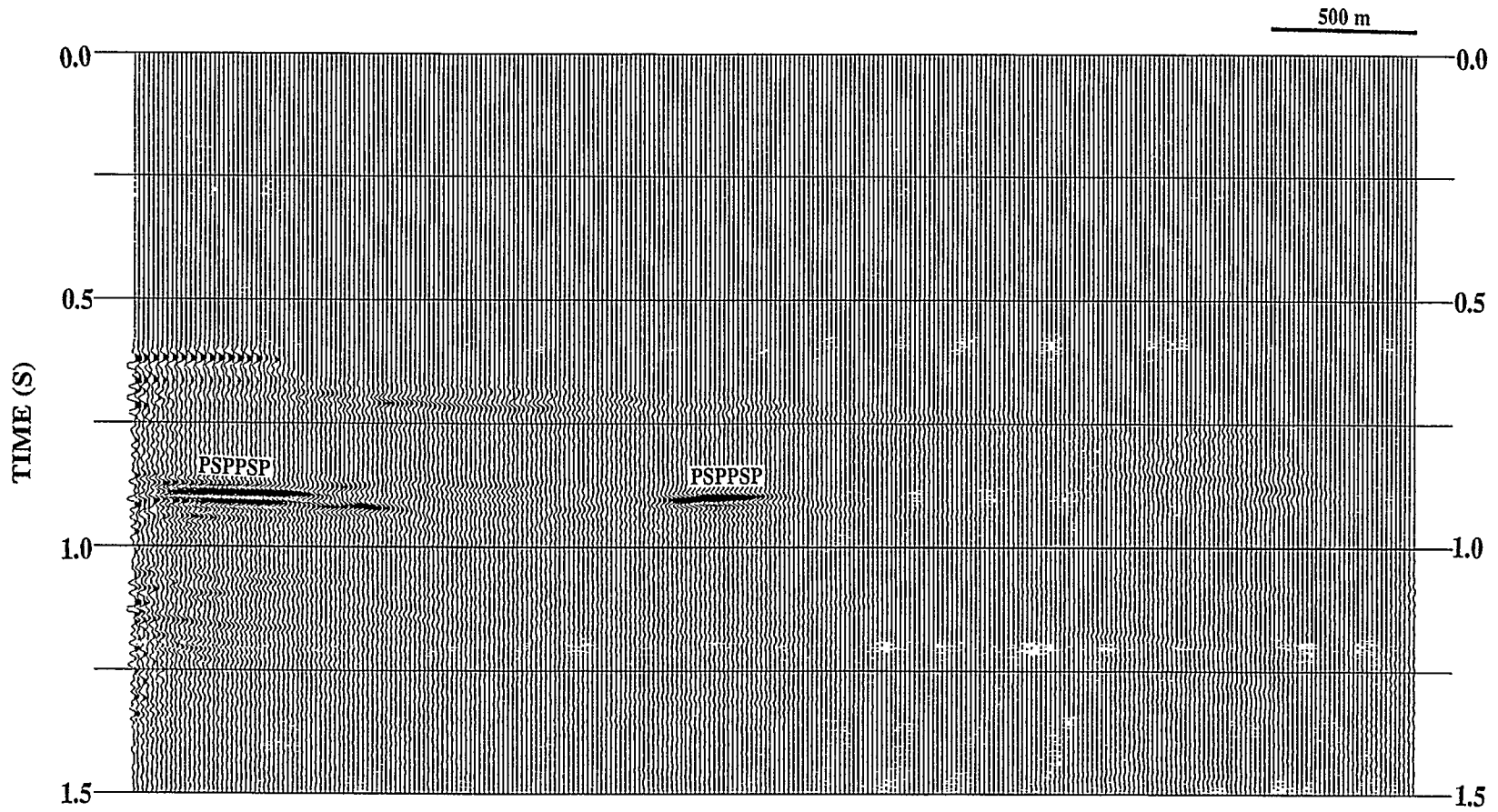


FIG. 4.13. The far offset (800 m to 1984 m) stacked section for the physical modeling data. PSPPSP = multiconverted reflections from the top of layer 4 (aluminum).

the data in order to collapse the diffraction energy. Figure 4.14 shows the final migrated section obtained from the physical modeling data.

4.4 Discussion

In this chapter, the top of layer 2 of the physical model was well imaged for all cases when using the standard processing procedures. Reflectors deeper than the base of layer 2 were well imaged only when Plexiglas, polystyrene or Trabond was used as layer 2. When PVC Foam and aluminum were used as layer 2, only PP reflections were observed. As discussed previously, this is due to the fact that most P-wave incident energy was reflected back at the top of PVC Foam and aluminum.

A good image of the top of layer 4 was obtained by using PSPPSP reflections when Plexiglas and Trabond were used as layer 2. This observation could be useful for seismic imaging in the Canadian Beaufort Sea. In the Canadian Beaufort Sea, several layers of permafrost (high P-wave velocity) overlie one another (Poley and Lawton, 1991). As discussed in chapter 2, the P-wave velocities in Plexiglas and Trabond are close to that of permafrost in the Canadian Beaufort Sea. Poley and Lawton (1991) showed that it is difficult to obtain a good image of the top of the second layer of ice-bearing permafrost (equivalent to layer 4 in our physical model) by using conventional P-wave reflections (PPPPPP). The results of this research shows that it is possible to obtain a better image of the top of the second layer of ice-bearing permafrost by using multiconverted reflections (PSPPSP).

In Figure 4.14, the two-way zero-offset travelttime difference between the PPPPPP reflection and the PSPPSP reflection is small. This is mainly due to the fact that layer 2 is very thin (31 m after scaling) in our physical model, and the two-way travelttime difference between the P-mode and S-mode is small. Therefore, there is not much time difference between PPPPPP and PSPPSP reflections. This could be a problem in using multiconverted reflections to image the top of layer 4 when both PPPPPP and PSPPSP

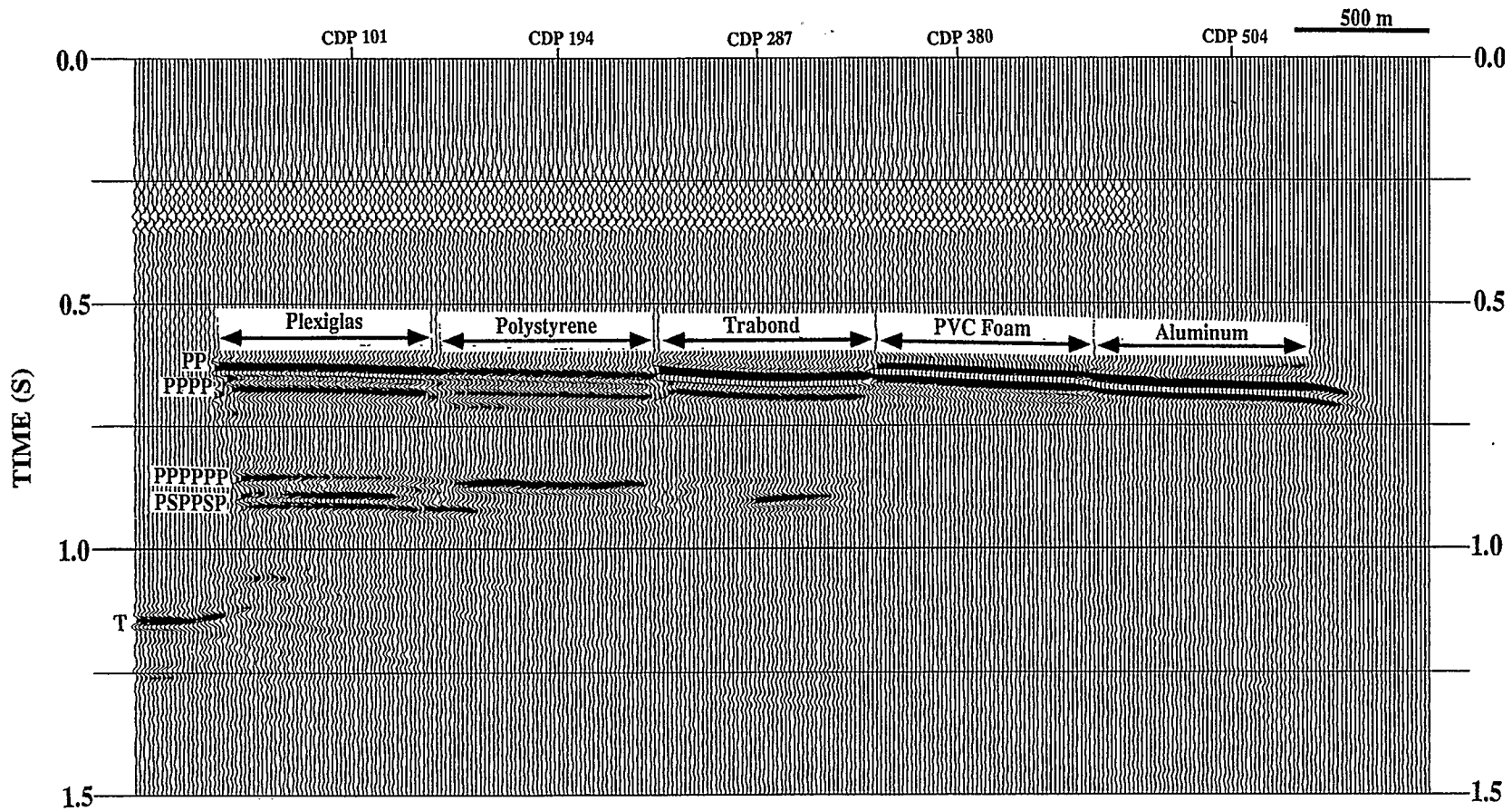


FIG. 4.14. Final migrated section for the physical modeling data. Five CMP locations (shown from Figure 4.6 to Figure 4.10) are marked. PP = P-wave reflection from the top of layer 2 (Plexiglas, polystyrene, Trabond, PVC Foam and aluminum); PPPP = P-wave reflection from the base of layer 2; PPSPPSP = P-wave reflection from the top of layer 4 (aluminum); PPSPPSP = multiconverted reflections from the top of layer 4; T = P-wave reflection from the top of the Plexiglas table.

events are present in the shot gathers (such as in the physical modeling case). However, these two reflections can be separated since they tend to occur over different offset ranges (Figures 4.12 and 4.13). Hence, partial offset stacks can be used to produce PPPPP and PSPPSP images of the same reflector.

Chapter 5: Multiconverted reflection analysis for the Canadian Beaufort Sea data

5.1 Introduction

Sea level in the Canadian Beaufort Sea during Pleistocene glacial cycles was about 100 m lower than the present (Poley et al., 1989). As a result, in the Arctic climatic condition, a thick sequence of sediments became frozen in that environment (Poley, 1987; Poley et al., 1989). This ice-bearing permafrost has a very high P-wave velocity (about 3000 m/s) compared with that of the surrounding sediments in which the P-wave velocity is around 1600 m/s, which is only slightly higher than the P-wave velocity in water. Therefore, in this marine environment, a high-velocity permafrost layer occurs near the sea floor.

Two data sets were made available to the study: high-resolution site survey data (dataset A) and a conventional exploration data set (dataset B). These two data sets were processed in this study, in an attempt to identify and process multiconverted events.

5.2 Dataset A

5.2.1 Introduction

The distribution of the ice-bearing permafrost in the Canadian Beaufort Sea is of significant importance to gravel mining and to the drilling of production wells in the region (Poley and Lawton, 1991). As discussed earlier, ice-bearing permafrost occurs in up to six discrete horizons (*D1* to *D6*). Due to the strong screening effect of the shallowest (*D6*) layer, seismic reflections from the second (and deeper) permafrost layer are not clear on conventional P-wave data.

Dataset A was reprocessed, with a focus on examining the data for multiconverted reflections in order to determine whether these events could provide a better image of the reflections below the *D6* layer. The physical and numerical modeling results presented in previous chapters were used to assist processing and interpretation of the field data.

Figure 5.1a shows a shot gather of dataset A, with the time window of 0 to 0.4 s. The P-wave reflection event for the top of the *D6* layer was identified by Poley and Lawton (1991). At a travelttime of around 0.2 s in Figure 5.1a, there is an event which occurs in the middle offset range, which is interpreted to be a PSSP reflection from the bottom of the *D6* layer (the first ice-bearing permafrost layer). Also for the travelttime around 0.3 s, there is another event which occurs at far offsets which is interpreted to be a PSPPSP reflection from the top of *D5* (the second ice-bearing permafrost layer). This interpretation was based on the physical and numerical modeling results discussed in chapters 2 and 3. In Figure 2.1a, for instance, the PP reflection occurs at a time of 0.54 s, with an equivalent depth of 410 m, which is about a quarter of the maximum source-to-receiver offset (1550 m). The multiconverted reflection occurs at the middle offset. Similarly, in Figure 5.1a, the PP reflection occurs at the time of 0.12 s, with an equivalent depth of 90 m, which is about a quarter of the maximum source-to-receiver offset (362.5 m). The multiconverted reflection occurs at the middle offset also.

This interpretation was verified by the synthetic seismogram shown in Figure 5.1b. In this seismogram, PP, PSSP and PSPPSP reflections arrive at about the same time and with the same moveout as the corresponding reflections on the field data in Figure 5.1a. Figure 5.2 shows the parameters used in the synthetic modeling. As discussed in chapter 2, both layer 2 and layer 4 are high-velocity layers, representing two layers of ice-bearing permafrost (*D6* and *D5*). Both layer 1 and layer 3 are water layers. The data were processed using both conventional and newly developed processing procedures, which are described in detail in the remainder of this chapter. Figure 5.3 is the conventional processing flow chart for the dataset A.

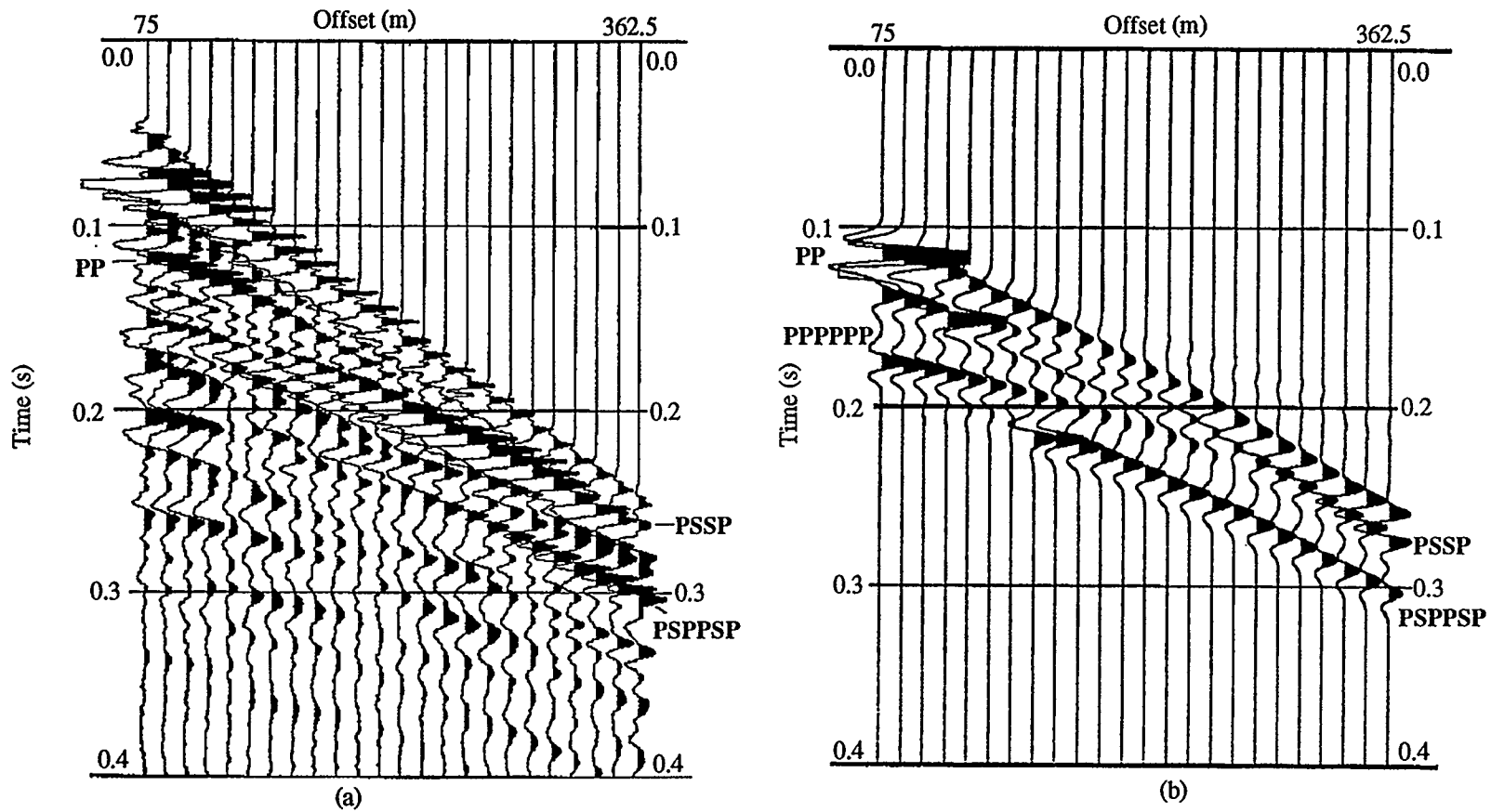


FIG. 5.1. (a) A shot-gather example of dataset A, Canadian Beaufort Sea. (b) Synthetic seismogram. PP = P-wave reflection from the top of the first ice-bearing permafrost layer; PSSP = multiconverted reflection from the base of the first ice-bearing permafrost layer; PPSPP = P-wave reflection from the top of the second ice-bearing permafrost layer; PSPPSP = multiconverted reflection from the top of the second ice-bearing permafrost layer.

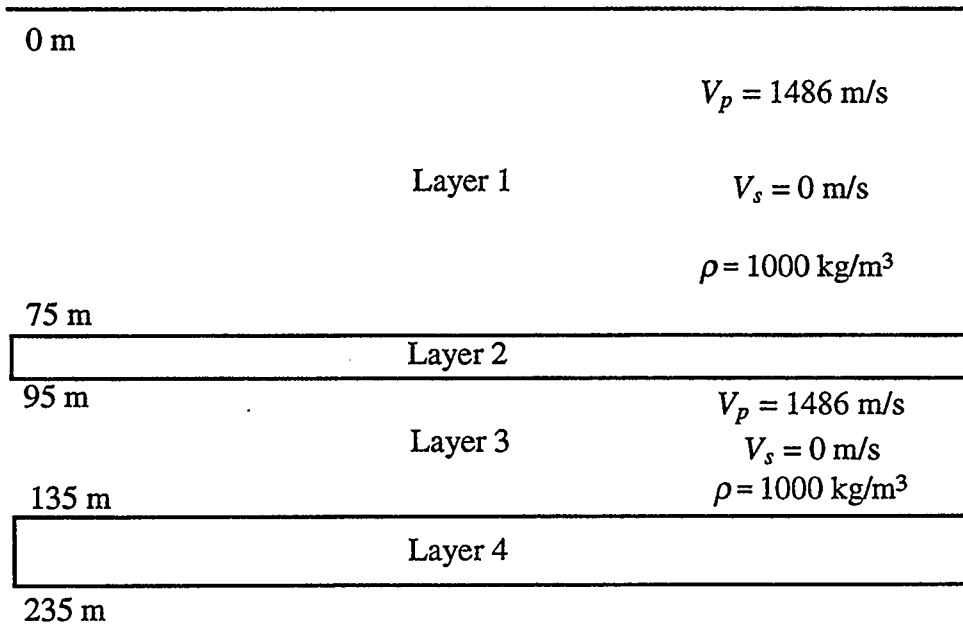


FIG. 5.2. Schematic diagram showing the model for synthetic seismogram in Figure 5.1b. Both layer 2 and layer 4 are high-velocity layers, with $V_p = 3000 \text{ m/s}$, $V_s = 1500 \text{ m/s}$, and $\rho = 1200 \text{ kg/m}^3$. V_p = P-wave velocity, V_s = S-wave velocity; ρ = density.

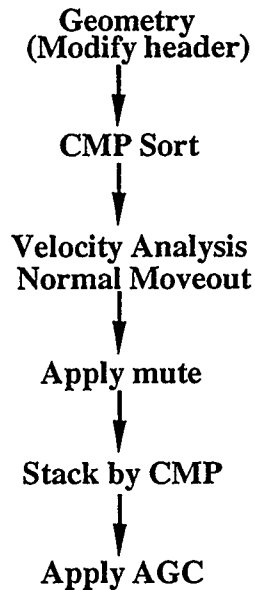


FIG. 5.3. The conventional seismic data processing flow chart for the dataset A, Canadian Beaufort Sea.

5.2.2 Preprocessing

The data were already demultiplexed, hence, preprocessing included only the field geometry. The geometry for the high-resolution site survey data is listed in Table 5.1.

Table 5.1. Acquisition geometry for the dataset A

Shots:	100
Receivers/shot:	24
Group interval (m):	12.5
Shot interval (m):	6.25
Maximum Fold:	24
Near offset (m):	75
Far offset (m):	362.5
Sample rate (ms):	1
Record length (s):	2

5.2.3 CMP sorting, velocity analysis, NMO correction and mute

As discussed in chapter 4, the traces in the collection of shot records are sorted into common midpoint (CMP) gathers before stacking the data. Velocity semblance analysis was undertaken for CMP gathers. The NMO correction was undertaken for CMP gathers based on the velocities picked by semblance analysis. Figure 5.4 shows an example of an NMO corrected CMP gather and shows the problem of severe NMO-stretch of the PSSP and PSPPSP events after application of the NMO correction. A mute pattern was chosen to mute these stretched events prior to stacking the data. The mute pattern is shown as a dashed line in Figure 5.4.

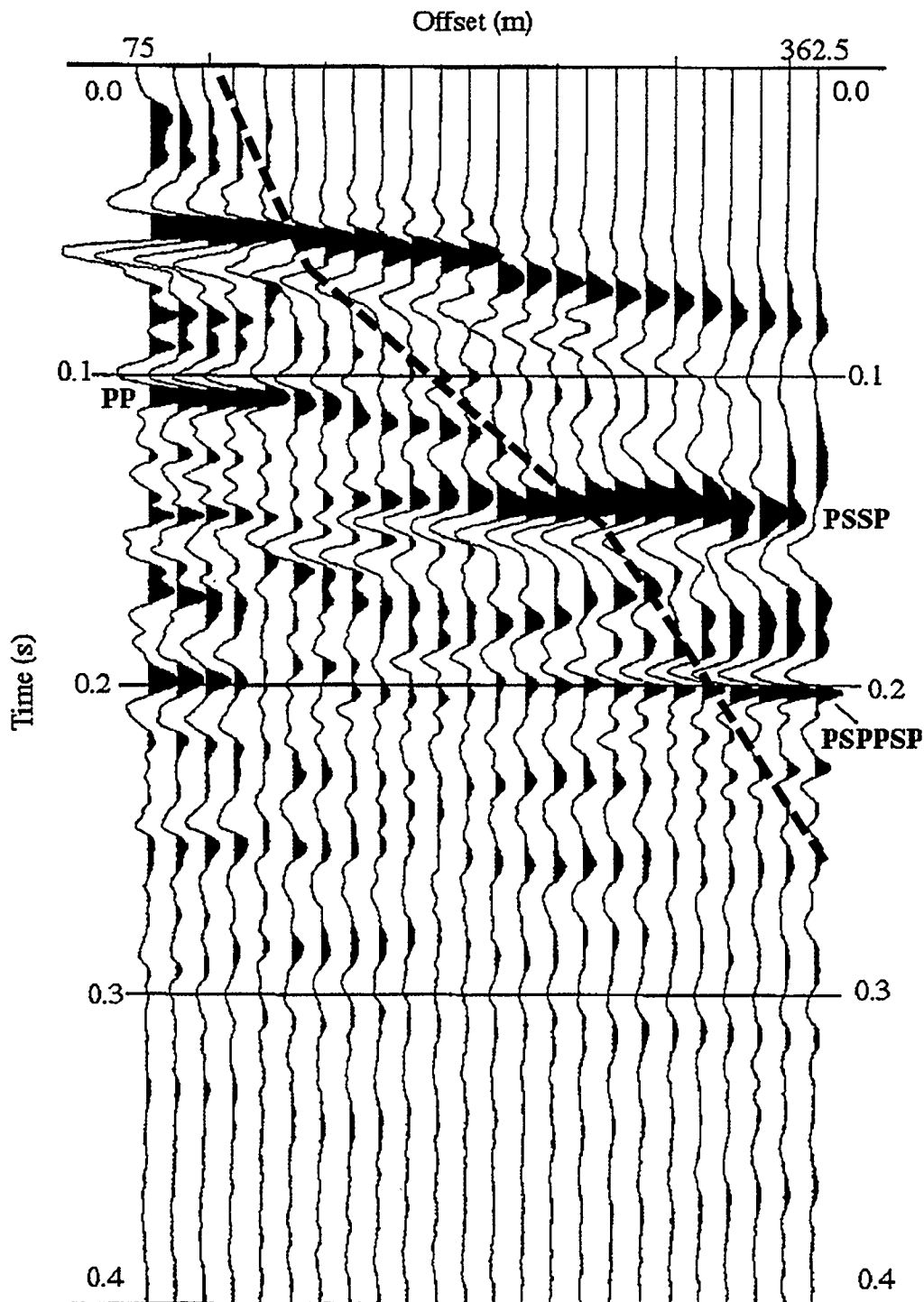


FIG. 5.4. NMO corrected CMP gather, without applying the mute.
 PSSP = Multiconverted reflection from the base of the first ice-bearing permafrost layer; PSPPSP = Multiconverted reflection from the top of the second ice-bearing permafrost layer. The mute pattern is shown as a dashed line.

5.2.4 Stack and AGC

In the CMP domain, all traces in one CMP are summed together to get one single trace to enhance the signal-to-noise ratio. AGC gain was applied to enhance the deep reflections on the seismic data. Figure 5.5 shows the final stacked section, on which AGC gain was applied with a time window of 250 ms. PP refers to the P-wave reflection for the top of the first ice-bearing permafrost layer, and PSSP is the multiconverted reflection from the bottom of the first ice-bearing permafrost layer.

5.2.5 Discussion

Dataset A was processed using conventional procedures. On the stacked section (Figure 5.5), the PP reflection was well imaged using these standard processing procedures. The PSSP event was well imaged on the right side of the stacked section, but not on the left side (Figure 5.5). This may be due to the mute pattern chosen for this data. For the particular geometry used for acquiring this data, the near-offset traces of the shot gather contribute more on the right side of the stacked section, while the far-offset traces of the shot gather contribute more to the left side of the stacked section (Figure 5.5). Far-offset traces were muted out before stacking the data.

The multiconverted reflection PSPPSP is absent on the stacked section (Figure 5.5). This is due to the fact that the PSPPSP reflection was muted out on the CMP gather (Figure 5.4). In order to image the PSPPSP reflection, a different approach to the correction for normal moveout was undertaken to avoid NMO stretch.

5.3 Postcritical seismic data processing for the dataset A

5.3.1 Introduction

Conventional seismic processing includes the normal moveout (NMO) correction. As mentioned above, a mute is applied after the NMO correction to reduce the detrimental effects of wavelet stretch.

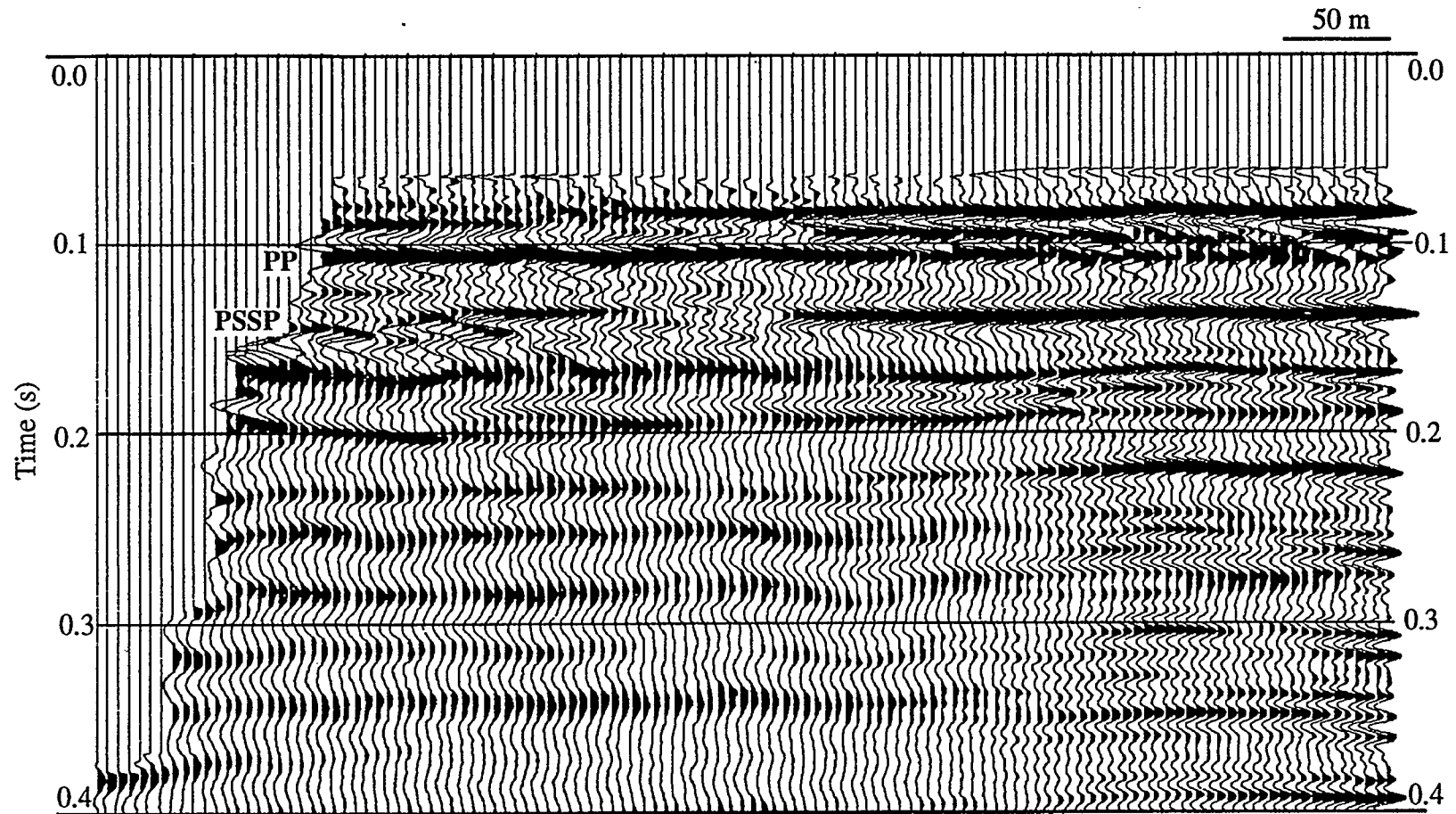


FIG. 5.5. Stacked section using conventional processing procedures, dataset A. PP = P-wave reflection from the top of the first ice-bearing permafrost layer; PSSP = multiconverted reflection from the base of the first ice-bearing permafrost layer.

The goal is to perform NMO correction without stretching the wavelet. Rupert and Chun (1975) undertook early research to apply NMO correction without wavelet stretch by using a 'block-move-sum' method. Their approach was to divide the zero-offset trace into several time blocks (each block can be overlaid with one another). Then the starting and ending points of each block were projected from the zero-offset trace to far-offset traces along the reflection hyperbolas for a particular velocity. Therefore, blocks on the far-offset trace have the same block length as those on the near-offset trace. Data blocks were corrected for NMO as a unit, and the overlapping values on far-offset traces were summed and normalized by the degree of stack. Rupert and Chun (1975) commented on the limitation of their method, such as the ambiguity of choosing the block length and block-shift, as well as the position in the block at which the velocity should be chosen. For a small time shift (such as 2 ms for a block length of 100 ms), the block-move-sum method created a muted appearance for the far-offset traces (Rupert and Chun, 1975). On the other hand, if the time shift is large (such as 100 ms for a block length of 100 ms), then some duplication would occur at the far-offset trace. Hence this method is not suitable for our case, since we do not want any distortions on the far-offset traces.

5.3.2 'Block-shift' NMO correction method

Our approach is to apply a block-shift NMO correction for a particular event to all traces in a CMP gather, similar to applying a statics shift. This is done for one event only (or for all the events which have the same rms velocities). All events are treated individually, after which all corrected events can be spliced into one gather, resulting in NMO-corrected gathers which have minimal wavelet distortions on the far traces. This approach is successful only in sparse reflectivity sequences and where offset-dependent tuning effects are absent. Figure 5.6 summarizes the 'block-shift' NMO correction procedure. The symbols used in Figure 5.6 are defined as:

- np : the total number of points (samples) in one trace;
 nt : the total number of traces in a CMP gather;
 nc : the total number of CMP for the whole survey;
 Δt_{nmo} : NMO moveout correction;
 k : the counter representing the CMP number ranging from 1 to nc ;
 i : the counter representing the trace number ranging from 1 to nt ;
 j : the counter representing the sample number ranging from 1 to np ;
 V_{rms} : the rms velocity for a particular layer;
 t_0 : the two-way vertical traveltime from source-to-receiver;
 x : the source-to-receiver offset.

The first step in the processing flow (Figure 5.6) is to input the first CMP gather ($k=1$). Suppose the CMP gather data matrix is: $data1(j, i)$. The next step is to calculate the NMO correction for specified values of V_{rms} and t_0 which are obtained through velocity analysis. The NMO correction (Δt_{nmo}) is given by:

$$\Delta t_{nmo} = \sqrt{t_0^2 + \frac{x^2}{v_{rms}^2}} - t_0. \quad (5.2)$$

In equation (5.2), Δt_{nmo} is the NMO correction which is unknown; t_0 is the two-way zero-offset time and V_{rms} is the rms velocity; x is the source-to-receiver offset. The next step is to let $n = int(\Delta t_{nmo})$, i.e., let n to be the nearest sample number of Δt_{nmo} ($n \leq \Delta t_{nmo}$), where n is an integer. The reason for that is because the sample interval for these data is 1 ms.

The next step after the NMO calculation is to obtain the NMO corrected data matrix: $data(j, i)$. First, suppose l is an another integer (variable). $Data(l, i)$ can be obtained by:

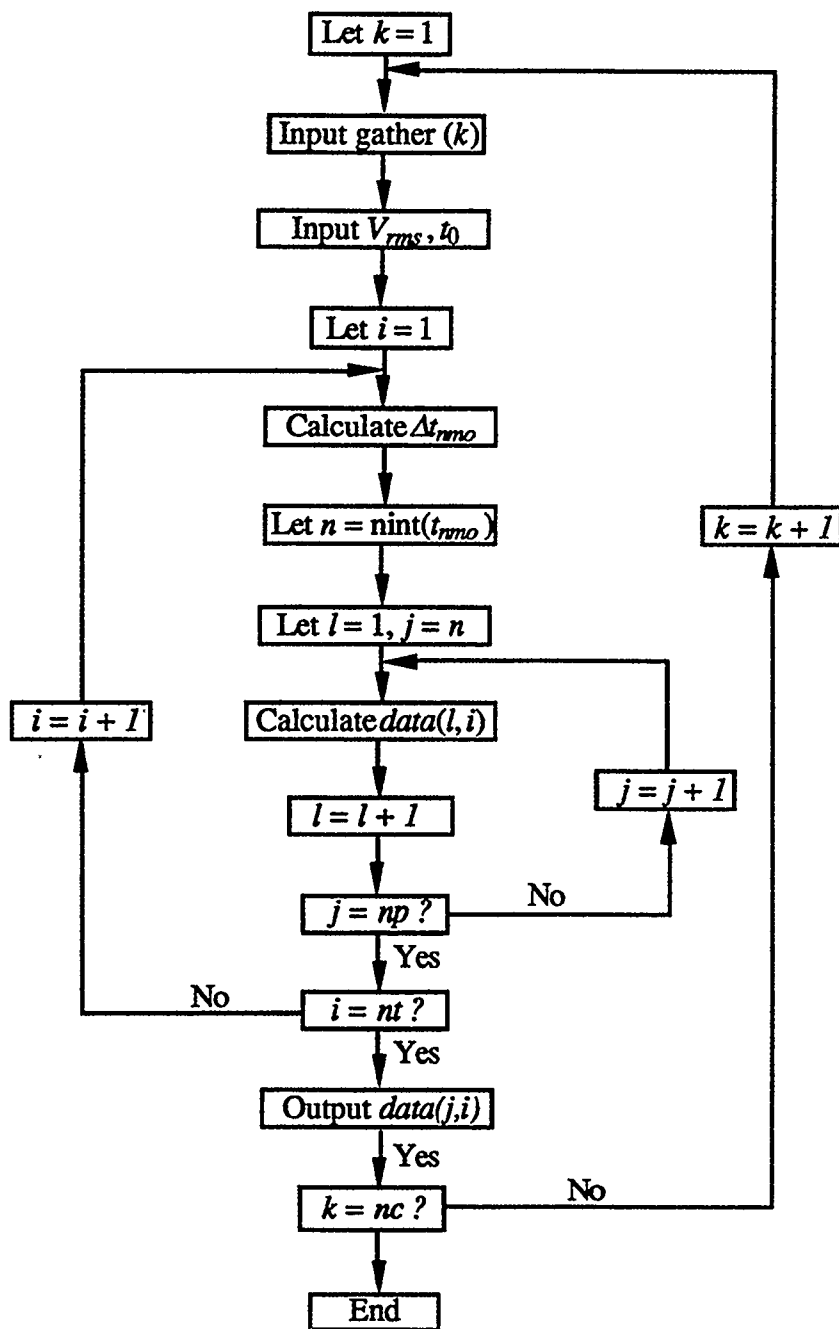


FIG. 5.6. Calculation procedure for 'block shift' NMO correction. k = the counter representing the CMP number ranging from 1 to nc (nc is the total number of CMP in the survey); i = the counter representing the trace number ranging from 1 to nt (nt is the total number of trace in one CMP gather); j = the counter representing the sample number ranging from 1 to np (np is the total number of sample in one trace).

$$data(l,i) = data1(j,i) + \frac{data1(j+1,i) - data1(j,i)}{t_{nmo} - n}, \quad (5.3)$$

for $j = 1$ to np and $i = 1$ to nt .

Equation (5.3) uses an interpolation method to get the matrix $data(l, j)$; $data1(j, i)$ is the input matrix. After this step, the output matrix $data(j, i)$ is NMO corrected for the selected event, without stretching the wavelet.

5.3.3 Results

Figure 5.7 shows the same NMO corrected CMP gather as in Figure 5.4, but with the application of a 'block-shift' NMO correction. Figure 5.7a shows the 'block-shift' NMO corrected CMP gather for the PSSP event, with a t_0 of about 0.14 s, and Figure 5.7b shows the 'block-shift' NMO corrected CMP gather for the PSPPSP event, with a t_0 of about 0.2 s. Here, two different pairs of t_0 and V_{rms} were chosen for PSSP and PSPPSP reflections to obtain Figures 5.7a and 5.7b. For both cases, it is not necessary to apply a mute, since there is no NMO stretch for the selected event after the correction has been applied.

This new approach for NMO correction was applied to the dataset A. Figure 5.8 shows the processing flow for the newly developed processing procedure. Compared with the conventional processing procedure (Figure 5.3), the big difference is how the NMO correction was applied. Two different stacked sections were obtained for PSSP and PSPPSP reflections respectively, then were spliced to get one final stacked section for both PSSP and PSPPSP reflections (Figure 5.9). The splice windows are from 0 to 0.17 s for PSSP and from 0.17 s to 0.4 s for PSPPSP. In Figure 5.9, PSSP refers to the multiconverted reflections from the bottom of the first ice-bearing permafrost layer ($D6$), and PSPPSP is the multiconverted reflection from the top of the second ice-bearing permafrost layer ($D5$). Comparing the stacked section in Figure 5.9 with the stacked section in Figure 5.5, it is clear that a better image of the top of the $D5$

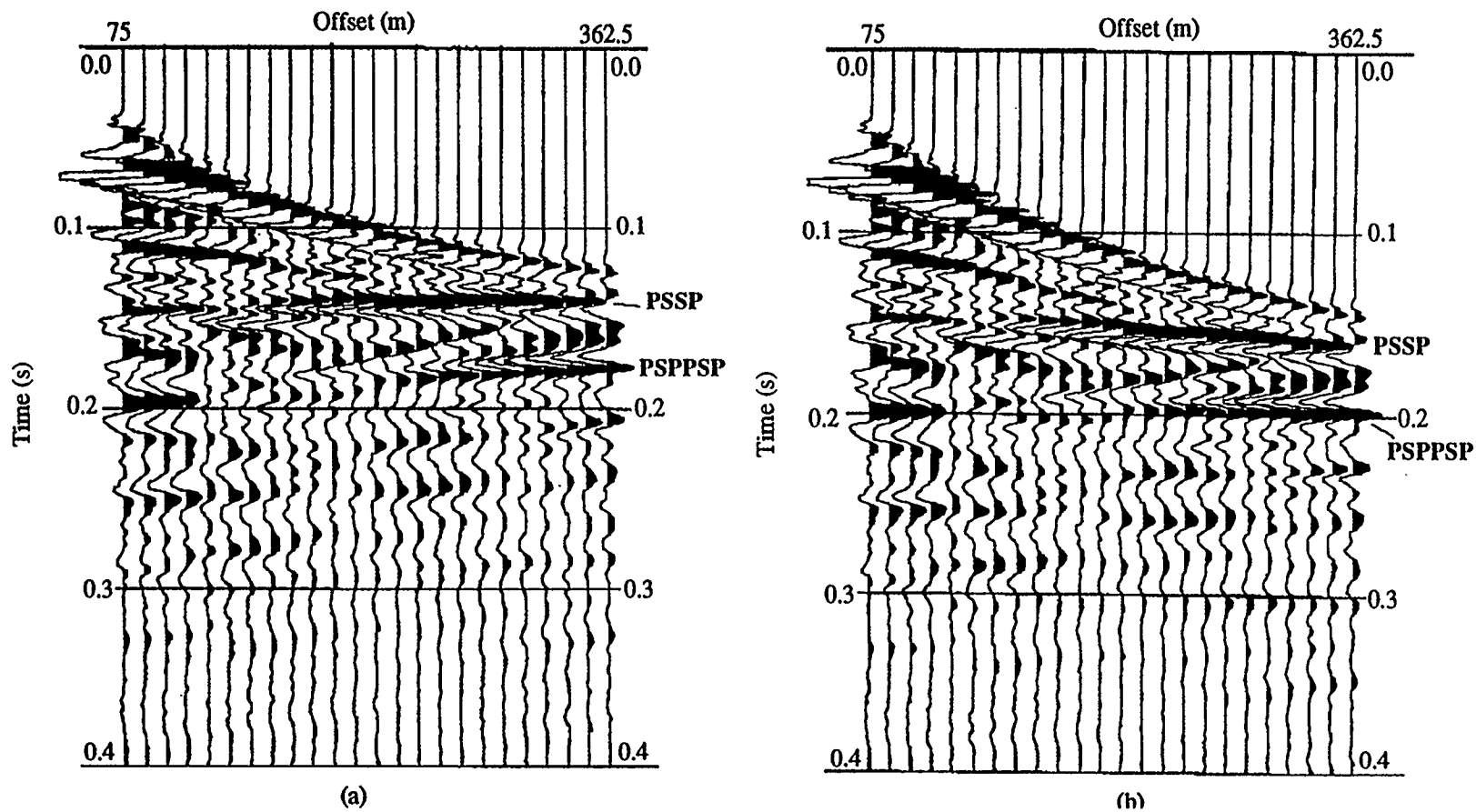


FIG. 5.7. 'Block shift' NMO-corrected gathers, using the same CMP gather, as shown in Figure 5.4. PSSP = multiconverted reflection from the base of the first layer of ice-bearing permafrost; PSPPSP = multiconverted reflection from the top of the second layer of ice-bearing permafrost. (a) PSSP event is corrected using a t_0 of 140 ms; (b) PSPPSP event is corrected using a t_0 of 200 ms.

(PSPPSP) was obtained by using the newly developed processing flow (Figure 5.8). However, there are still some pitfalls in this approach. For instance, we have to physically splice every stacked section for each pair of t_0 and V_{rms} . This is tedious and time-consuming. Also, this approach is not feasible when there is a crossing of two events, or when the time difference between two events is too small to splice.

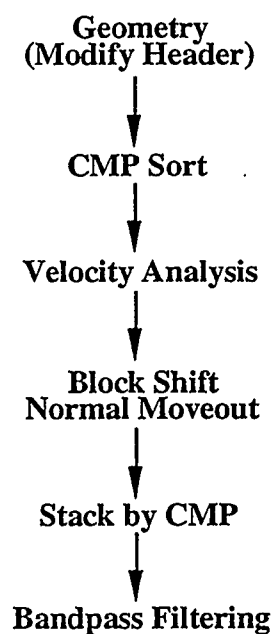


FIG. 5.8. Processing flow with 'block-shift' normal-moveout application, dataset A.

5.3.4 Discussion

Dataset A was reprocessed using 'block-shift' NMO processing procedures in order to get a better image of the top of the second ice-bearing permafrost layer ($D5$). It appears that a better image has been obtained using the newly developed processing procedure. The shallow, far-offset multiconverted reflections (PSSP and PSPPSP) were preserved through using the 'block-shift' NMO correction method.

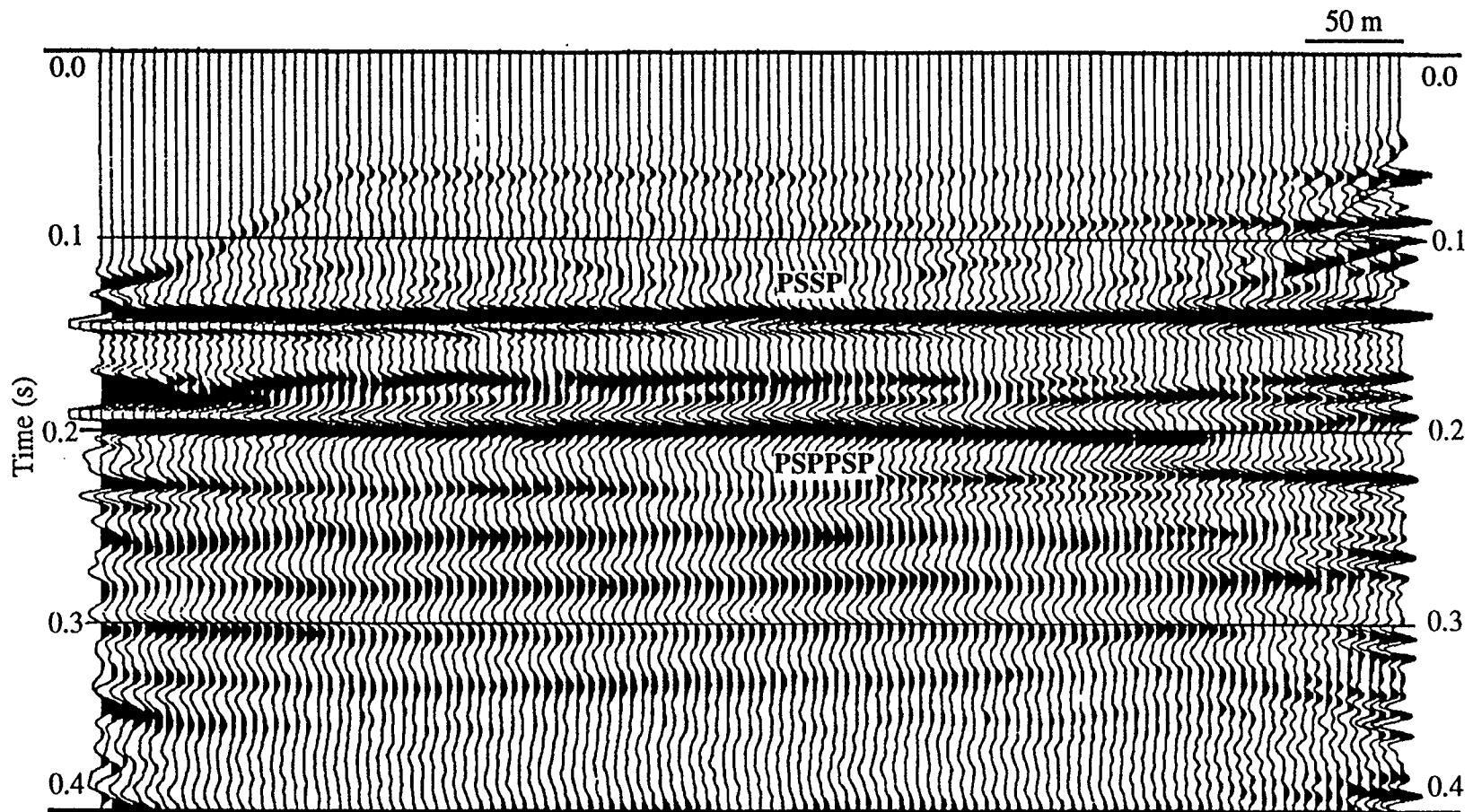


FIG. 5.9. Stacked section using 'bulk shift' NMO correction, dataset A. PSSP = multiconverted reflection from the base of the first ice-bearing permafrost layer; PSPPSP = multiconverted reflection from the top of the second ice-bearing permafrost layer.

For the particular geometry used for acquiring this data, the near-offset traces of the shot gather contribute more on the right side of the stacked section, while the far-offset traces of the shot gather contribute more to the left side of the stacked section (Figure 5.9). Therefore, the PSPPSP reflection on the right is not as clear as on the left (Figure 5.9). This is due to the fact that the multiconverted reflections mainly occur at the far-offset traces on shot gathers.

5.4 Dataset B

5.4.1 Introduction

In dataset A, multiconverted reflections from shallow horizons were processed to obtain an image of the top of the second ice-bearing permafrost layer (*D5*). Dataset B is the conventional exploration data, which were processed with a focus on deeper single-mode reflections. The purpose of this processing was to evaluate the effect of thin, high-velocity shallow layers on the ability to image deep reflectors in the Canadian Beaufort Sea.

Figure 5.10 shows the processing flow for the dataset B. Each step is described in detail in the following sections.

5.4.2 Preprocessing

The data were already demultiplexed, therefore, preprocessing included only the field geometry. The acquisition geometry is listed in Table 5.2.

Figure 5.11 is an example of a shot gather. Generally, the data quality is poor, and the record is dominated by linear noise (A & B in Figure 5.11) in the lower half of the section. These linear coherent noise trains were interpreted as off-line reflections from floating sea ice (Poley et al., 1989). The shallow ice-bearing permafrost layers occur near the sea floor, identified by the strong refractions with an apparent velocity around 3100 m/s (marked with *R*) in Figure 5.11. The direct arrival (marked with *D*)

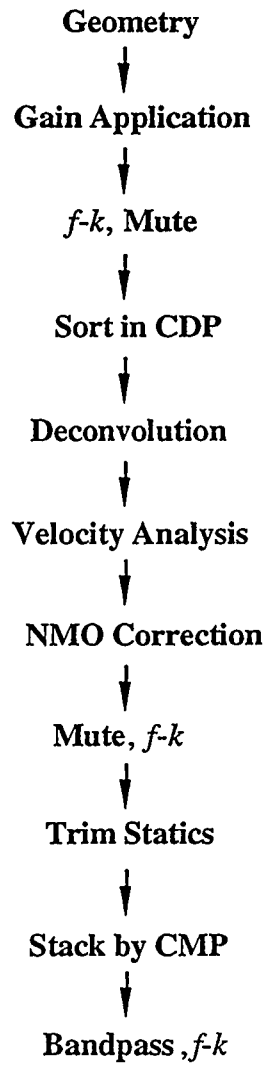


FIG. 5.10. Seismic data processing flow for the dataset B.

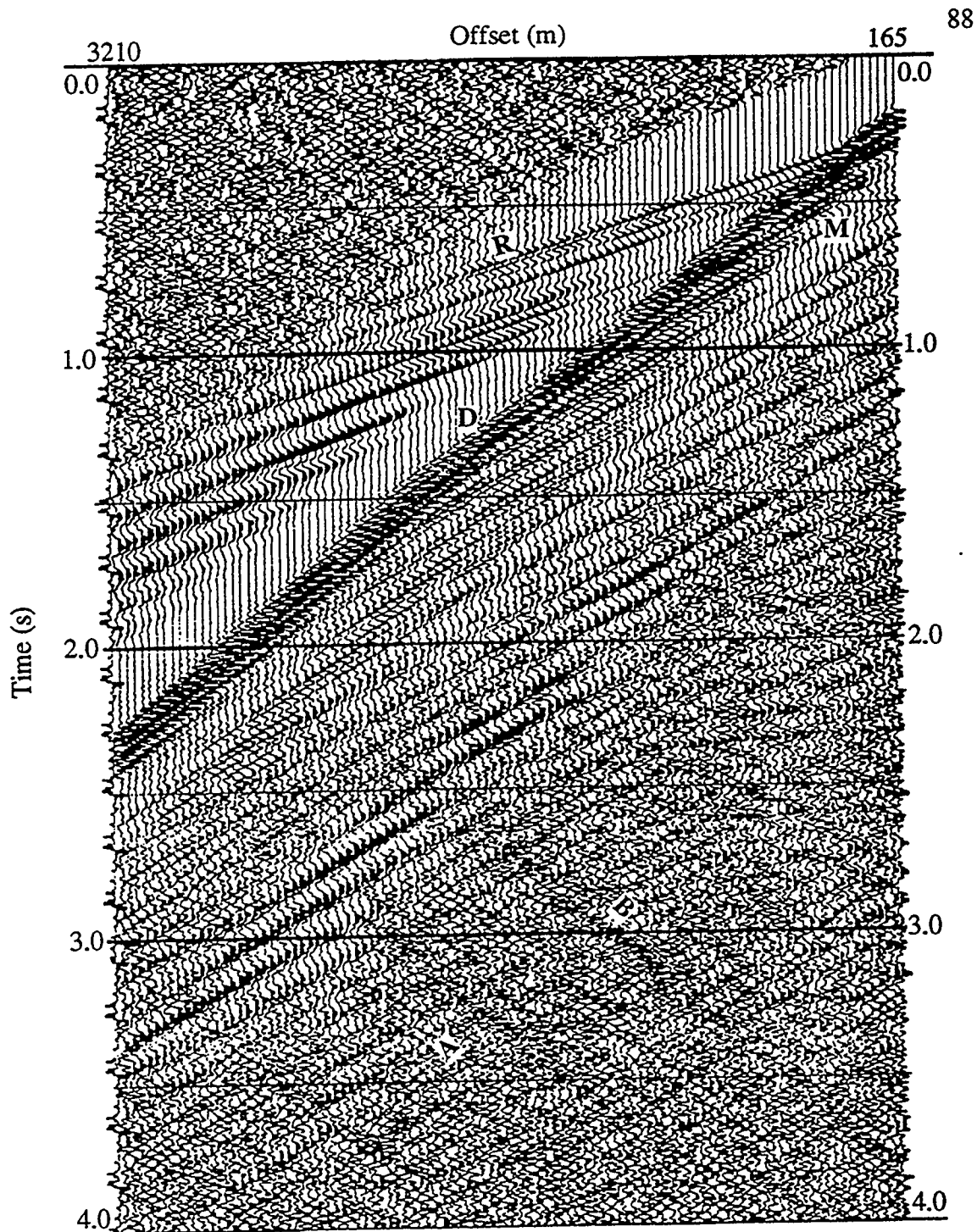


FIG. 5.11. A shot gather for the dataset B in the Canadian Beaufort Sea (plotted for every second trace). AGC was applied with a time window of 500 ms. R: refraction energy; D = Direct arrival; M = Multiconverted reflections and their multiples; A & B = off-line energy.

has a large amplitude. All events marked with M are interpreted to be multiconverted reflections and their multiples. These events are asymptotic to the direct arrival at the far-offset traces, meaning that the rms velocity of these events is close to the P-wave velocity in water. As discussed in chapter 2, the S-wave velocity in the ice-bearing permafrost layers is about the same as the P-wave velocity in water.

Due to the poor quality of the data, only a few reflections (between the time 2.2 s and 2.9 s) are evident in the shot gather in Figure 5.11. These events become indistinguishable from linear noise in the middle offset range. Also on the shot gather in Figure 5.11, two bad traces occur at the far-offset. It is necessary to do the trace editing in the procedure of preprocessing.

Table 5.2. Acquisition geometry for the dataset B

Shots:	100
Receivers/shot:	204
Group interval (m):	15
Shot interval (m):	30
Maximum fold:	51
Near offset (m):	165
Far offset (m):	3210
Sample rate (ms):	4
Record length (s):	8

5.4.3 Gain

Both deterministic and statistical gains were applied to the data. The deterministic gain mainly attempts to calculate a gain function by taking into account the physical effects which cause the amplitude to decay, such as geometrical spreading. The statistical gain uses an arbitrary gain function to scale down the high amplitudes of shallower reflections and scale up the low amplitudes of later reflections.

Geometrical spreading gain was applied to the data. The amplitude of each sample was scaled by a factor of the traveled distance. The traveled distance for each sample was calculated by multiplying the stacking velocity (obtained from velocity analysis) with the traveling time. AGC gain with a time window of 500 ms and a bandpass filter with the frequency range of 10 to 60 Hz were also applied to the shot gathers before applying the prestack f - k dip filtering. AGC was used to suppress possible spikes in the shot gathers. Convolution of the f - k dip filter operator with spikes in the time domain damages the data.

5.4.4 f - k filtering and mute

As discussed above, some linear noise (marked with A and B) and multiples (marked with M) appear on the shot gather in Figure 5.11. Events that dip in the (t, x) plane can be separated in the (f, k) plane by their dips (Yilmaz, 1987). This allows us to eliminate some unwanted events on the shot gathers. A prestack f - k filter with the rejected apparent velocity zone from -2,000 m/s to 2,000 m/s was applied to the dataset B, since the noise has an apparent velocity around 1,500 m/s (A & M) and -1,500 m/s (B). Figure 5.12 is the same shot gather as shown in Figure 5.11, but with the f - k dip filtering and mute applied. Notice that almost all events that have the linear moveout in Figure 5.11 are eliminated. Also notice that the signal-to-noise ratio is increased by applying the prestack f - k dip filtering, especially for two events around the time of 2.4 s (marked with R in Figure 5.12).

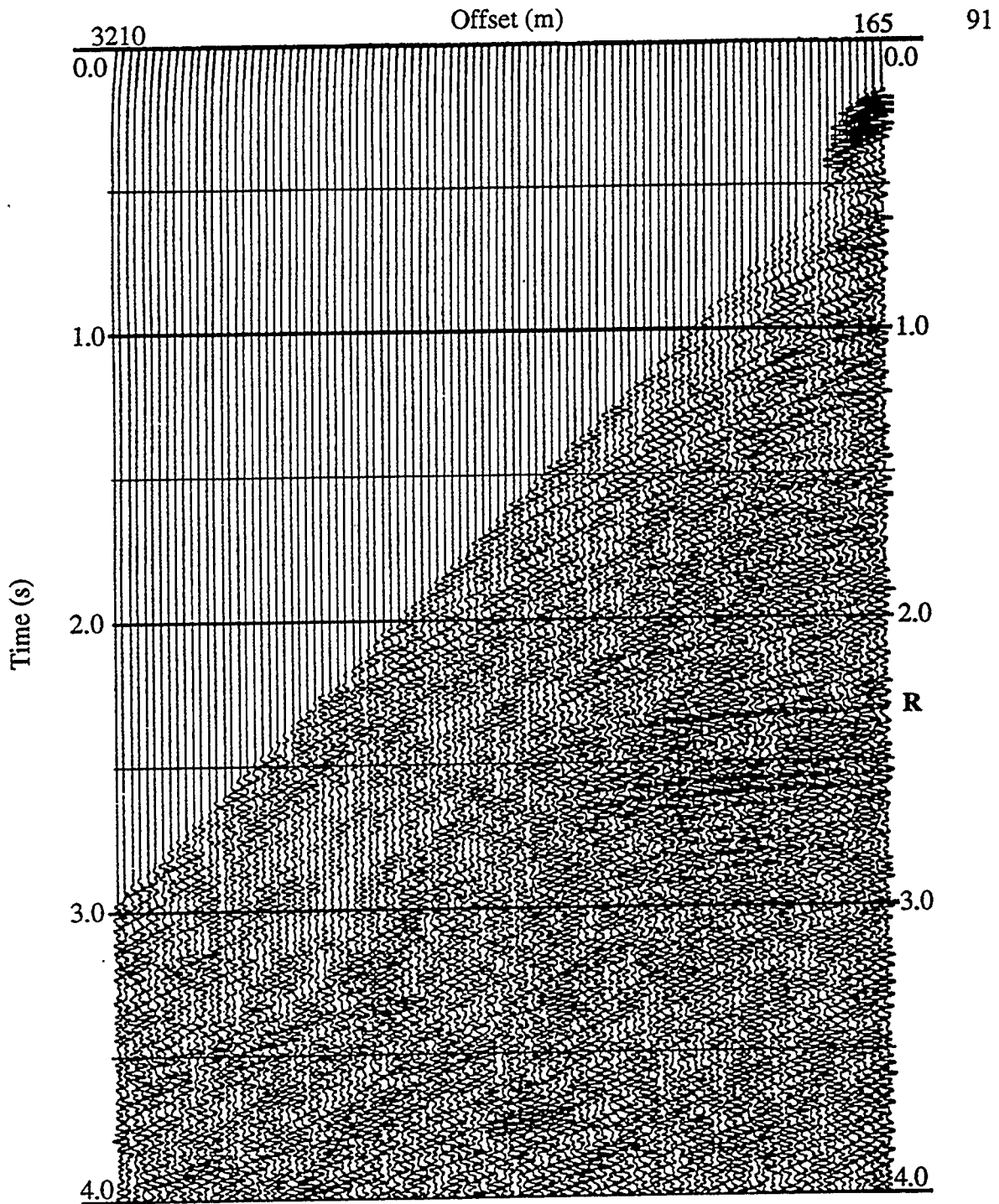


FIG. 5.12. The same shot gather as shown in Figure 5.11, but with prestack f - k filtering and mute applied. AGC was applied with a time window of 500 ms. R = reflection energy.

5.4.5 CMP sorting and deconvolution

The traces in the collection of shot records were sorted into CMP gathers. For the dataset B, the shot interval is twice of the group interval, therefore, the maximum trace number in one CMP gather is 51 (i.e., the maximum fold is 51). These traces in one CMP gather can be stacked to get one single trace after NMO correction of all the traces in the gather.

As discussed in chapter 4, deconvolution was used for data processing to improve the seismic resolution by compressing the seismic wavelet. In this study, gather-oriented minimum phase spiking deconvolution was applied to the dataset B, using a Levinson recursion method with a 100-ms time window for estimation of the wavelet, and the deconvolution was applied within the window from 400 ms to 3000 ms to the data.

5.4.6 Velocity analysis and NMO correction

As mentioned in chapter 4, the data have to be NMO-corrected before stacking in the CMP domain, and the velocity analysis is necessary to obtain rms velocities for the NMO correction. The signal-to-noise ratio is very low in Figure 5.12, compared with the previous data (dataset A) as illustrated in Figure 5.1a. This leads the difficulty in picking velocities on CMP gathers. However, higher signal-to-noise ratio can be obtained by generating common-offset stacked CMP gathers within a certain range of CMP gathers (20 CMPs for the dataset B). As a result, the signal-to-noise ratio was enhanced for the velocity analysis. Table 5.3 shows two pairs of rms velocities (for CMP 373 and CMP 703), which were obtained from the velocity analysis using common offset stacked sections.

5.4.7 Mute and f - k filtering

Figure 5.13 shows a CMP gather after a mute was applied to eliminate problems with NMO stretch. A strong event (marked with *M*) occurs in the lower half section,

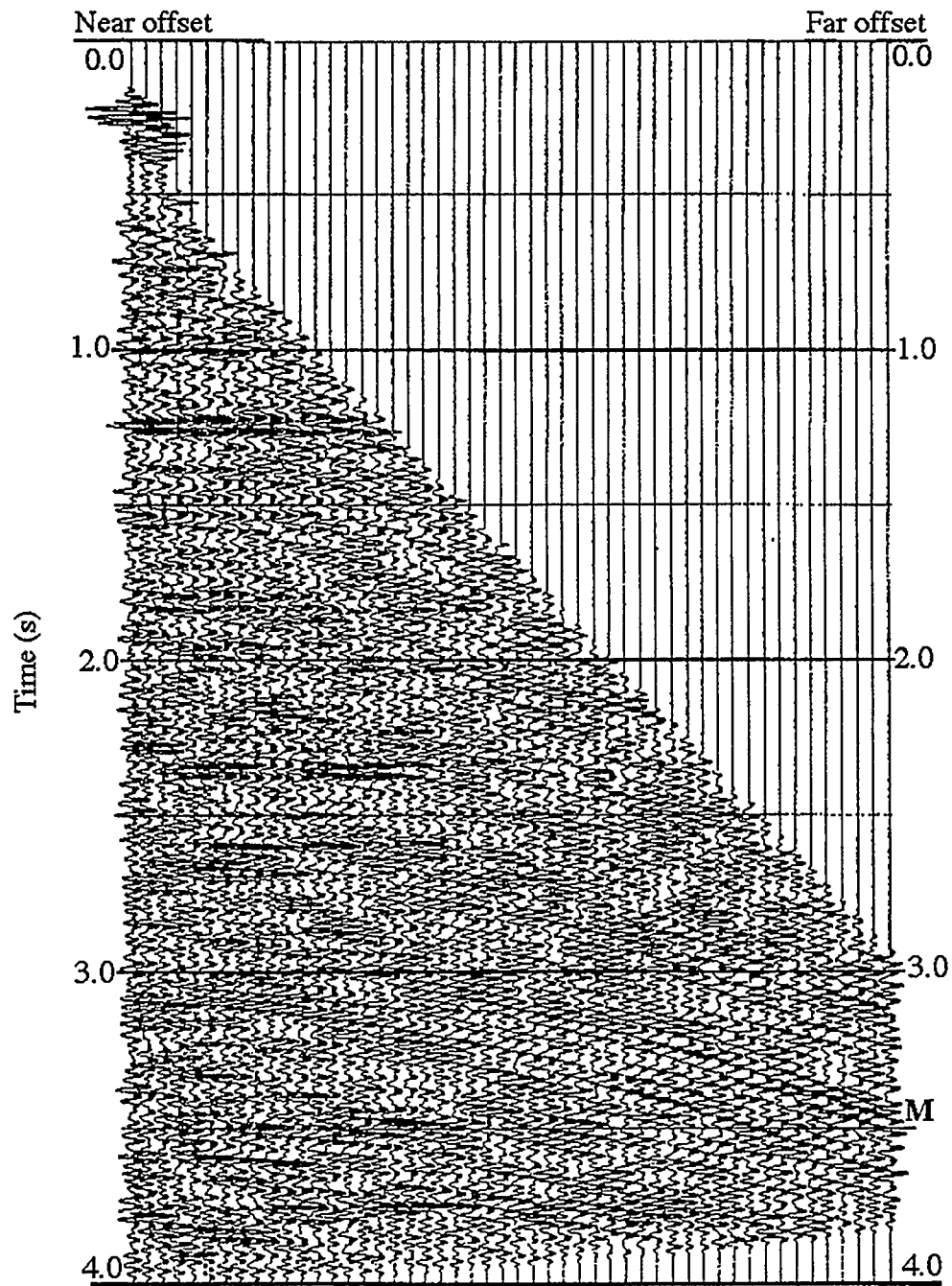


FIG 5.13. NMO-corrected CMP gather for the dataset B. M: Multiples.

Table 5.3 RMS velocities obtained from the velocity analysis

Time (ms)	Velocity (m/s) (CMP 373)	Velocity (m/s) (CMP 703)
0	1800	1805
540	1800	1805
720	1835	1836
1000	1900	1904
1250	1950	1950
1280	2057	1966
1700	2070	2011
1900	2200	2170
2350	2310	2280
2550	2340	2300
2850	2350	2330
3000	2370	2380
3450	2500	2500
3700	2835	2840

and this was interpreted as a multiple (reverberation energy trapped in the ice-bearing permafrost layer). Therefore, $f-k$ filtering was chosen to eliminate this event. Figure 5.14 shows the same CMP gather in Figure 5.13, but with $f-k$ filtering applied. The rejected velocity zone with the apparent velocity from -5,000 m/s to 5,000 m/s was chosen for the $f-k$ filtering.

5.4.8 Trim statics

After NMO correction, all traces for a particular event should be horizontally corrected. However, there is some residual moveout amount left after the NMO correction because of inaccuracies in the rms velocities picked by the velocity analysis. Trim statics with a maximum shift of ± 8 ms and a time window from 500 ms to 3500 ms was applied to the dataset B.

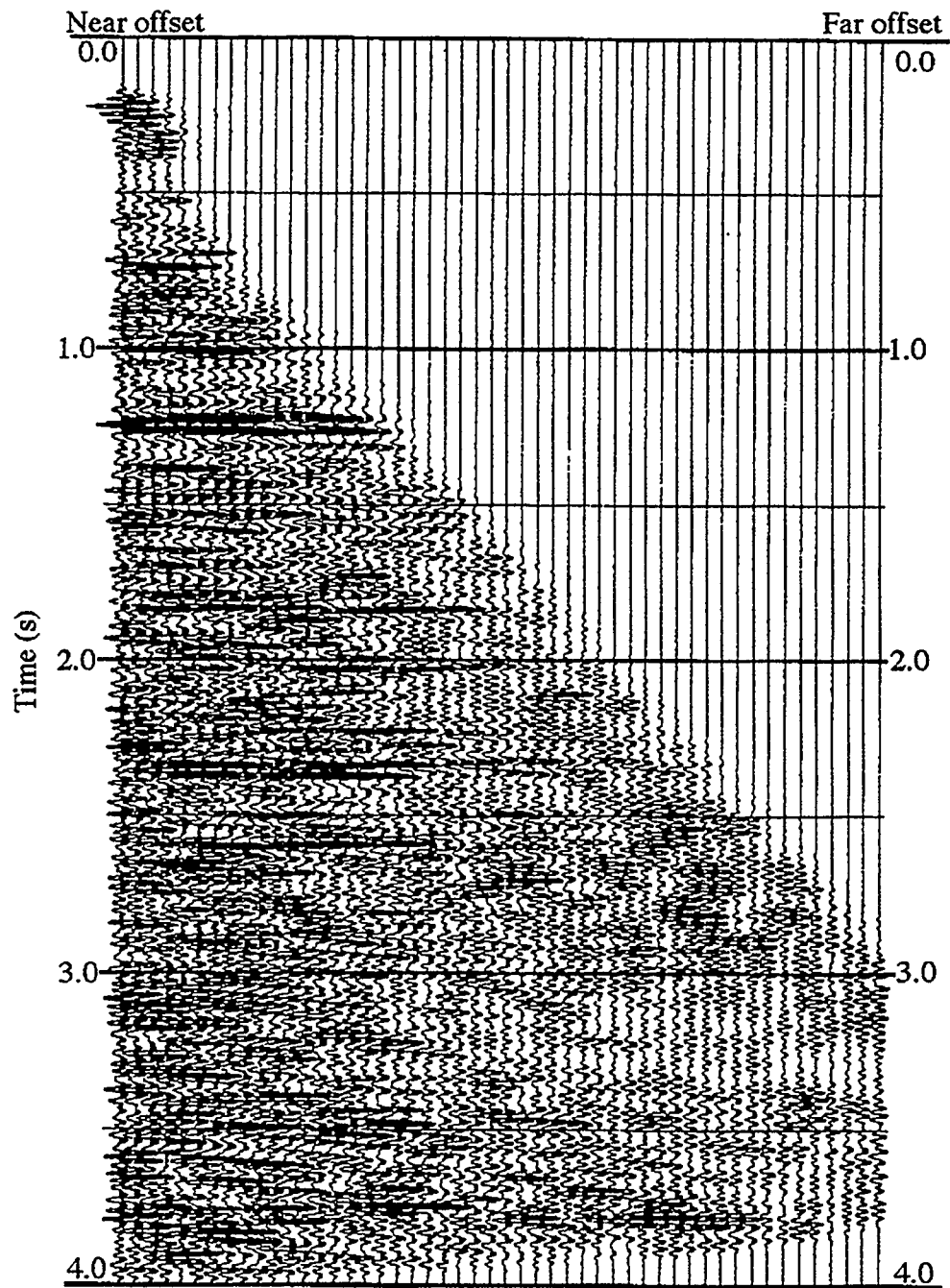


FIG. 5.14. Same CMP gather as shown in Figure 5.13, but with prestack $f-k$ filtering applied.

5.4.9 Stack and bandpass

Stacking (i.e. summing) in the CMP domain is used mainly to enhance the signal-to-noise ratio. For the dataset B, maximum fold is 51. Therefore, the signal to noise ratio was greatly increased by stacking the data.

A bandpass filter with a frequency range from 10 to 60 Hz. was applied to the stacked section which is shown in Figure 5.15.

5.4.10 Post-stack $f-k$ filtering

Linear noise persists on the stacked section (marked with *B* in Figures 5.15). This kind of linear noise was interpreted to be side-scattered energy (Yilmaz, 1987). This energy manifests itself as linear noise on the shot gather (Figure 5.11), is not apparent on the CMP gather (Figure 5.13), but reappears as linear noise on the stacked section (Yilmaz, 1987). The post-stack $f-k$ filtering was chosen to reject dipping energy in Figures 5.15. For this particular data set, post-stack $f-k$ filtering with the rejected apparent velocities range from -2,000 m/s to 2,000 m/s was chosen, since the linear noise has an apparent velocity around 1,500 m/s. Figure 5.16 shows the final stacked section with the post-stack $f-k$ filtering applied. It is noticed that the dipping events (marked with *B* in Figures 5.15) were eliminated.

5.4.11 Discussion

Through this example, it has been shown that reasonable quality of deep reflectors (around 2.4 s) can be obtained using a careful processing procedure, as shown by the final section in Figure 5.16. However, for dataset B, due to the screening effect of the first ice-bearing permafrost, most of incident P-wave energy was reflected back at the top of the first layer of ice-bearing permafrost, hence most later reflections were not particularly clear on the shot gather (Figure 5.11). Multiconverted events appear to be dominated by multiples and were not able to be processed successfully using the 'block-shift' NMO

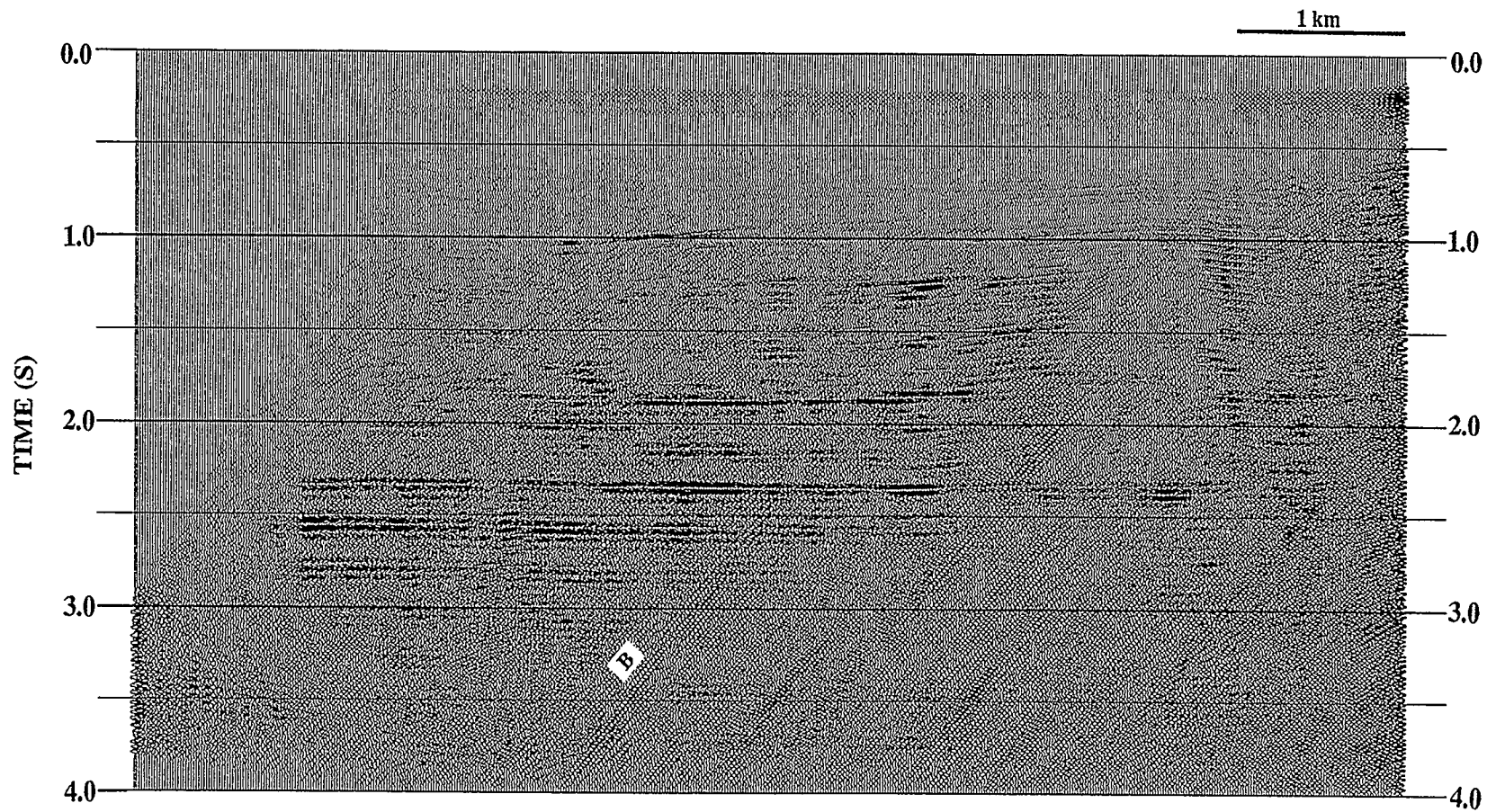


FIG. 5.16. Final stacked section for the dataset B, with a poststack $f-k$ filter applied.

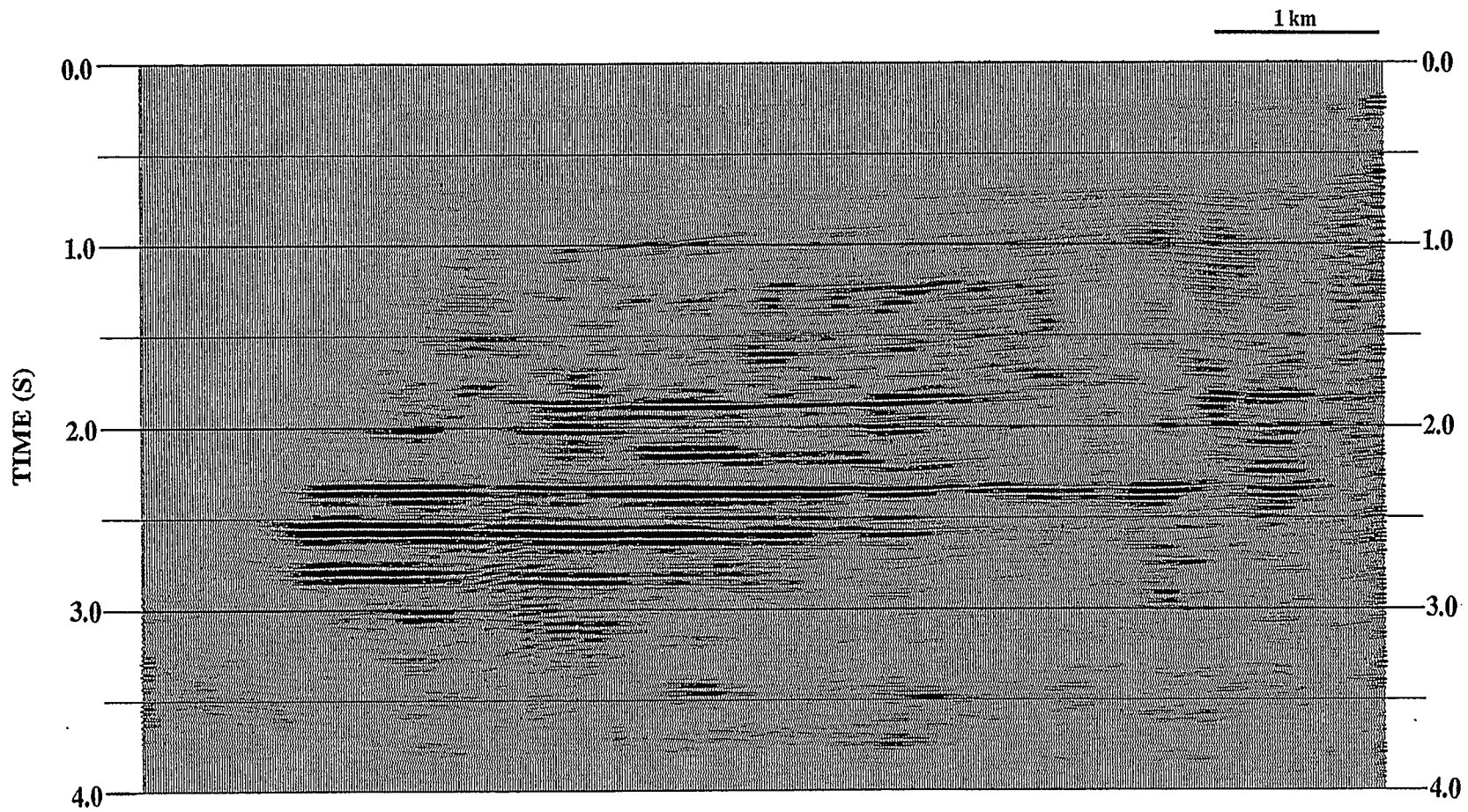


FIG. 5.16. Final stacked section for the dataset B, with a poststack $f-k$ filter applied.

procedures which were used for dataset A. The signal-to-noise ratio for the dataset B is much lower than that for the dataset A. Common offset stacks had to be generated to enhance the signal-to-noise ratio for velocity analysis.

Two passes of prestack $f-k$ filtering was applied to the dataset B. It was necessary to use the prestack $f-k$ filtering to eliminate the linear noise (marked with *A* and *B* in Figure 5.11) on the shot gather. The second pass of the prestack $f-k$ filtering was applied to eliminate the multiply energy on the CMP gather after NMO correction (Figure 5.13). Poststack $f-k$ filtering was again applied to eliminate side-scattered energy which reappears on the stacked section (Figure 5.15).

Multiples (reverberation energy within permafrost layers) of multiconverted reflections cause a noise problem for the far-offset traces in Figure 5.11. Therefore, for dataset B, we could not generate far-offset stacked sections, since far-offset traces are dominated by the multiconverted reflection multiples. Multiconverted reflections can be useful to determine the depth and the thickness of the ice-bearing permafrost (dataset A), but cause a severe multiple noise problem for the image of deeper reflectors (dataset B).

5.5 Conclusions

Based on physical and numerical modeling results shown in chapter 2 and chapter 3, two lines of field data (datasets A and B) were processed. Through this study, we conclude that analysis for the multiconverted reflections is very critical for the interpretation for the Beaufort data, especially for the shallow section. In the previous example (dataset A), multiconverted reflections (PSPSP) from the top of the second ice-bearing permafrost layer were well imaged by using a newly developed processing flow. Multiconverted reflections can be useful to determine the depth and the thickness of the ice-bearing permafrost. For the second example (dataset B), the processing was focused on the deeper reflectors. A good image for the deeper strata can be obtained when the processing flow is carefully chosen.

Chapter 6 Conclusions

6.1 Thesis summary

In the Canadian Beaufort Sea, partially due to the screening effect of the first layer of ice-bearing permafrost, the seismic image of the top of the second (and deeper) layer of ice-bearing permafrost is difficult to obtain by using conventional P-wave data. Multiconverted reflections (PSPPSP) were studied in this thesis in order to evaluate images of reflections underlying a high-velocity layer. In chapter 2, acoustic seismic physical modeling was presented for multiconverted reflections (PSPPSP) recognition and analysis. AVO analysis was undertaken for multiconverted reflections (PSPPSP) as well. Physical modeling results were complemented by computing the synthetic seismograms for equivalent physical models to verify the multiconverted reflections in terms of reflection amplitude and traveltime. Additional synthetic seismograms were generated (chapter 3) to investigate the amplitudes of multiconverted reflections for numerical models that did not have a physical equivalent. Both the physical and numerical modeling results in chapters 2 and 3 indicate that both the S-wave velocity in layer 2 and the P-wave velocity of layer 4 contribute most significantly to the multiconverted PSPPSP reflection amplitude. Numerical modeling results in chapter 3 also suggest that the P-wave velocity of layer 2 does not affect the PSPPSP event amplitude significantly, but will affect the offset range over which this event is observed. Based on the assumption of zero attenuation for all layers, the thickness and the depth of layer 2 do not contribute significantly to the amplitude of the PSPPSP reflection.

Also, from the results of model 2-2 (Figure 2.9a), a higher amplitude event for the top of layer 4 was obtained for the multiconverted reflection (PSPPSP), compared with the single-mode reflection (PPPPPP). These results could be useful, since PPPPPP events on near traces may be dominated by noise, and the multiconverted reflections

(PSPPSP) might be a more useful approach for imaging reflections below a shallow high-velocity layer.

In chapter 4, a good image for the top of layer 4 was obtained by using PSPPSP reflection when Plexiglas and Trabond were used as layer 2. This observation could be useful for seismic imaging in the Canadian Beaufort Sea, since the P-wave velocities in Plexiglas and Trabond are close to that of ice-bearing permafrost in the Canadian Beaufort Sea. Based on these investigations, two lines of field data (datasets A and B) were processed and results are presented in chapter 5. Through the field data study, we concluded that the analysis for the multiconverted reflection is very critical for the interpretation for the Beaufort data, especially for the shallow section. In the first field data example (dataset A), the multiconverted reflections (PSPPSP) from the top of the second ice-bearing permafrost layer were well imaged by using a newly developed NMO correction procedure. The imaged multiconverted reflections can be useful to determine the depth and the thickness of the ice-bearing permafrost. For the second field data example (dataset B), a good image for the deeper strata was obtained after the processing flow was carefully chosen. However, multiples of multiconverted reflections (reverberation energy within permafrost layers) cause a noise problem for the far-offset traces and multiconverted events (PSPPSP) could not be used constructively. Multiconverted reflections (PSPPSP) can be useful to determine the depth and the thickness of the ice-bearing permafrost (dataset A), but cause a severe multiple noise problem for the image of deeper reflectors (dataset B).

6.2 Future work

For dataset A in chapter 5, the multiconverted reflection PSPPSP was absent on the stacked section when a standard processing flow was used. This is because the PSPPSP reflection was muted out on the CMP gathers due to NMO stretch. In order to image the PSPPSP reflection, a different approach to the correction for normal moveout

was undertaken to avoid NMO stretch. A better image was obtained using the newly developed 'block-shift' NMO correction. The shallow far-offset multiconverted reflections (PSSP and PSPPSP) were preserved through using the 'block-shift' NMO correction method.

However, this approach is successful only in sparse reflectivity sequences and where offset-dependent tuning effects are absent. We physically spliced every stacked section for each pair of t_0 and V_{rms} . Therefore, this approach is not feasible when there is a crossing of two events, or when the time difference between two events is too small to splice. It is thus necessary to develop a better NMO correction approach for all reflections without stretching the wavelet for more common cases.

References

- Abadalla, A.A., 1989, P-SV numerical modeling and AVO of the Cardium conglomerate in the Carrot Creek field of central Alberta, Canada: The University of Calgary, CREWES Project report, v.1, 131-150.
- Aki, K. and Richards, P.G., 1980, Quantitative seismology: Theory and methods, v. 1: W.H. Freeman and Co.
- Anstey, N.A., 1986a, Whatever happened to ground roll?: Geophysics: The Leading Edge of Exploration, March, 40-45.
- Anstey, N.A., 1986b, Field techniques for high resolution: Geophysics: The Leading Edge of Exploration, April, 26-34.
- Brown, R.L., Cook, R.N. and Lynn, D., 1989, How useful is Poisson's ratio for finding oil/gas?: World Oil, October, 99-106.
- Castagna, J.P., 1993, Petrophysical imaging using AVO: Geophysics: The Leading Edge of Exploration, March, 172-178.
- Castagna, J.P. and Smith, S.W., 1993, Comparison of AVO indicators: A modeling study: 63rd Ann. Internat. Mtg., Soc. Expl. Geophy., Expanded Abstracts, 734-737.
- Cheadle, S.P., 1988, Applications of physical modeling and localized slant stacking to a seismic study of subsea permafrost: Ph.D. thesis, The University of Calgary.
- Chen, T. and Lawton, D. C., 1992a, Multiconverted reflections in marine environments: A numerical and physical seismic study: 62nd Ann. Internat. Mtg., Soc. Expl. Geophy., Expanded Abstracts, 1297-1299.
- Chen, T. and Lawton, D.C., 1992b, Multiconverted reflections in marine environments: The University of Calgary, CREWES Project report, v.4, chapter 6.
- Coulombe, C.A., 1993, Amplitude-versus-offset analysis using vertical seismic profiling and well-log data: M.Sc. thesis, The University of Calgary.

- Coulombe, C.A., Stewart, R.R., and Jones, M.J., 1992a, Elastic wave AVO using borehole seismic data: 62nd Ann. Internat. Mtg., Soc. Expl. Geophy., Expanded Abstracts, 864-866.
-
- _____, 1992b, AVO analysis of VSP and well log data: The University of Calgary, CREWES Project report, v.4, chapter 15.
- Embree, P., and Roche, S., 1983, Using vibrators in carbonate areas: presented at the 45th meeting of the European Association of Exploration Geophysicists, Oslo, Norway, June 14-17.
- Fix, J.E., Robertson, J.D., and Pritchett, W.C., 1983, Shear-wave reflections in three west Texas basins with high-velocity surface rocks: 53rd Ann. Internat. Mtg., Soc. Expl. Geophy., Expanded Abstracts, 414-416.
- Fuller, B.N., Pujol, J.M., and Smithson, S.B., 1988, Seismic reflection profiling in the Columbia Plateau: 58th Ann. Internat. Mtg., Soc. Expl. Geophy., Expanded Abstracts, 34-37.
- Gregory, A.R., 1976, Fluid saturation effects on dynamic elastic properties of sedimentary rocks: *Geophysics*, 41, 895-921.
- Gregory, A.R., 1977, Aspects of rock physics from laboratory and log data that are important to seismic interpretation: *Memoir 26 of the AAPG*, 15-46.
- Hampson, D., and Russell, B., 1990, AVO Inversion: Theory and Practice: 60th Ann. Internat. Mtg., Soc. Expl. Geophy., Expanded Abstracts, 1456-1458.
- Hampson Russell Software Service Ltd., 1991, Amplitude-versus-offset analysis: Unpublished notes.
- Jarchow, C.M., Catchings, R.D., and Lutter, W.J., 1991, How Washington crew got good, thrifty seismic in bad data area: *Oil and Gas Journal*, June 17, 54-55.
- Koefoed, O., 1955, On the effect of Poisson's Ratios of rock strata on the reflection coefficients of plane waves: *Geophy. Prosp.*, 3, 381-387.

- Landmark/ITA, 1992, ITA Insight/1 user guide.
- Le, L.H.T., Lawton, D.C., and Abramovici, F., 1992, AVO study using full-wave synthetics: 62nd Ann. Internat. Mtg., Soc. Expl. Geophy., Expanded Abstracts, 860-863.
- Meister, L.J., Roche, S.L., and Lansley, R.M., 1989, Seismic data acquisition over carbonates, volcanics and rugged topography: 59th Ann. Internat. Mtg., Soc. Expl. Geophy., Expanded Abstracts, 1373.
- Miller, S.L.M., and Stewart, R.R., 1990, Effects of lithology, porosity and shaliness on P- and S- wave velocities from sonic logs: Jour. Can. Soc. Expl. Geophys., 26, 94-103.
- Nazar, B.D., 1991, An interpretive study of multicomponent seismic data from the carrot creek area of west-central Alberta: M.Sc. thesis, The University of Calgary.
- Nazar, B.D., and Lawton, D.C., 1993, AVO analysis of a thin conglomerate deposit: Journal of Seismic Exploration, 2, 333 - 348.
- Ostrander, W. J., 1984, Plane-wave reflection coefficients for gas sands at normal angles of incidence: Geophysics, 49, 1637-1648.
- Petrel Robertson Ltd., 1991, Integrated geological and geophysical research study of porosity development, and its affects on Poisson's ratio for Swan Hills and Slave Point carbonates: Unpublished Notes.
- Poley, D.F., 1987, Acquisition and processing of high-resolution reflection seismic data from permafrost affected areas of the Beaufort Sea continental Shelf: Ph.D. thesis, The University of Calgary.
- Poley, D.F., and Lawton, D.C., 1991, A model study of multichannel reflection seismic over shallow permafrost in the Beaufort Sea continental shelf: Jour. Can. Soc. Expl. Geophys., 27, 34-42.

- Poley, D.F., Lawton, D.C., and Blasco, S.M., 1989, Amplitude-offset relationships over shallow velocity inversions: *Geophysics*, 54, 1114-1122.
- Pritchett, W.C., 1990, Problems and answers in recording reflections from beneath karst or volcanic surface: 60th Ann. Internat. Mtg., Soc. Expl. Geophy., Expanded Abstracts, 922-925.
- Pritchett, W.C., 1991, *Acquiring better seismic data*: Chapman and Hall.
- Purnell, G.W., 1992, Imaging beneath a high-velocity layer using converted waves: *Geophysics*, 57, 1444-1452.
- Purnell, G.W., McDonald, J.A., Sekharan, K.K., and Gardner, G.H.F., 1990, Imaging beneath a high-velocity layer using converted waves: 60th Ann. Internat. Mtg., Soc. Expl. Geophy., Expanded Abstracts, 752-755.
- Rupert, G.B., and Chun, J.H., 1975, The block move sum normal moveout correction: *Geophysics*, 40, 17-24.
- Rutherford, S.R., and Williams, R.H., 1989, Amplitude-versus-offset variations in gas sands: *Geophysics*, 54, 680-688.
- Sheriff, R.E., 1991, *Encyclopedic dictionary of exploration geophysics: Third Edition*: SEG.
- Smith, G.C., and Gidlow, P.M., 1987, Weighted stacking for rock property estimation and detection of gas: *Geophys. Prosp.*, 35, 993-1014.
- Stewart, R.R., 1990, Joint P and P-SV inversion: University of Calgary, CREWES Project report, v.2, 112-115.
- Tatham, R.H. and McCormack, M.D., 1991, *Multicomponent seismology in petroleum exploration*: SEG.
- Toksöz, M.N., Cheng, C.H., and Timur, A., 1976, Velocities of seismic waves in porous rocks: *Geophysics*, 41, 621-645.
- Yilmaz, O., 1987, *Seismic Data Processing*, Society of Exploration Geophysicists.

Young, R.A., and Lucas, J.E., 1988, Exploration beneath volcanics: Snake River plain, Idaho: *Geophysics*, 53, 444-452.

Zhang, C. and Stewart, R. R., 1991, Using P-Sv waves to improve conventional AVO estimates: A synthetic study: The University of Calgary, CREWES Project report, v.3, chapter 23.